Alma Mater Studiorum – Università di Bologna

DOTTORATO DI RICERCA

Ingegneria Chimica, dell'Ambiente e della Sicurezza

Ciclo XXI
Settore scientifico disciplinario di afferenza: ING/IND-24

CHARACTERIZATION AND MODELING OF THE BARRIER PROPERTIES IN NANOSTRUCURED SYSTEMS

Presentata da: Matteo Minelli

Coordinatore Dottorato
Prof. Giulio C. Sarti

Relatore
Prof. Ferruccio Doghieri

Correlatori:
Ing. Maria Grazia De Angelis
Ing. Marco Giacinti Baschetti

Esame finale anno 2009

Summary

CHAPTER I

Introduction

Nanostructured materials may be defined as those materials whose structural elements, clusters, crystallites or molecules, have at least one dimension in the order of the nanometers, i.e. from 1 to 100 nm, more typically less than 50 nm. Nanostructured materials include atomic clusters, layered or lamellar films, filamentary structures, and bulk nanostructured materials.

Nanostructure science and technology has become now an identifiable, very broad and multidisciplinary, field of research and emerging application. It is one of the most visible and growing research areas in materials science in its broadest sense.

It is almost traditional to quote from Feynman's visionary lecture "There is plenty of room at the bottom" in 1959 [1], the early beginning of such new class of materials, but its largest development belongs to the last two decades.

The explosion in both academic and industrial interest in these materials begins from the remarkable improvements in fundamental electrical, optical as well as barrier properties that occur going from an "infinitely extended" solid to a particle of material consisting of a countable number of atoms. In some cases, the physics of nano-sized materials can be very different from the macroscale behavior of the same substance, offering often superior properties that warrant much interest in these materials [2-3].

In this concern, nanotechnologies arise many approaches in developing new classes of materials for specific applications and suitable in several fields.

1.1 Nanocomposites: polymer-layered silicates

In recent years, a significant interest in the nanotechnology has been devoted to the study of polymer-layered silicate nanocomposites, because they often exhibit remarkable improvement in materials properties, with just few percent of inorganic phase, to be compared with the case of classic composites, where a significant amount of filler content is needed to obtain interesting results in properties enhancement. These improvements can include high modulus [4-5], increased strength and heat resistance [6], decreased gas permeability [7-8] and flammability [9], and increased biodegradability of biodegradable polymers [10]. Such improvements make these materials very attractive for applications in many different fields, from automotive, to painting and packaging.

The commonly used layered silicates for the preparation of this type of nanocomposites belong to the same general family of 2:1 layered or phyllosilicates. Their crystal structure consists of layers made up of two tetrahedrally coordinated silicon atoms fused to an edge-shared octahedral sheet of either aluminum or magnesium hydroxide. The layer thickness is around 1 nm, while lateral dimensions may vary from 30 nm to several microns or larger, depending on the particular layered silicate. Montmorillonite (MMT), Hectorite, and Saponite are the most commonly used layered silicates. Two peculiar characteristics of these silicates are extremely important for their use as nanofiller: the ability of the silicate particles to disperse into individual layers, and the possibility of finely tune their surface chemistry through ion exchange reactions with organic and inorganic cations.

The physical mixture of a polymer and layered silicate may not form a nanocomposite, so, in order to improve the compatibility of the two phases, the polymer-silica interaction is usually artificially enhanced: the interlayer surfaces of the silicate are chemically treated to make the silicate less hydrophilic and therefore more wettable by the polymer.

In general, due to the very high aspect ratio of layered silicates (varying in the range 10-1000), a few weight percent of inorganic phase, properly dispersed

throughout the polymer matrix, creates much higher surface area for polymer/filler interaction as compared to conventional composites [10]. Depending on the strength of interfacial interactions between the polymer matrix and layered silicate (modified or not), there are three different types of layered nanocomposites, as shown in Figure 1-1, and the physical properties of the resultant system are significantly different [11]:

- Phase-separated: the polymer is unable to penetrate between the silicate sheets, and the properties stay in the same range as those for traditional micro-composites.
- Intercalated: a single extended polymer chain can penetrate between the silicate layers, and a well-ordered multilayer morphology results with alternating polymeric and inorganic layers. Properties of the composites typically resemble those of ceramic materials.
- Exfoliated: the silicate layers are completely and uniformly dispersed in a continuous polymer matrix, an exfoliated or delaminated structure is obtained [12].

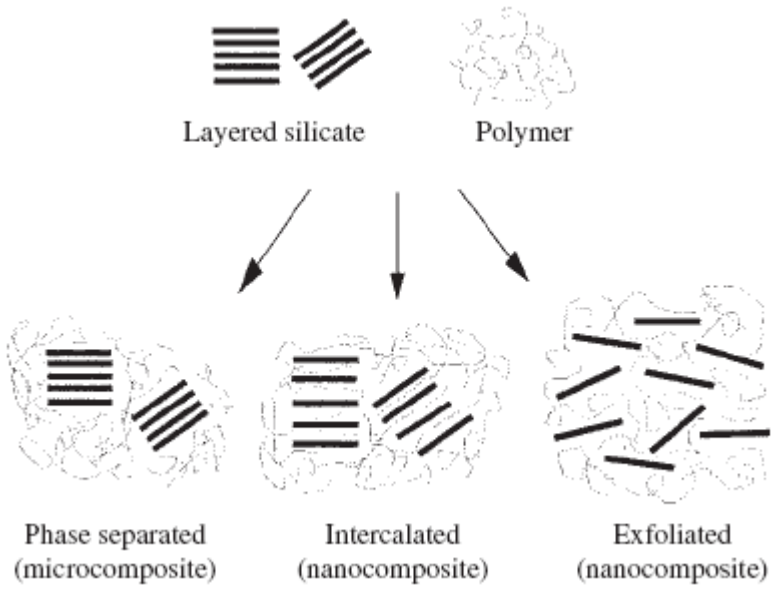

Figure 1-1, Morphologies of a polymer layered-silicate nanocomposite [12].

The exfoliation of the inorganic material throughout the polymer is a crucial point to make a successful nanocomposite; if a uniform dispersion is not achieved,

agglomerates of inorganic material are found within the host polymer matrix, limiting the improvement.

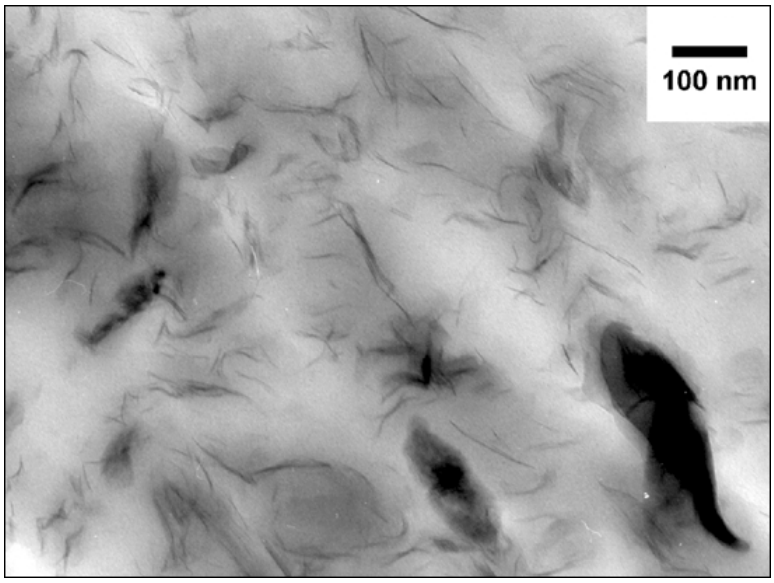

Figure 1-2, TEM photomicrograph of MMT-nylon 6 composites [13].

Layered nanocomposites provide reinforcing efficiency because of their high aspect ratios; furthermore, their properties are strongly influenced by the size scale of the component phases and the degree of mixing between the two phases. Depending on the nature of the components used and the method of preparation, significant differences in composite properties may be obtained [14].

1.2 Nanocomposites: organic-inorganic hybrid coatings via sol-gel technique

A second class of composite materials, with nano-sized inorganic and organic domains deeply interconnected, has been developed with a bottom-up approach, by exploiting the sol-gel chemistry [15-16]. The sol-gel process is mainly based on inorganic polymerization reactions and it is a chemical synthesis method commonly used for the preparation of inorganic materials such as glasses and ceramics. The most relevant feature of this technique is the low processing temperature that also provides unique opportunities to make pure and well-

controlled composition organic-inorganic hybrid materials incorporating low molecular weight species and organic molecules with appropriate inorganic moieties, preserving thus the stability and the characteristics of such organic phases.

These hybrid materials have, in perspective, interesting applications in the field of packaging [17-18], in view also of the possibility of including a high content of inorganic phase, of an easy control of their properties by a suitable choice of reactants and catalyst and of the easy application of such materials as thin coatings onto plastics substrates [19].

The aim of this approach is to combine the properties of different materials leading to the development of composite materials or blends, in which two different phases with complementary physical properties are mixed. So, while using a polymer as organic phase gives tenacity and flexibility as well as a good adhesion to different substrates (that is extremely important in the case of coatings application), the inorganic component brings in the hybrid its toughness and a remarkable thermal and chemical stability as well as good barrier properties. Furthermore, the concept of composites originated in the idea of producing materials having better properties than either of the two components is achievable by combining the chemical groupings with different properties at the nanoscopic level. Although such materials are macroscopically homogeneous, their properties reflect the nature of the chemical building blocks from which they are composed. The blending of organic and inorganic components and the synergism of their properties is particularly useful and allows the development of materials with totally new properties [20]. Some recent papers and patents have, for instance, claimed a strong decrease of the oxygen permeation rate of plastic films by using hybrid coatings [21-22].

The aforementioned sol-gel reaction is a method to prepare pure ceramic precursors and inorganic glasses at relatively low temperatures. The reaction is generally divided into two steps: hydrolysis of metal alkoxides to produce hydroxyl groups, followed by polycondensation of the hydroxyl groups and residual alkoxyl groups to form a three-dimensional network, as shown in Figure 1-3.

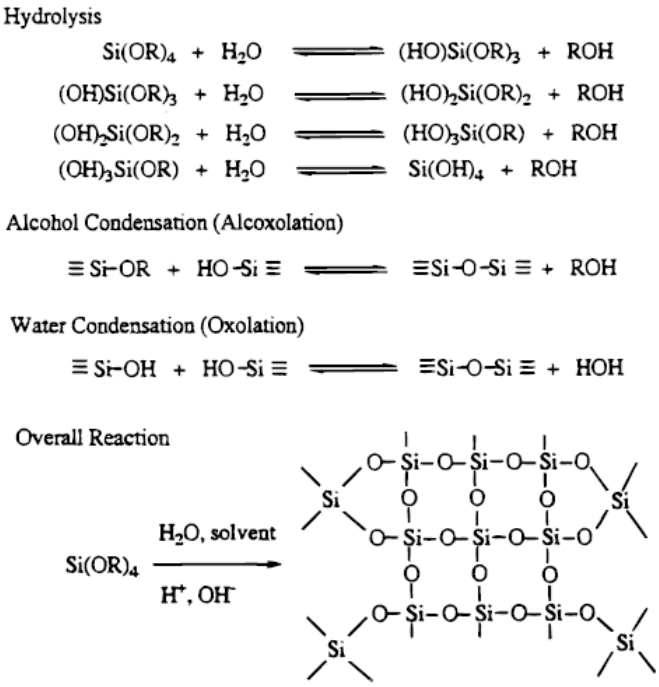

Figure 1-3, Reaction scheme of the sol-gel route [15].

The sol-gel route generally starts with alcoholic, or other low molecular weight organic solutions of monomeric, metal or semimetal alkoxide precursors $M(OR)_n$, where M represents a network-forming element such as Si, Ti, Zr, Al, B, etc., and R is typically an alkyl group (C_xH_{2x+1}), and water. Generally, the hydrolysis and condensation reactions occur simultaneously once the hydrolysis reaction has been initiated. Both the hydrolysis and condensation steps generate low molecular weight byproducts such as alcohol and water. These small molecules must be removed from the system, and such removal would lead, in the limit, to a tetrahedral SiO_2 network if the species were silicon. The removal of these byproducts also contributes to the high shrinkage that occurs during the classical sol-gel process.

In the case of silicon based metal alkoxides, the hydrolysis and condensation reactions typically proceed with either an acid or base as catalyst, and the structure and morphology of the resulting network strongly depend on the nature of the catalyst, in particular, the pH of the reaction [15].

In this concern, a new range of material properties can be produced, incorporating many different polymeric or oligomeric species within inorganic networks by

different synthetic approaches. The chemical bond between inorganic and organic phases can be introduced mainly by three approaches:

- Functionalizing oligomeric/polymeric species with silane, silanol, or other functional groups that can undergo hydrolysis and condensation with metal alkoxides.
- Utilizing already existing functional groups within the polymeric/oligomeric species.
- Using alkoxysilanes ($R\text{-}Si(OR)_3$) as the unique or one of the precursors of the sol-gel process with R- being a second-stage polymerizable organic group often carried out by either a photochemical or thermal curing following the sol-gel reaction [15].

Figure 1-4 is a FE-SEM micrograph of a PVOH-SiO_2 hybrid gel reported as an example of the microstruture and of the morphology of these organic-inorganic systems, and it shows that silica domains, with fairly small size, are uniformly dispersed in the polymeric matrix, suggesting the strong interaction between the two phases that characterizes this network [23].

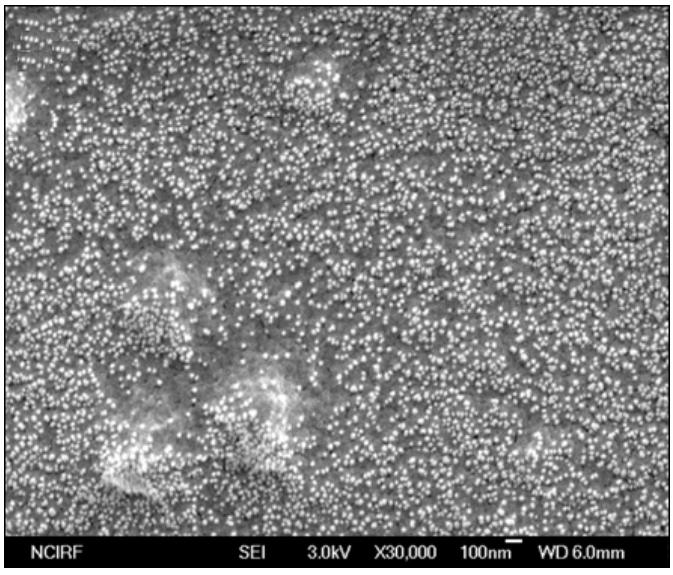

Figure 1-4, FE-SEM micrograph of a PVA/SiO_2 hybrid gel with TEOS contents 0.04 mol [23].

1.3 Microfibrillated cellulose

Although microfibrillated cellulose (MFC), a biodegradable system produced by delamination of cellulosic fibers in high-pressure homogenizers, has been know since the beginning of the 80s, it is in the recent years that it is emerging in the world of nano-phased materials for its surprising properties, promising for a wide variety of applications.

A fully delaminated MFC consists of rather long microfibrils, in the micrometer range (usually between 700 nm and 1 μm), with a diameter of some tenths of nanometers (10-20 nm). Microfibrillated cellulose consists of nanostructures with high stiffness and strength, crystals with self-organizing effects, and hydroxyl groups at the surface, providing reaction sites for further modifications [24]. It is soluble in water where it tends to form a highly viscous, shear-thinning transparent gel.

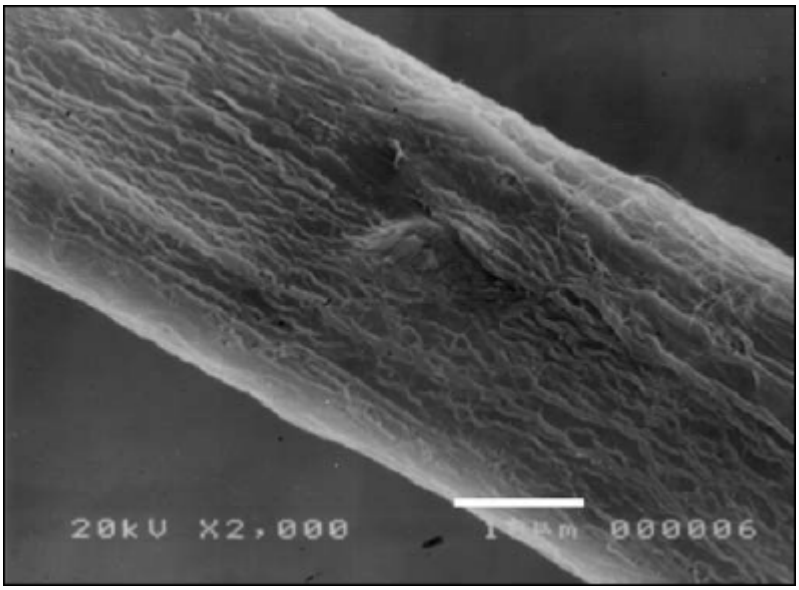

Figure 1-5, SEM micrograph of a kraft pulp single elementary fiber (Scale bar: 10 μm) [25].

There are several potential applications for such new class of cellulose regarding the field of paper and paperboard materials: taking advantage of its features, MFC can be indeed applied to improve the mechanical properties, as surface strength agent to prevent linting, or to form nano-coatings or nano-barriers. The MFC is a highly attractive organic and biodegradable reinforcement for polymer

nanocomposite, due to its high aspect ratio, good mechanical properties and its ability to form networks. Films of pure microfibrillated cellulose can also bear large stresses and strains before failure and, as consequence, MFC can be used in biodegradable composites with for instance starch. In the recent years, indeed, several composite systems have been prepared and studied, either from the mechanical or from the barrier properties point of view, showing remarkable improvement due to the addition of MFC [26-28].

Figure 1-6 shows two SEM micrographs of a starch matrix (50/50 amylopectin/glycerol matrix) reinforced by cellulose nanofibrills and of a pure MFC film.

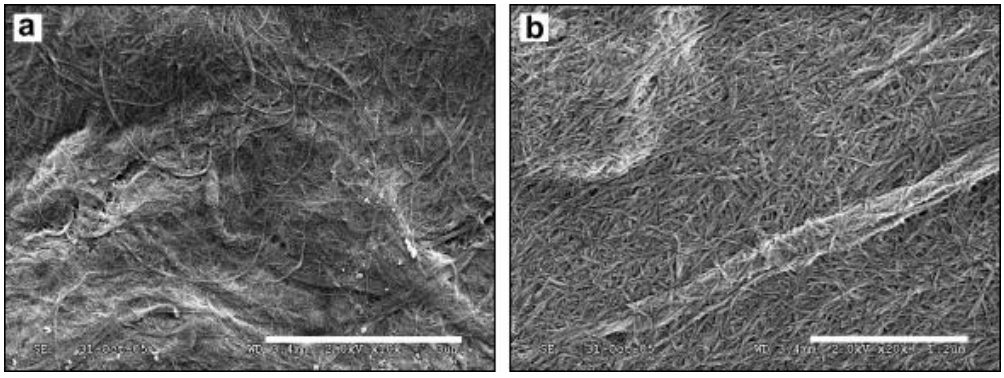

Figure 1-6, FE-SEM micrographs of the surface of (a) cellulose nanofiber reinforced composite and (b) a neat cellulose film. (Scale bars: (a) 3 μm and (b) 1.2 μm) [29].

As one can see in the pictures, some porosity is present in both cases, while the random orientation and distribution of the fibers is to be considered as apparent. The thickness of most nanofibers is about 30 nm, although thicker entities are present and the typical nanofiber length is several microns, resulting in a high aspect ratio [29].

A crucial point, to predict and control the properties of cellulosic systems is to understand the water-cellulose interaction due to the strong influence of the water content onto the structural and mechanical properties of such hydrophilic material. In this concern, the particular structure of the microfibrillated nanofibers is able to reduce the water uptake, while the kinetic of the moisture sorption is surprisingly rather long, as reported by different authors [30-32]; this makes these materials interesting for a broad variety of applications.

1.4 Self-assembling monolayers

Organic molecules can spontaneously assemble on various surfaces to form a highly-ordered, crystalline-like monolayer, in which the hydrocarbon chains are oriented almost perpendicular to the surface, as shown in Figure 1-7.

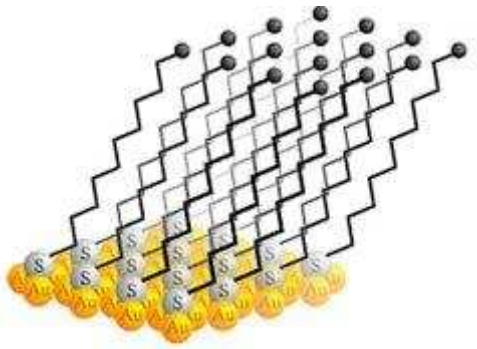

Figure 1-7, *n*-alkanthiolate self assembled monolayer on gold [33].

The formation of monolayers by the organization of surfactant molecules at surfaces is one example of the general phenomenon of self-assembly. The ability to tailor both head and tail groups of the constituent molecules makes self-assembling monolayers excellent systems for a more fundamental understanding of the mechanism which is affected by competing intermolecular, molecular-substrates and molecule-solvent interactions.

SAMs are ordered molecular assemblies formed by the adsorption of an active surfactant on a solid surface. This simple process makes SAMs inherently manufacturable and thus technologically attractive for building superlattices and for surface engineering. The order in these two-dimensional systems is produced by a spontaneous chemical synthesis at the interface as the system approaches equilibrium. Although the area is not limited to long chain molecules, SAMs of functionalized long-chain hydrocarbons are most frequently used as building blocks of super-molecular structures [34]. One deeper reason why organic materials are attractive in such diverse fields is probably due to the tunability of the properties of these materials by selectively modifying specific functional groups while leaving the rest of the molecule unchanged [34].

The general concept of self-assembly, which exploits the preferential, strong binding of one functional group of the molecule to the substrate is the preparation both from solution and from the gas phase, except for those systems, where a precursor reaction is required in the solution.

The ease of preparation and the low costs of solution deposition are one important reason for the popularity of SAMs. They can be prepared using different types of molecules and different substrates, widespread examples are alkylsiloxane monolayers, fatty acids on oxidic materials and alkanethiolate monolayers.

The principle to prepare a SAM is rather simple, once that the substrate has been properly cleaned, it has just to be dipped into the corresponding solution for a certain period of time, and the monolayer will assemble. Considering the alkanethiolate on gold, the route of synthesis is shown in two steps in Figure 1-8: the substrate, a golden sheet, is immersed into an ethanol solution of the desired thiol. After an initial fast adsorption (order of magnitude of seconds), an organization phase follows, which should be allowed to continue for a longer time (about one day) in order to achieve the best results.

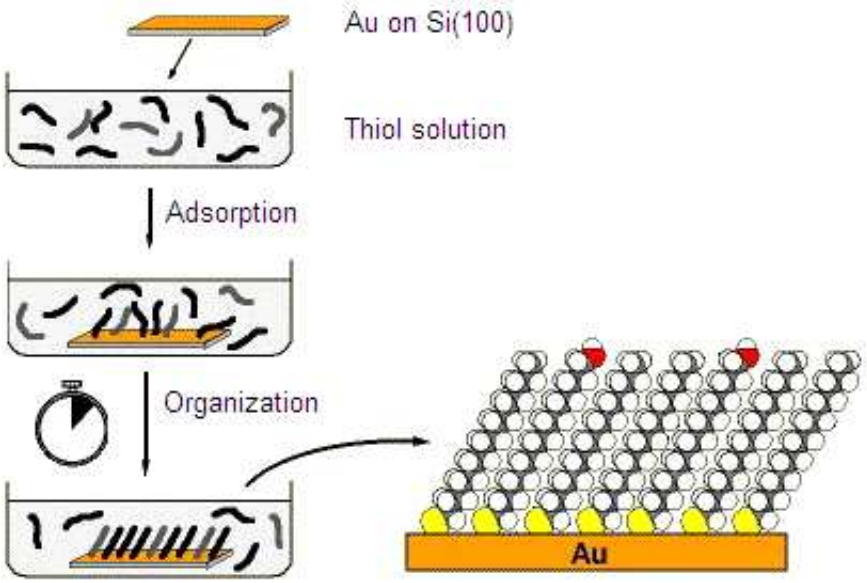

Figure 1-8, Scheme for the preparation of *n*-alkanethiolates SAMs on gold [35].

These materials often exhibit optical, electrical, optoelectronical, mechanical, chemical, or other properties interesting for the potential applications, which are not accessible with inorganic materials. Besides the classical areas of technology,

organic thin films can also play an important role in interfacing bio-technological devices [36-37]. An important application of these material belongs to the field of the barrier properties; it has been proved, indeed, that the thin (1-3 nm) hydrocarbon layer of the SAM can provide significant protection against oxidation to a metal surface. This demonstration is based on the observation that the rate of oxidation becomes slower as the *n*-alkanethiols used to make the SAM become longer, guaranteeing therefore a thicker barrier layer [38].

1.5 Barrier properties of nanostructured materials

The above mentioned qualities of nano-sized material are often exploited in the field of membrane applications, such as gas separation, as well as in the packaging industry; in both cases, the permeation of chemical species through the polymeric-based membrane plays a key role. In gas separation membranes, nanotechnology is often employed to develop new classes of materials with improved perm-selectivity preserving the productivity levels already achieved by pure polymer membranes. In this concern, the combination of nano-sized ceramic materials with the polymer matrix has received much attention in recent years [39-42].

On the other hand, barrier films find applications in a wide range of different areas in preventing the permeation of species which would damage the packaged product; a fist example is in paints where keeping water out is usually the primary objective and the addition of aligned mica flakes can inhibit metal corrosion [43]. Although the barrier performance of materials have perhaps never attracted so much industrial attention as over recent decades, when it started to be associated with some modern food and beverage packaging technologies making use of plastic materials [44-46], it became an important issue associated with food commercialization, food shelf life extension, quality and safety [47]. The widest application for barrier membranes is, indeed, in extending the shelf-life of the food product, i.e. the time during which food maintains its hygienic and sensorial characteristics. Shelf-life can be significantly improved by enhancing the barrier

properties of the food package towards oxygen that enables microbial metabolism and food degradation. The decrease of the oxygen transfer rate would therefore allow to widen the application of plastic films to the packaging of a lot of different food products, whose shelf-life is today achieved by a low temperature storage coupled with particular packaging conditions, such as Modified Packaging Atmosphere (MPA) [48].

References:

[1] Feynman R.P. There's plenty of room at the bottom (originally published in the February 1960 ed. Caltech Engineering and Science Journal) http://www.zyvex.com/nanotech/feynman.html (1959).

[2] Moriarty P. Nanostructured materials. *Rep. Prog. Phys.* **64** (2001) 297-381.

[3] Koch C. Nanostructured materials: processing, properties and applications. Taylor & Francis (2002).

[4] LeBaron P.C., Wang Z., Pinnavaia T.J. Polymer-layered silicate nanocomposites: an overview. *Appl. Clay. Sci.* **15** (1999) 11-29.

[5] Giannelis E.P. Polymer layered silicate nanocomposites. *Adv. Mater.* **8** (1996) 29-35.

[6] Giannelis E.P. Polymer-layered silicate nanocomposites: synthesis, properties and applications. *Appl. Organomet. Chem.* **12** (1998) 675-680.

[7] Messersmith P.B, Giannelis E.P. Synthesis and barrier properties of poly(1-caprolactone)-layered silicate nanocomposites. *J. Polym. Sci, Part A: Polym. Chem.* **33** (1995)1047-57.

[8] Yano K., Usuki A., Okada A., Kurauchi T., Kamigaito O. Synthesis and properties of polyimide-clay hybrid. *J. Polym. Sci., Part A: Polym. Chem.* **31** (1993) 2493-2498.

[9] Gilman J.W. Flammability and thermal stability studies of polymer-layered silicate (clay) nanocomposites. *Appl. Clay. Sci.* **15** (1999) 31-49.

[10] Sinha Ray S., Yamada K., Okamoto M., Ueda K. New polylactide/layered silicate nanocomposite: a novel biodegradable material. *Nano Lett.* **2** (2002) 1093-1096.

[11] Hussain F., Hojjati M., Okamoto M., Gorga R.E. Polymer-matrix nanocomposites, processing, manufacturing and application: an overview. *J. Comp. Mater.* **40** (2006) 1511-1575.

[12] Alexandre M., Dubois P. Polymer-layered silicate nanocomposites: preparation, properties and uses of a new class of materials. *Mater. Sci. Eng. Rep.* **28** (2000) 1-63.

[13] Fornes T.D., Yoona P.J., Hunter D.L., Keskkula H., Paul D.R. Effect of organoclay structure on nylon 6 nanocomposite morphology and properties. *Polymer* **43** (2002) 5915-5933.

[14] Park C., Park O., Lim J., Kim H. The fabrication of syndiotactic polystyrene/organophilic clay nanocomposites and their properties. *Polymer* **42** (2001) 7465-7475.

[15] Wen J., Wilkes G.L. Organic/inorganic hybrid network materials by the sol-gel approach. *Chem. Mater.* **8** (1996) 1667-81.

[16] Sanchez C., Julian B., Belleville P., Popall M. Applications of hybrid organic-inorganic nanocomposites. *J. Mater. Chem.* **15** (2005) 3559-3592.

[17] Amberg-Schwab S., Katschorek H., Weber U., Burger A., Haensel R., Steinbrecher B. Inorganic-organic polymers as migration barriers against liquid and volatile compounds. *J. Sol-Gel Sci. Technol.* **26** (2003) 699-703.

[18] Lee S.Y., Lee J.D., Yang S.M. Preparation of silica-based hybrid materials coated on polypropylene film. *J. Mater. Sci.* **34** (1999) 1233-1241.

[19] Mackenzie1 J.D., Bescher E.P. Physical properties of sol-gel coatings. *J. Sol-Gel Sci. Technol.* **19** (2000) 23-29.

[20] Schubert U., Husing N., Lorenz A. Processing of organofunctional metal alkoxides. *Chem. Mater.* **7** (1995) 2010-2027

[21] Amberg-Schwab S., Weber U., Burger A., Nique S., Xalter R. Development of passive and active barrier coatings on the basis of inorganic-organic polymers. *Monatsh. Chem.* **137** (2006) 657-666.

[22] Amberg-Schwab S., Burger A., Weber U., Xalter R., Nique S. Lacquer compositions with oxygen scavenger and/or oxygen indicator function for coatings or adhesives layers in food packaging films. *PCT Int. Appl.* (2007) (WO 2007051860).

[23] Kim S.W. Preparation and barrier property of poly(vinyl alcohol)/SiO_2 hybrid coating films. *Korean J. Chem. Eng.* **25** (2008) 1195-1200.

[24] Ankerfors M. The manufacture of microfibrillated cellulose (MFC) its application. Nanostrucured cellulose and new cellulose derivatives seminar (2006).

[25] Nakagaito A.N., Yano H. The effect of fiber content on the mechanical and thermal expansion properties of biocomposites based on microfibrillated cellulose. *Cellulose* **15** (2008) 555-559.

[26] Shields R.J., Bhattacharyya D., Fakirov S. Oxygen permeability analysis of microfibril reinforced composites from PE/PET blends. *Compos. Part A: Appl. S.* **39** (2008) 940-949.

[27] Dufresne A., Vignon M.R. Improvement of starch film performances using cellulose microfibrils. *Macromolecules* **31** (1998) 2693-2696.

[28] Lu J., Wang T., Drzal L.T. Preparation and properties of microfibrillated cellulose polyvinyl alcohol composite materials *Compos. Part A: Appl. S.* **39** (2008) 738-746.

[29] Svagan A.J., Hedenqvist M.S., Berglund L. Reduced water vapour sorption in cellulose nanocomposites with starch matrix. *Compos. Sci. Technol.* **69** (2009) 500-506.

[30] Topgaard D., Soderman O. Diffusion of water absorbed in cellulose fibers studied with ^{1}H-NMR. *Langmuir* **17** (2001) 2694-2702.

[31] Dufresne A., Dupeyre D., Vignon M.R. Cellulose microfibrils from potato tuber cells: processing and characterization of starch-cellulose microfibril composites. *J. App. Pol. Sci.* 76 (2000) 2080-2092.

[32] López-Rubio A., Lagaron J.M., Ankerfors M., Lindström T., Nordqvist D., Mattozzi A., Hedenqvist M.S. Enhanced film forming and film properties of amylopectin using micro-fibrillated cellulose. *Carb. Polym.* **68** (2007) 718-727.

[33] http://www.ehcc.kyoto-u.ac.jp

[34] Ulman A. Formation and structure of self-assembled monolayers. *Chem. Rev.* **96** (1996) 1533-1554.

[35] Schreiber F. Structure and growth of self-assembling monolayers. *Prog. Surf. Sci.* **65** (2000) 151-256.

[36] http://www.ifm.liu.se

[37] Love J.C., Estroff L.A., Kriebel J.K., Nuzzo R.G., Whitesides G.M. Self-assembled monolayers of thiolates on metals as a form of nanotechnology. *Chem. Rev.* **105** (2005) 1103-1169.

[38] Laibinis P.E., Whitesides G.M. Self-Assembled monolayers of *n*-alkanethiolates on copper are barrier films that protect the metal against oxidation by air. *J. Am. Chem. Soc.* **114** (1992) 9022-9028.

[39] Suer M.G., Baç N., Yilmaz L.Gas permeation characteristics of polymer-zeolite mixed matrix membranes. *J. Membr. Sci.* **91** (1994) 77-86.

[40] Vu D.Q., Koros W.J., Miller S.J. Mixed matrix membranes using carbon molecular sieves II. Modeling permeation behavior. *J. Membr. Sci.* **211** (2003) 335-348.

[41] Cong H., Radosz M., Towler B.F., Shen Y. Polymer-inorganic nanocomposite membranes for gas separation. *Sep. Purif. Tech.* **55** (2007) 281-291.

[42] Koh H.C., Park J.S., Jeong M.A., Hwang H.Y., Hong Y.T., Ha S.Y., Nam S.Y. Preparation and gas permeation properties of biodegradable polymer/layered silicate nanocomposite membranes. *Desalination* **233** (2008) 201-209.

[43] Moggridge G.D., Lape N.K., Yang C., Cussler E.L. Barrier films using flakes and reactive additives. *Prog. Org. Coat.* **46** (2003) 231-240.

[44] Bureau G., Multon J.L. Food packaging technology. VCH Publishers. New York (1995).

[45] Brody A.L., Marsh K.S. The Wiley encyclopedia of packaging technology, 2nd edn. Wiley. New York (1997).

[46] Hanlon J.F., Kelsey R.J.,Forcinio H.E. Handbook of package engineering, 3rd edn. Lancaster. Technomic Publishing Co. (1998).

[47] Lagaron J.M., Català R., Gavara R. Structural characteristics defining high barrier properties in polymeric materials. *Mat. Sci. Tech.* **20** (2004) 1-7.

[48] Minelli M., De Angelis M.G., Doghieri F., Marini M., Toselli M., Pilati F. Oxygen permeability of novel organic-inorganic coatings: I. Effects of organic-inorganic ratio and molecular weight of the organic component *Eur. Polym. J.* **44** (2008) 2581-2588.

CHAPTER II

Experimental

The mass transport through polymeric membranes can be approached by the sorption-diffusion model, in which the process is described by two different steps: at first the dissolution of the probe molecules in the polymeric matrix and then its diffusion through the membrane, driven by a chemical potential gradient of the gas.

The gas diffusion in polymer generally is correctly described by the Fick's law with a diffusion coefficient that can be considered constant in a reasonable wide concentration range; it is thus assumed as not changing during the test. Under these conditions, Fick's law gives the distribution of the gas concentration c (x,t) in the solid phase as a simple material balance for the solute within the membrane:

$$\frac{\partial c}{\partial t} = D \cdot \nabla^2 c \qquad (1)$$

Appropriate boundary and initial conditions have also to be applied to describe the experimental conditions. In the present case, polymeric membranes are thin films in which the thickness of the geometry is considerably smaller then the other dimensions and it should be considered that the diffusion occurs in only one dimension, through the thickness direction. In this hypothesis the equation becomes:

$$\frac{\partial c}{\partial t} = D\frac{\partial^2 c}{\partial x^2} \qquad (2)$$

2.1 Permeation

In permeation experiments in polymeric membranes, the mass transport is a pure diffusive phenomenon and, since the solution polymer-gas is extremely diluted, the

mass balance is given by Eq. (2). Hence, the problem has been uniquely described by imposing the proper boundary and initial conditions. The two membrane surfaces can be considered as at constant concentration in the entire test: the pressure, indeed, is proportional to the concentration according to Henry's law ($c = S\,p$), and it does not change significantly due to very low fluxes. Then, as initial condition, the concentration in the membrane has been considered as uniform, and in most of the case, it is equal to 0 (dry membrane). The complete set is formalized as follows:

$$\begin{aligned} c(0,t) &= c_1 \\ c(l,t) &= c_2 \\ c(x,t) &= c_0 \end{aligned} \tag{3}$$

where l is the thickness of the membrane.

In the first part of the test, a transient state is observed due to the gas sorption of the solid phase, and then a steady state is reached when the membrane has been saturated and the solute concentration remains constant during the time. Therefore, under these conditions and if D is kept constant and the Fick's law becomes:

$$\frac{\partial c}{\partial t} = D\frac{\partial^2 c}{\partial x^2} = 0 \Rightarrow \frac{d^2 c}{dx^2} = 0 \tag{4}$$

The integration of Eq. (4) gives easily the concentration profile in the membrane as linear along the x direction:

$$\frac{c - c_1}{c_2 - c_1} = \frac{x}{l} \tag{5}$$

Furthermore, the steady conditions guarantee a constant flux J_{SS} through the membrane and it can be expressed as:

$$J_{SS} = -D\frac{\partial c}{\partial x} = D\frac{(c_1 - c_2)}{l} \tag{6}$$

However, in permeation experiments, the differential pressure among the sample is known rather then c_1, and c_2, and the concept of permeability P has been introduced:

$$J = P\frac{(p_1 - p_2)}{l} \tag{7}$$

At this point, by means of the Henry's law, it is possible to derive the relationship between permeability and diffusivity, being S the gas solubility in the polymer film:

$$P = D \cdot S \tag{8}$$

In case of a manometric apparatus, the amount of mass permeated is calculated by monitoring the pressure of the downstream volume (that has known value), and the flux at the steady state can is linear with the pressure derivative and, in the assumption of ideal gas, it is given by:

$$\left|J\right|_{ss} = \left(\frac{dp_1}{dt}\right)_{t\to\infty} \cdot \frac{V}{RT} \cdot \frac{1}{A} \tag{9}$$

where V is the downstream volume, A the membrane area and T the temperature.

The Transfer Rate (*T.R.*), or permeance, is a specific flux density; hence J_{ss} is divided by the driving force of the phenomenon, i.e. the pressure difference:

$$T.R. = \frac{-\left|J\right|_{ST}}{p_1 - p_2} = -\left(\frac{dp_1}{dt}\right)_{t\to\infty} \cdot \frac{V}{RT} \cdot \frac{1}{A} \cdot \frac{1}{\left(p_1 - p_2\right)} \tag{10}$$

However, the permeance is still an operative property, because it is related to the sample geometry, namely the thickness of the film, while the permeability depends only on the nature of the membrane and it is given by:

$$P = T.R. \cdot l = \frac{-\left|J\right|_{ST} \cdot l}{p_1 - p_2} = -\left(\frac{dp_1}{dt}\right)_{t\to\infty} \cdot \frac{V}{RT} \cdot \frac{l}{A} \cdot \frac{1}{\left(p_1 - p_2\right)} \tag{11}$$

The permeability has been expressed in Barrer:

$$1 \text{ Barrer} = 10^{-10} \cdot \left(\frac{cm^3(STP) \cdot cm}{cm^2 \cdot s \cdot cmHg}\right) \tag{12}$$

To describe the complete process and to capture the concentration behavior over time in the transient state, the differential equation Eq. (2) has to be solved considering the I.C. and B.C. in Eqs. (3), and the complete solution is given by Crank [1]:

$$\begin{aligned} c = c_1 + (c_2 - c_1)\frac{x}{l} + \frac{2}{\pi}\sum_{n=1}^{\infty}\frac{c_2\cos n\pi - c_1}{n}\sin\frac{n\pi x}{l}e^{-Dn^2\pi^2 t/l^2} + \\ + \frac{2}{l}\sum_{n=1}^{\infty}\sin\frac{n\pi x}{l}e^{-Dn^2\pi^2 t/l^2}\int_0^l f(x')\sin\frac{n\pi x'}{l}dx' \end{aligned} \tag{13}$$

The instantaneous flux that exits from the membrane is the permeate rate at $x = 0$, i.e. the low concentration surface, and it is given by:

$$\left|J\right|_{x=0} = D\left(\frac{\partial c}{\partial x}\right)_{x=0} \tag{14}$$

Substituting the concentration profile of Eq. (13) and integrating over time the flux at the interface, the amount of permeate Q_t at time t is determined.

In the hypothesis of negligible pressure in the downstream volume and dry membrane at $t = 0$, Q_t can be written as:

$$\frac{Q_t}{l \cdot C_1} = \frac{D \cdot t}{l^2} - \frac{1}{6} - \frac{2}{\pi^2} \cdot \sum_1^{\infty} \left(\frac{(-1)^n}{n^2} \cdot e^{-\frac{D \cdot n^2 \cdot \pi^2 \cdot t}{l^2}} \right) \tag{15}$$

And in the limit of $t \to \infty$ Eq. (15) has an asymptotic behavior:

$$\left. \frac{Q_t}{l \cdot C_1} \right|_{t \to +\infty} = \frac{D \cdot t}{l^2} - \frac{1}{6} \tag{16}$$

In this concern, the time-lag value, θ_L, defined as the intercept on the t axis of the straight line which approximates this curve at long times when steady state conditions are approached, allows the calculation of the diffusion coefficient D as follows:

$$\vartheta_l = \frac{l^2}{6 \cdot D} \tag{17}$$

2.1.1 Permeation in multi-layer samples

In case of multi-layer film, the material cannot be considered as uniform and the Fick's law has to be written with a different diffusion coefficient for every layer of the sample.

Concerning the steady state of permeation, the permeability P_i of the i-th layer can be evaluated from a simple series resistance approach:

$$\frac{1}{T.R.} = \sum_i \frac{1}{(T.R.)_i} = \sum_i \frac{l_i}{P_i} \tag{18}$$

The analysis of the kinetics of diffusion was developed by Barrie [2] who adopted the solution given by Jaeger [3] to the analogous thermal problem and the diffusivities of a three layers film can be evaluated using the time-lag technique:

$$\vartheta_{123}=\frac{1}{\frac{l_1}{P_1}+\frac{l_1}{P_2}+\frac{l_3}{P_3}}\cdot\left[\frac{l_1^2}{D_1}\left(\frac{l_1}{6P_1}+\frac{l_2}{2P_2}+\frac{l_3}{2P_3}\right)+\frac{l_2^2}{D_2}\left(\frac{l_1}{2P_1}+\frac{l_2}{6P_2}+\frac{l_3}{2P_3}\right)+\right]$$
$$+\frac{1}{\frac{l_1}{P_1}+\frac{l_1}{P_2}+\frac{l_3}{P_3}}\cdot\left[\frac{l_3^2}{D_3}\left(\frac{l_1}{2P_1}+\frac{l_2}{2P_2}+\frac{l_3}{6P_3}\right)+\frac{P_2 l_1 l_2 l_3}{P_1 D_2 P_3}\right] \quad (19)$$

where θ_{123} is the time lag resulting in a permeation test on the three layer sample.

2.2 Sorption

In case of sorption experiment, the specimen is immersed in a gaseous phase at uniform concentration, so the problem is still described by the Fick's law, but a different set of boundary and initial conditions has to be considered. In the present work, differential sorption tests are performed by means of a pressure-decay technique: the solubility, or the concentration, in terms of penetrant mass absorbed per sample mass, is evaluated measuring the decay in pressure of the gaseous phase in a known volume. The test starts with a certain concentration in the gaseous phase which decreases due to the sample absorption, until when the net flux through the membrane is zero and the concentration is thus uniform within the sample.

If $M_0^{(i)}$ is the initial mass in the gas phase in the pre-chamber at the *i*-th step, and $M_\infty^{(i)}$ is the mass in the gas phase at the equilibrium in the system pre-chamber and sample-chamber (in the end of the *i*-th step), being m_p the initial mass of the specimen (dry), the penetrant concentration is described by:

$$c^{(i)}-c^{(i-1)}=\frac{M_\infty^{(i)}-M_0^{(i)}}{m_p}=\frac{M_\infty^{(i)}-M_\infty^{(i-1)}}{m_p} \quad (20)$$

The concentration at the equilibrium of the fist step can be evaluated by means of measurement of the experimental pressure; in the ideal gas approximation, the initial and final values of the pressure, p_0 and p_∞, knowing the volumes of the two chambers (V_{C01}, volume of the pre-chamber and V_{C02}, volume of the sample-chamber), give the gas or vapor solubility in the sample:

$$M_0^{(1)} = \frac{p_0^{(1)} \cdot V_{C01}}{RT} \cdot M_{W,pen} \tag{21}$$

$$M_\infty^{(1)} = \frac{p_\infty^{(1)} \cdot (V_{C01} + V_{C02})}{RT} \cdot M_{W,pen} \tag{22}$$

More generally, in the following steps, to evaluate $M_0^{(i)}$ at the *i*-th step:

$$M_0^{(i)} = \frac{(p_0^{(i)} \cdot V_{C01} + p_\infty^{(i-1)} \cdot V_{C02})}{RT} \cdot M_{W,pen} \tag{23}$$

$$M_\infty^{(i)} = \frac{p_\infty^{(i)} \cdot (V_{C01} + V_{C02})}{RT} \cdot M_{W,pen} \tag{24}$$

Where $p_\infty^{(i-1)}$ is the equilibrium pressure of the (*i*-1)-th step and $p_0^{(i)}$ the initial pressure at the following one (*i*-th). As obvious, the above expression has a general validity, and so, in order to analyze the kinetics of diffusion, the instant value of the absorbed mass can be determined from the pressure $p(t)$ at time t.

In a pressure-decay experiment, the pressure in the gas phase changes and the concentration on the interface solid-gas is expected to vary due to the mass absorbed in the specimen: the hypothesis of boundary condition constant in time is thus not longer correct and the problem has to be properly reformulated.

Considering a 2 l thick slab, if a is the ratio between the volume of the gas phase and the membrane surface, the conditions at the boundaries become:

$$\frac{a}{K}\frac{\partial c}{\partial t} = \mp D\frac{\partial c}{\partial x}, \qquad x = \pm l, \qquad t > 0. \tag{25}$$

This equation is a mass balance and states that the amount of penetrant absorbed in the sample at the surfaces $x = \pm l$ is equal to the mass that left the gas phase. The partition factor K is the ratio between the concentration in the gas phase and the one within the specimen. In the hypothesis of ideal gas, given R the ideal gas constant and S the gas solubility in the sample, the partition factor is given by:

$$K = SRT \tag{26}$$

The solution to this problem was developed by Crank [1] by means of Laplace transforms; the instantaneous mass absorbed in the sample is then expressed as follows:

$$\frac{M(t)}{M_\infty} = 1 - \sum_{n=1}^{\infty} \frac{2\alpha(1+\alpha)}{1+\alpha+\alpha^2 q_n^2} e^{-Dq_n^2 t/l^2} \tag{27}$$

where α is the ratio $a/(K\ l)$ between the volume of the solution and the membrane, while q_n are the positive, non zero, solutions of the equation:

$$\tan q_n = -\alpha q_n \tag{28}$$

The aforementioned solution is correct in the case of initially dry sample while in the following steps, it has to be modified:

$$\frac{M_t^{(i)} - M_0^{(i)}}{M_\infty^{(i)} - M_0^{(i)}} = 1 - \sum_{n=1}^{\infty} \frac{2\alpha(1+\alpha)}{1+\alpha+\alpha^2 q_n^2} e^{-Dq_n^2 t/l^2} \tag{29}$$

From the best fitting of Eq. (29) in the experimental data, the diffusion coefficient D can be evaluated.

For the study of gas and vapor solubility in multilayer samples, a mass additive rule was considered to identify the individual contributions of each layer to the water uptake:

$$c_{eq,tot} = \sum x_i \cdot c_{eq,i} \tag{30}$$

where $c_{eq,tot}$ is the equilibrium water concentration in the sample, $c_{eq,i}$ is the equilibrium water concentration in each layer i and x_i the corresponding mass fraction.

2.3 Apparatus description

2.3.1 Permeometer

The permeability of pure gases in the various films was investigated by using a closed-volume manometric apparatus, especially designed to characterize ultra barrier films and shown in Figure 2-1.

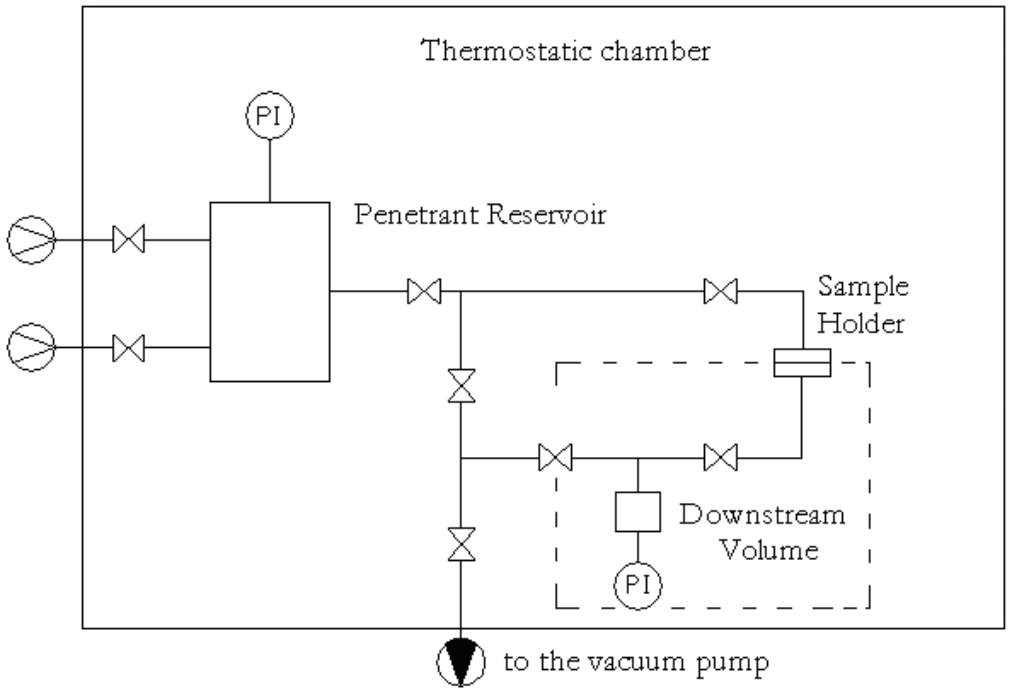

Figure 2-1, Layout of the permation apparatus.

A pressure difference is maintained across the two sides of the sample and the amount of mass permeated is calculated measuring the pressure increase in a closed volume of known dimensions at constant temperature. As observed in Figure 2-1, the apparatus is divided, by the sample holder, in two different volumes; the downstream side is kept as small as possible to have the highest sensitivity (30 ± 1.5 cm^3), while in the upper part there is a relatively big reservoir (about 2 L) where the probe gas is filled. The specimen, whose permeation area is about 9.6 cm^2, is carefully clamped in the sample holder where 2 O-rings in Viton allow good sealing.

To ensure the evacuation of any chemical species absorbed in the sample before every test, an ultra-vacuum pump is used, which guarantees absolute pressure values in the order of magnitude of 10^{-3}-10^{-4} mbar. In the downstream volume, a high-resolution manometer gives the instantaneous values of the pressure that gives the amount of mass permeated. The manometer works in the range 0-10 mbar with a sensitivity of 0.001 mbar and with an accuracy of 0.15% of the reading. In order to have the correct value of the driving force, the differential pressure across the membrane, another manometer is placed in the upstream volume, on the reservoir, whose values are

supposed to be constant while the tests are carried out. The entire apparatus is then kept in a thermostatic chamber to have a constant temperature.

The experimental procedure starts by setting the specimen in the sample-holder and it is then pre-treated to evacuate the chemical species already absorbed in the membrane, by connecting the chamber with the vacuum pump for a sufficiently long time, depending on its properties and thickness, to make sure that the sample will be completely dry.

After this treatment, the experiment starts by closing the valve on the downstream volume, and the reservoir is connected with the membrane: the differential pressure across the specimen is therefore accomplished.

In the first part of the test, the flux trough the membrane increases until the material is saturated and the steady state is reached and the experiment can be thus finished; an example of a permeation output is reported in Figure 2-2.

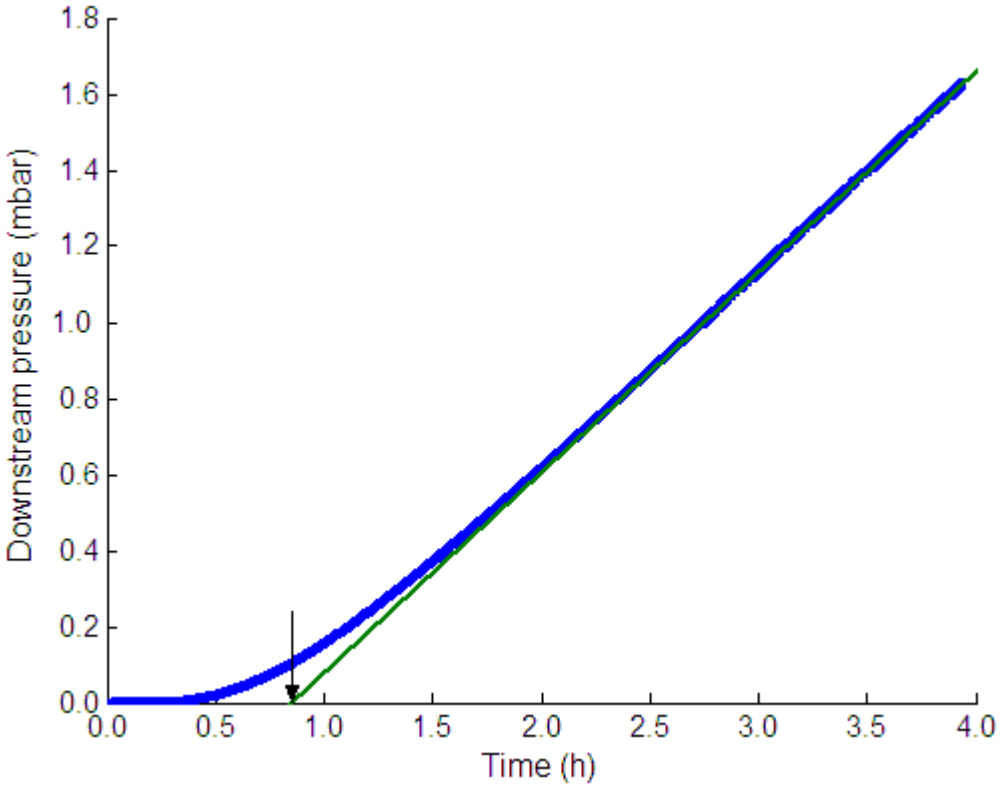

Figure 2-2, Permeation experiment output.

Every data point (in terms of *T.R.* and time-lag) is collected at least twice to assure a complete repeatability and reliability of the measurements.

2.3.2 Humid permeometer

A second permeation apparatus was then developed on the same basis of the one above described, to allow the characterization of samples in presence of humidity. Measurements of either pure water permeability or humidified gas permeability are carried out by means of the close volume manometric equipment detecting the amount of mass permeated by monitoring the pressure in a known volume. The permeation part of the apparatus is essentially the same of the one for pure gases, but a new section has been added to pre-treat the specimen at certain humidity and to ensure a flow-experiment at controlled R.H. in the upstream section, as one can see in Figure 2-3. In this concern, the sample holder has an inlet and outlet connection in the upper section, the latter provides the necessary purge to keep the desired humidity content constant during the test.

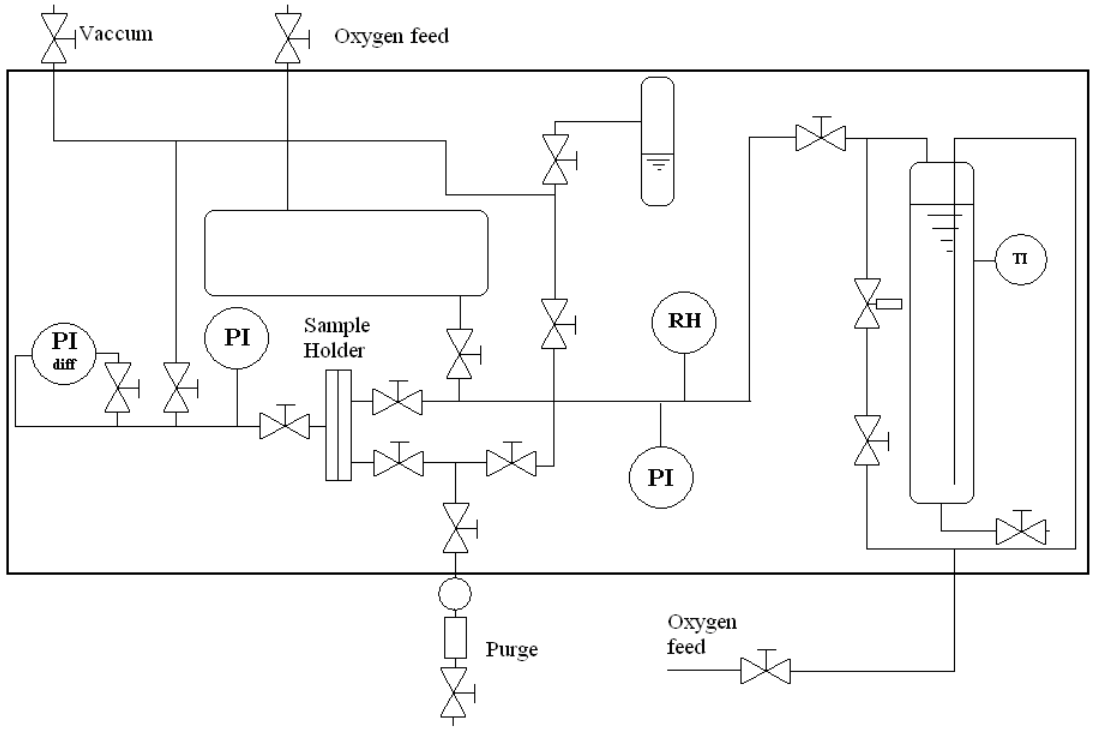

Figure 2-3, Layout of the humid permeometer apparatus.

In all cases, the specimen has to be pre-treated by connecting it with the vacuum pump for a sufficiently long time to ensure that all the chemical species therein absorbed have been evacuated. The water vapor permeability test, then, proceeds

simply as previously described for the case of pure oxygen experiments: the downstream volume is closed and the sample is connected with the water reservoir charged at the desired pressure. From the output of the test, both permeability and diffusivity can be determined from the analysis of the steady state flow and the time-lag, respectively.

On the other hand, humid gas permeation tests require a further pre-treatment of the specimen that is set at a certain water activity until equilibrium conditions have been reached. At this point, humidified gas (at the same water activity) is flowed in the upstream section and the permeation experiment can start. In this concern, after a short transient time, due to slight water pressure difference causing a water flow through the membrane, the partial pressure of water is the same in both sides, and, consequently, there is no force driving the water to cross the sample. On the contrary, the gas pressure difference causes the flow from the upstream part to the downstream volume.

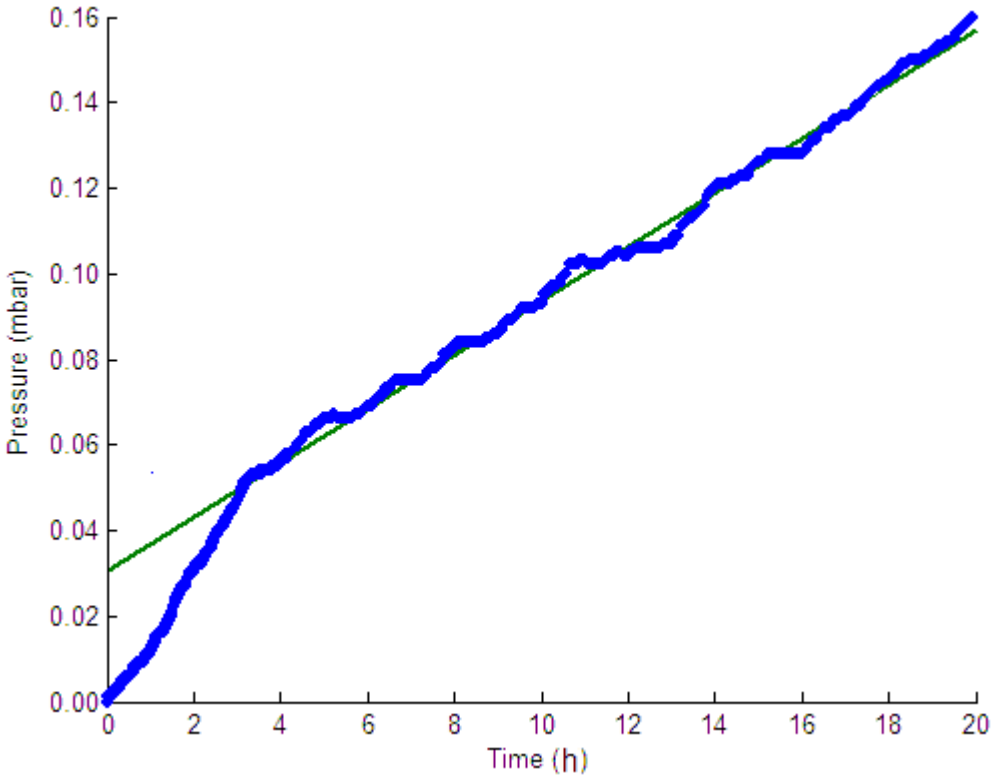

Figure 2-4, Humid permeation experiment output.

From the analysis of the increasing pressure in this volume showed in Figure 2-4, the amount of permeated gas can be evaluated as well as the gas permeability at certain humidity.

2.3.3 Pressure decay

The experimental device that has been used for differential sorption test is a pressure-decay apparatus with double chamber, in which the amount of absorbed gas or vapor is measured as decay of pressure of the gaseous phase is a known volume. As reported in Figure 2-5, the system is characterized by a pre-chamber where the penetrant is charged at a certain pressure controlled by a high precision manometer (range 0-100 or 0-1000, with a resolution of 0.01 and 0.1 mbar, respectively) and a second chamber where the specimen is set.

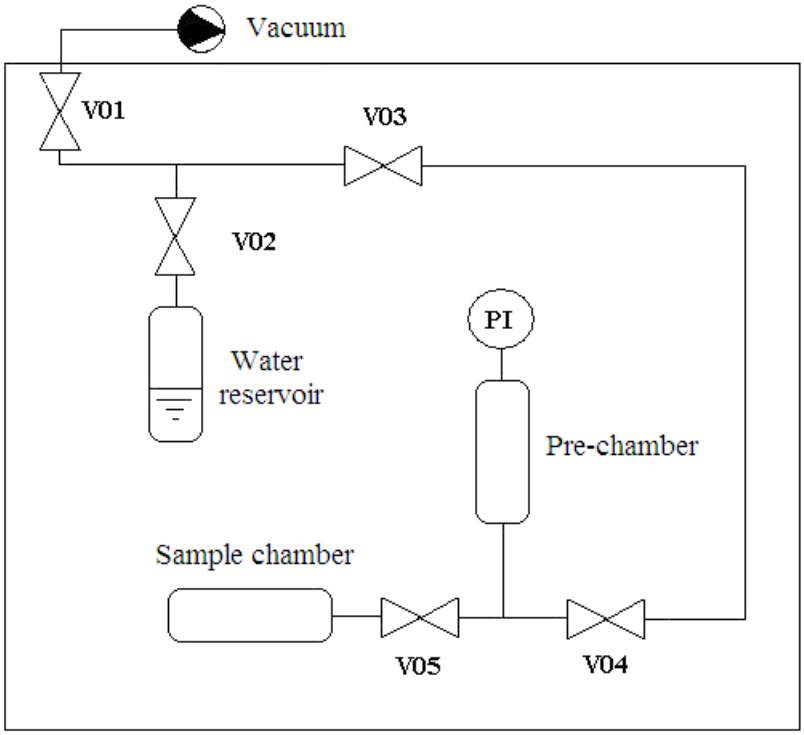

Figure 2-5, Layout of the pressure-decay apparatus.

The specimen is at first weighed with an electronic balance with a precision of ± 5 μg and it is then set within the sample-chamber, which, in turn, is sealed with an aluminum gasket; in order to evacuate the chemical species present in the material,

the sample is pre-treated by connecting the chamber with the vacuum pump for a sufficiently long time.

At the beginning, the pre-chamber is filled with the probe gas up to a certain pressure and, when the valve between the two chambers is opened, the experiment starts. The pressure suddenly drops to a specific value due to the volume expansion, easily predictable in the assumption of ideal gases; then the penetrant molecules go into the specimen causing the pressure decay: from its evaluation the mass absorbed is determined. After a certain time, steady state conditions are reached, the penetrant in the sample is at the equilibrium with the one in the gas phase and the pressure does not change anymore; an example of the sorption output is reported in Figure 2-6.

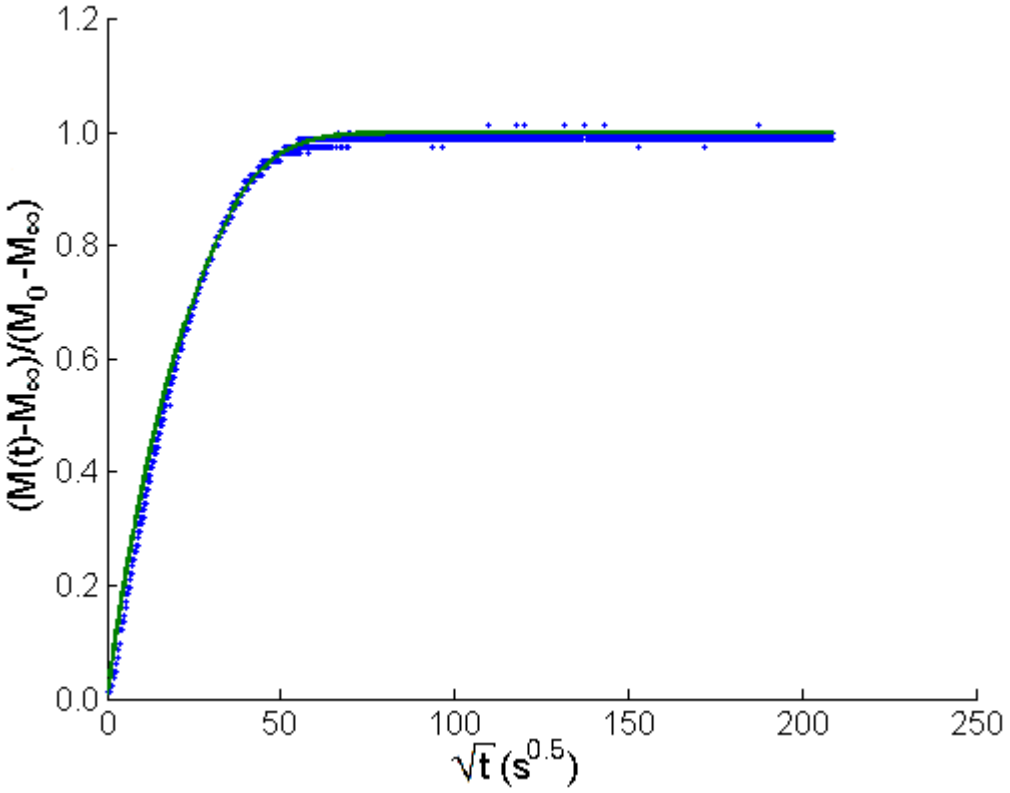

Figure 2-6, Sorption experiment output.

Closing then the valve between the chambers, it is possible to repeat this procedure increasing the pressure for the following sorption step. A sufficient number of steps has been carried out in order to carefully describe the entire range of activity and to obtain an accurate sorption isotherm for the system analyzed.

The complete test is repeated at least twice to make sure of the repeatability of the results.

2.4 Material description

2.4.1 Organic-inorganic hybrids

The organic-inorganic hybrid samples analyzed in this section were developed by the Department of Materials and Environmental Engineering at the University of Modena and Reggio Emilia (set 1.a and 1b, PE-PEG based systems) and by the Department of General Chemistry, Inorganic Chemistry, Analytic Chemistry and Physical Chemistry at the University of Parma (set 2, PVOH based systems) within the Italian framework funded by the Project "Organic-inorganic hybrid Coatings for Packaging innovative Films".

2.4.1.1 PE-PEG/Si-SiO_2

A bubble extruded LDPE thin film, 45 μm thick, supplied by Polimeri Europa S.p.A., was used as polymer substrate for hybrid coatings. High purity tetraethoxysilane (TEOS, Aldrich), 3-isocyanatopropyltriethoxysilane (ICPTES, Fluka), ethanol (EtOH, Carlo Erba), tetrahydrofuran (THF, Sigma-Aldrich), hydrochloric acid 37% solution (Sigma-Aldrich), sodium hydroxide pellets (Sigma-Aldrich), two different monohydroxy terminated polyethyleneblock-poly(ethylene glycol) copolymers containing 50 and 80 wt.% of ethylene oxide and having M_n = 920 and 2250 g/mol, respectively (PE-PEG(50) and PE-PEG(80), Aldrich) were also used as received without further purification.

The triethoxysilane terminated copolymers PE-PEG(*n*)-Si triethoxysilane terminated copolymers were prepared as follows [4-5]. ICPTES was reacted in bulk with the PE-PEG hydroxyl terminated copolymers in molar ratio of 1.1:1. The reaction was carried out in a 50 mL glass flask with magnetic stirring, at 120°C, for about 3 h. The progress of the reaction was monitored using FT-IR spectroscopy by following the

increase of the strong absorption band of the urethane groups (at about 1760 cm^{-1}) deriving from the reaction of the hydroxy groups with isocyanate groups and the disappearing of the band related to isocyanate groups (at 2300 cm^{-1}). It was found that, under the experimental conditions used in this study, the reaction goes to completion within 3 h. The expected structures of the final products, respectively coded as PE-PEG(50)-Si and PE-PEG(80)-Si (in which the numbers represent the weight percentage of ethylene oxide in the commercial copolymers) have been confirmed also by the ^{1}H NMR [4].

The hybrid coatings of this series (set 1.a) were prepared by dissolving TEOS and triethoxysilane terminated copolymers, PEPEG(*n*)-Si, in warm THF under magnetic stirring at the concentration of 30% wt./v. Water (for the hydrolysis reaction), EtOH (to make the system homogeneous) and catalyst (HCl or NaOH) were added at the following molar ratios with respect to the overall ethoxide groups (deriving both from TEOS and functionalized copolymers): EtO-:H2O:EtOH:catalyst = 1:1:1:0.05, and finally partially cured in a closed vial at 60°C for 2 h before deposition on the LDPE substrate.

The preparation of PE-PEG(80)-Si/SiO_2 1:1 hybrid is reported in the following as an example: 0.70 g of a PEPEG(80)-Si and 2.30 g of TEOS were added to 10 mL of THF until a homogeneous solution was obtained. Then 2.92 g of a mixture of EtOH, water and HCl (in molar ratio 1:1:0.05) were added under stirring.

Most of the coatings were prepared using HCl as catalyst, and the final hybrids were coded as XN, in which X is a letter indicating the molecular weight of the organic component (H = high, L = low) and N is a figure corresponding to the nominal weight percentage of inorganic component, calculated assuming the completion of the hydrolysis and condensation reactions during the sol-gel process.

Other samples were prepared using either a basic catalyst (NaOH) or a pure organic phase as the coating. Deposition and thermal curing of polymer-silica hybrids onto PE substrate polymer/TEOS homogeneous solutions prepared according to the procedure previously described were deposited onto LDPE films (130 x 130 mm) by spin-coating using a spin rate of 1000 rpm for 30 s.

Spin-coating is useful to obtain very thin films (typically 0.1 - 1 μm) just on one side of the substrate, and this application technique was used in this work as it is known to

lead to uniform thickness over wide surface area, thus making permeability measurements more reliable. All coated films were obtained using LDPE films washed in methanol before coating application, without any previous surface treatment. The samples, after deposition, were subjected to a thermal post-treatment at 60°C for 24 h in an air-circulating oven.

The resulting network molecular structure and morphology are dependent on the reaction conditions and in particular on the kind of catalyst used (acidic or basic) and on reaction temperature and time. Under acidic catalysis, highly branched silica chains grow preferably up to gelation, whereas under basic catalysis silica particles grow first and then form bonds, leading to gelation in the last part of the process. It is also useful to emphasize that, due to molecular constraints, Si-O-Si connectivity is usually far from that expected by a complete condensation reaction and is typically about 80-85% of the theoretical values [6-8]. This means that a significant amount of silanol groups (Si-OH) are included in the final hybrid material along with siloxane bridges, and their capability to form hydrogen bonds with the included polymer can play a relevant role with respect to the polymer chain mobility within the organic domains, where oxygen diffusion is expected to occur.

Coatings with different organic-inorganic ratios were prepared using PE-PEG-Si block copolymers and silica from TEOS, in order to assess the effect of parameters such as their composition and the molecular weight of the organic phase. The coatings were applied to the LDPE film without any previous surface treatment, as it has been previously demonstrated that they are able to lead to good adhesion to commercial LDPE films [4]. Because of the presence of the trialkoxysilane terminal groups, PE-PEG-Si is expected to form covalent bonds with the inorganic precursor, TEOS. This in turn is expected to favor the formation of organic-inorganic nano-sized domains with extended interface [9]. Indeed, all the coated films were as transparent as the original LDPE film, supporting the hypothesis of formation of nano-sized domains.

Different PE-PEG-Si/TEOS weight ratios (from 33% to 67% of silica) were used to investigate the role of the organic and inorganic components on the gas transport behavior.

In all cases, the solution was allowed to react for a given time before being applied by spin-coating onto LDPE films, and the same post-application thermal treatment was

also performed on all coated films. In order to obtain reproducible and uniform coatings, the initial solutions were applied to the plastic films by spin coating, leading to rather small thickness values (0.5 - 1 μm). No significant defects were detected on the surface at visual inspection and a quite good adhesion was observed for all samples, as attested by the SEM investigation of the cross-sectional view of the fracture surfaces (fractured in liquid nitrogen) of the coated films (see Figure 2-7 as an example). Due to the mild curing conditions used, no deformation was observed in the coated LDPE films.

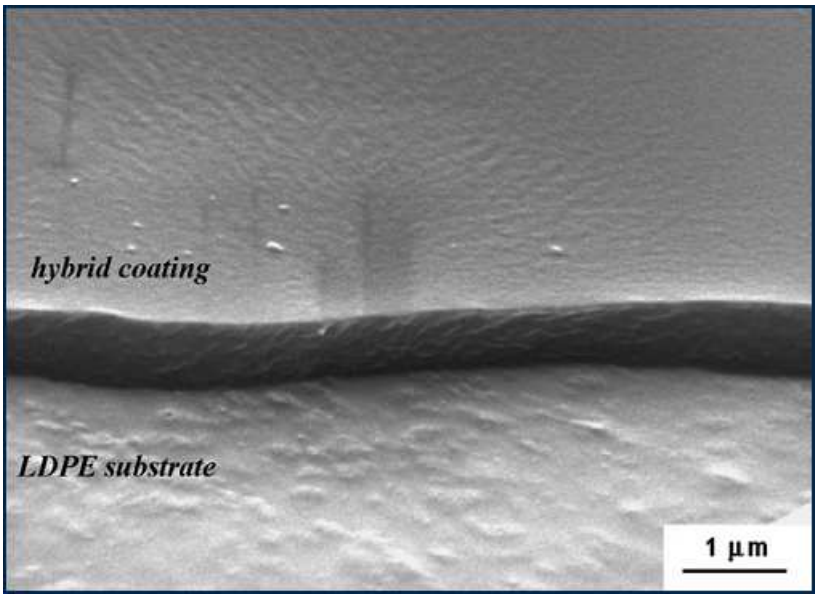

Figure 2-7, SEM micrograph of the edge view of LDPE film coated with H50 hybrid coating.

Table 2-1 summarizes the main composition data for all the hybrid coatings tested and reports data about the film thickness, as measured by SEM from the cross-sectional view of the coated films. The coating thicknesses of all the samples inspected are quite uniform over the surface of each sample, and range from 0.72 ± 0.05 μm for the coating with high inorganic content (67%), to 1.00 ± 0.08 μm for the coating with low inorganic content (33%) (Table 2-1).

It is expected that a critical role on oxygen permeability is played by the final morphology, which in turn is affected by several variables, including polymer molecular weight and type of catalyst used. Two PE-PEG-Si copolymers with different molecular weights were used as organic phase, and the coatings were prepared either under acidic (HCl) or basic (NaOH) catalysis.

Table 2-1, List of uncoated and coated LDPE films analyzed (set 1.a).

Code	Sample	Film thickness μm	Coating characteristics		
			O/I ratio	**Silica content** % wt.	**M_n (PE-PEG)** g/mol
LDPE	uncoated	45	-	-	-
H67	coated PE-PEG-Si/SiO_2	45 + 0.72	1:2	67	2250
H50	coated PE-PEG-Si/SiO_2	45 + 0.82	1:1	50	2250
H33	coated PE-PEG-Si/SiO_2	45 + 1.00	2:1	33	2250
L67	coated PE-PEG-Si/SiO_2	45 + 0.72	1:2	67	920
L50	coated PE-PEG-Si/SiO_2	45 + 0.82	1:1	50	920
L33	coated PE-PEG-Si/SiO_2	45 + 1.00	2:1	33	920
H00	coated PE-PEG	45 + 5.0	-	-	2250
H50B	coated PE-PEG-Si/SiO_2 (basic catalysis)	45 + 0.82	1:1	50	2250

A second series of samples (set 1.b) was specifically developed by adding a new component with a low permeability characteristic, poly(4-hydroxystyrene), PHS, to the copolymer PE-PEG constituting the organic phase in order to improve further the oxygen barrier effect [10].

This component, the TEMPO-terminated PHS, was prepared by living free radical polymerization in the presence of 2,2,6,6-tetramethylpiperidinyl-1-oxy (TEMPO) as shown in the reaction scheme reported in Figure 2-8 [11].

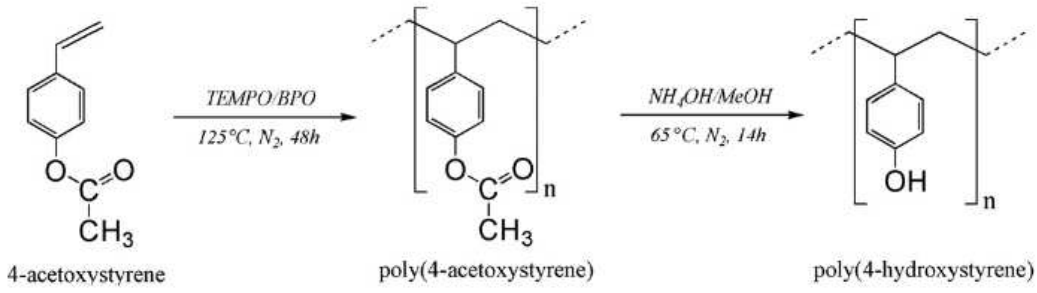

Figure 2-8, Preparation of poly(4-hydroxystyrene) from 4-acetoxystyrene.

Briefly, 4-acetoxystyrene (5.0 g, 30.9 mmol) was placed in a 50 mL round bottom flask and purged under nitrogen. The initiating system (TEMPO/BPO molar ratio 1/ 0.77) was then added to get the desired molecular weight. For example, to obtain a molecular weight of approximately 16000 g/mol, a molar ratio of 1:100 initiator to 4-acetoxystyrene, was used. After addition of the initiator, the polymerization mixture was heated at 125°C, under nitrogen, and stirred for 48 h. The reactor was then cooled to room temperature and the polymer dissolved in acetone (15 mL), and isolated by

precipitation into *n*-hexane (100 mL). The polymer (TEMPO-terminated poly(4-acetoxystyrene)) was then filtered, washed with *n*-hexane, and dried in a vacuum oven overnight at 50°C. To a slurry of poly(4-acetoxystyrene) (5.0 g, 31 mmol of acetoxy groups) in refluxing methanol (40 mL), ammonium hydroxide (2.5 g, 69 mmol) dissolved in water (7 mL) was added drop wise over 15 min under nitrogen. The reaction mixture was refluxed for 14 h, to allow the polymer dissolution. The solution was then cooled to room temperature, and the polymer recovered by precipitation into hexane (100 mL), filtered, washed with water, and dried in a vacuum oven overnight at 50°C. Typical yields of poly(4-hydroxystyrene) were 64-72%. The expected structures of the final products have been confirmed by the ^{1}H NMR (d 1.87 (m, CH_2-CH-Ph), 2.76 (m, CH-Ph), 6.65 (m, Ph-o-OH), 7.33 (m, Ph-m-OH), 9.83 (s, OH)). A number-average molecular weight of 14400 g/mol, was determined from ^{1}H NMR by comparison of the signal at 2.76 ppm (1 proton for each repeating monomeric unit) with the methyl signal of TEMPO at 1.15 ppm (12 protons) [12].

Then, the hybrid coatings were prepared as above described by dissolving TEOS and PE-PEG-Si in THF under magnetic stirring at the concentration of 30% w/w. Water (for the hydrolysis reaction), EtOH (to make the system homogeneous) and HCl (as catalyst) were added at the following molar ratios with respect to the overall ethoxide groups (deriving both from TEOS and functionalized copolymers): EtO-:H2O:EtOH:HCl = 1:1:1:0.05 and finally partially cured in a closed vial at 60°C for 2 h before spin-coating deposition on the LDPE substrate.

Some LDPE films were also subjected to plasma treatment (in air) using a 13.56 MHz radiofrequency reactor, Plasmod 1645, supplied by March Instruments Inc. The reactor pressure was 0.1 Torr (~13 Pa), the gas flow rate was 7.7 cm^3/min, the power was set at 15 W and the treatment time was 2 min.

Finally, polymer/TEOS homogeneous solutions prepared according to the procedure previously described were deposited onto LDPE films (130x130 mm) by spin-coating using a spin rate of 1000 rpm for 30 s. After deposition, samples were subjected to a thermal post-treatment at 60°C for 24 h in an air-circulating oven. Samples of this series have bee listed in Table 2-2.

Table 2-2, List of uncoated and coated LDPE films analyzed (set 1.b).

Sample		Film thickness μm	Component wt fractions		
code	**coating**		**PE-PEG**	**SiO_2**	**Additive (type [c])**
LDPE	Uncoated LDPE	45	-	-	-
H50-M05	PE-PEG-Si/SiO_2/MA	45 + 0.80	0.475	0.475	0.05 (MA)
H50-M10	PE-PEG-Si /SiO_2/MA	45 + 0.88	0.45	0.45	0.10 (MA)
H50-M20	PE-PEG-Si/SiO_2/MA	45 + 0.85	0.40	0.40	0.20 (MA)
H33-S22	PE-PEG-Si/SiO_2/PHS	45 + 1.00	0.45	0.33	0.22 (PHS)
H67-S11	PE-PEG-Si/SiO_2/PHS	45 + 0.75	0.22	0.67	0.11 (PHS)
H33-S44	PE-PEG-Si/SiO_2/PHS	45 + 1.00	0.22	0.33	0.44 (PHS)
H00	PE-PEG	45 + 5.0	1.00	-	-
H00-S20	PE-PEG/PHS	45 + 5.0	0.80	---	0.20 (PHS)
H00-S40	PE-PEG/PHS	45 + 5.0	0.60	---	0.40 (PHS)
H50-DL	PE-PEG-Si/SiO_2 first layer PVOH-Si/SiO_2 second layer	45 + 1.00	0.50	0.50	-
		+ 0.85	-	0.30	0.70
H67P	PE-PEG-Si/SiO_2 - Plasma[b]	45 + 0.72	0.33	0.67	-
H50P	PE-PEG-Si/SiO_2 - Plasma[b]	45 + 0.82	0.50	0.50	-
H33P	PE-PEG-Si/SiO_2 - Plasma[b]	45 + 1.00	0.67	0.33	-

(a) Double layered film
(b) The coating was deposited on plasma treated LDPE films.
(c) MA = malic acid; PHS = poly(4-hydroxystyrene).

2.4.1.2 PVOH/Si-SiO_2

The second system (set 2) that has been considered was developed using an ultra barrier polymer such as PVOH as organic phase of the hybrid. In this concern, fully hydrolyzed polyvinyl acetate (PVAc) (97-100 % of the acetate groups substituted) or partially hydrolyzed PVAc (86-89% of the acetate groups substituted) can be used: both grades are commercially available. The inorganic Si-SiO_2 groups were obtained by the addition of TEOS [13].

An aqueous or hydro alcoholic solution comprising PVOH and the alkoxide in variable concentrations, depending on the desired final O/I ratio, was prepared. In order to catalyze the hydrolysis and condensation reactions, the solution was adjusted to slightly acidic values by adding a small amount (0.03-1 wt%) of HCl. In these conditions, the components reacted according to the classical sol-gel route shown in Figure 2-9 [14].

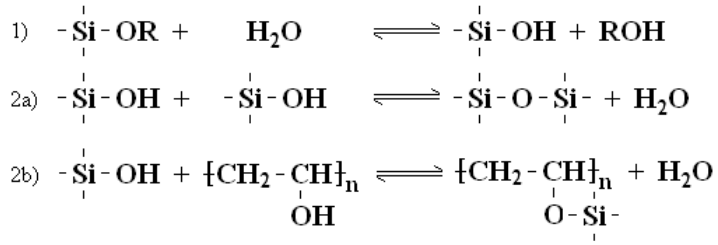

Figure 2-9, PVOH-TEOS sol-gel reaction scheme.

In the scheme it can be seen that, after hydrolysis, the silanol groups Si-OH originated from TEOS may react according to two competitive condensation reactions: *i*) with another silanol group, to form Si-O-Si; *ii*) with the hydroxyl groups of PVOH, allowing the formation of the hybrid network. In the literature, there is strong evidence that supports the hypothesized reaction scheme and that a strong interconnection, represented either by a covalent or a hydrogen bond, is present between the organic and inorganic domains in the final systems [15-21].

The sol-gel solution was then deposited on the polymer substrates by dip coating at different velocities (from 4.2 to 11.6 cm/min) achieving similar results in terms of adhesion and resistance. This technique allowed to obtain samples coated on both sides, while for mono-layered laminates a roll coating technique was employed, that produced good results in terms of adhesion. The hybrid layers obtained in this way were colorless and perfectly transparent.

The final configuration was then analyzed with SEM microscopy to measure the coating thickness, which was determined to be equal to 1 ± 0.1 μm on each side of the sample for bi-coated samples. Figure 2-10 reports a SEM micrograph of a coated PET sample, where the coating layer has been purposively detached to allow the determination of its absolute thickness.

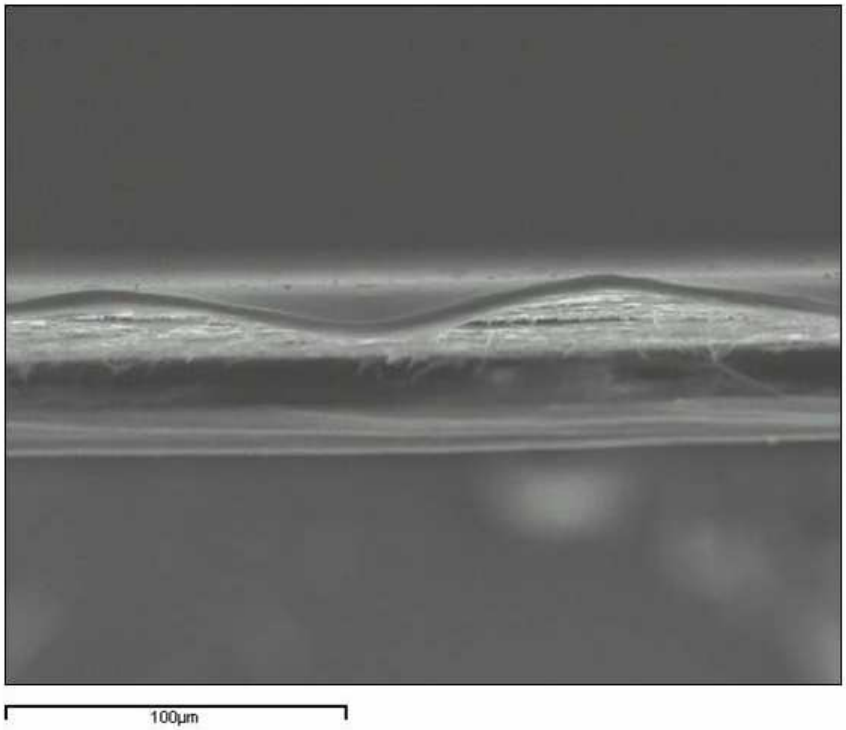

Figure 2-10, SEM micrograph of the edge view of PET film coated with PVOH based hybrid coating.

The final weight percentage fraction of inorganic phase in the hybrid layers inspected was equal to about 30% for the coating named Co1 and to about 50% for coating Co2. Also coatings formed by the organic phase only (PVOH) were obtained and named Co0. The three different coatings were applied onto a 36 µm thick PET substrate: due to the polar nature of this support, they can be dipped into the hydrophilic sol-gel solution without any special surface treatment, obtaining a good adhesion. Other polymeric supports, namely oriented poly-propylene (oPP) cast poly-propylene (cPP), low density poly-ethylene (LDPE) and a blend of LLDPE and LDPE (COEX), were coated with the hybrid named Co1 and, due to their hydrophobic nature, treated with cold plasma before deposition in order to improve adhesion. The plasma treatment was performed in air at 30 W; the duration of treatment was varied from 10 s to 30 s, obtaining similar adhesion strength. The machine used is a "Colibrì" device manufactured by Gambetti Vacuum SrL (Binasco, Mi, IT) that operates within the absolute pressure range of 0.1 - 1 mbar.

A list of the multilayer samples prepared and characterized is provided in Table 2-3 where the thickness and type of polymeric support is reported, as well as the composition of the hybrid coatings in terms of final polymer/Si-SiO_2 ratio.

Table 2-3, List of uncoated and coated polymer films analyzed (set 2).

	Substrate		Coating	
Code	**Type**	**Thickness** (μm)	**O/I ratio** (final)	**Thickness** (μm)
PET-Co0	PET	36	100/0	1+1
PET-Co1	PET	36	70/30	1+1
PET-Co2	PET	36	50/50	1+1
oPP-Co1	oPP	30	70/30	1+1
oPP1-Co1	oPP	30	70/30	1
cPP-Co1	cPP	75	70/30	1+1
LLDPE-Co1	LLDPE	110	70/30	1+1
COEX-Co1	LLDPE/LDPE blend	65	70/30	1+1

2.4.2 Microfibrillated cellulose

The samples of microfibrillated cellulose here described were prepared at Risø, National Laboratory for Sustainable Energy in Copenhagen (Denmark) and were developed within the European framework Sustainpack.

Two generations of MFC were developed by following two different preparation processes. For the manufacture of MFC generation 1 (MFC G1), a commercial bleached sulfite softwood pulp (Domsjö ECO Bright, Domsjö Fabriker AB, Sweden) consisting of 40% pine (*Pinus sylvestris*) and 60% spruce (*Picea abies*) with a hemicellulose content of 13.8% and a lignin content of 1% was used. MFC generation 2 (MFC G2) was prepared from a commercial sulfite softwood-dissolving pulp (Domsjö Dissolving Plus; Domsjö Fabriker AB, Sweden) with a hemicellulose content of 4.5% and a lignin content of 0.6% at STFI-Packforsk (Stockholm, Sweden). For both pulps, the hemicellulose content was assessed as solubility in 18% NaOH and the lignin content was estimated as 0.165*Kappa number using the SCAN C 1:00 test procedure [22]. Both pulps were thoroughly washed with deionized water before use. Glycerol (99% GC, Sigma Aldrich Chemie GmbH, Steinheim, Germany) was used as a plasticizer.

MFC G1 was prepared using a combined refining and enzymatic pre-treatment followed by a high pressure homogenization described in detail by Pääkkö et al. [23], while MFC G2 was prepared via carboxymethylation pre-treatment followed by a high pressure homogenization described in detail in Wågberg et al. [24]. Due to the

different manufacturing procedures the two MFCs have different sizes and anionic charge densities. MFC 1 fibrils have diameters of about 17-30 nm, while the MFC G2 fibrils are somewhat smaller (~15 nm) [24]. The charge density was about 40 µeq/g for MFC G1 and about 586 µeq/g for MFC 2, measured using conductometric titration.

In order to be able to cast films the MFC gels were diluted with deionized water; since MFC G2 gel had much higher viscosity than MFC G1 gel, it was necessary to use approximately twice as much water in order to prepare a suspension that could be easily poured. The suspensions were stirred for about 3 hours and then approximately 60 g 1 wt% MFC G1 and 90 g 0.67 wt% MFC G2 aqueous suspension was poured into a 120 x 120 mm polystyrene Petri dish (Sigma-Aldrich, Denmark). Films were prepared by drying the cast gels in an incubator with controlled humidity (Climacell 111, MMM Medcenter Einrichtungen GmbH, Planegg, Germany) at 45 °C and 50% R.H. for 48 hours and subsequently in a Vacucell vacuum oven (MMM Medcenter Einrichtungen GmbH at 70°C overnight. In case of plasticized films (MFC G1P and G2P) glycerol was added to the suspensions to have 33 wt% concentration in the dried films. The thickness of obtained films was measured with a Mitutoyo micrometer at 10 different spots. The complete list of the set of samples is reported in Table 2-4.

Table 2-4, List of the MFC samples inspected.

	Treatment	**Glycerol content**	**Fibril diameter** (nm)
G1	Gen. 1	0.00	17-30
G2	Gen. 2	0.00	15
G1P	Gen. 1	0.33	17-30
G2P	Gen. 2	0.33	15

2.5 Results

2.5.1 PE-PEG based hybrids

A wide investigation action has been performed in order to characterize the oxygen barrier properties of the LDPE films coated by a PE-PEG based hybrid layer. In this

concern, pure oxygen (0% R.H.) experiments have been carried out at two different temperatures, namely 35 and 50°C. The tests were performed with an upstream pressure ranging from 1 to 1.5 bar, and the data collected are averaged at least over two different permeation experiments. The uncertainty is below 5% for the steady state measurements and somewhat higher, between 10% and 15%, for the measure of the transient (time-lags).

2.5.1.1 PE-PEG/Si-SiO_2 hybrids

Concerning the results from the permeation in samples of set 1.a, at first oxygen transfer rates (*O.T.R.*) and time-lag values have been considered to evaluate the overall properties, both *O.T.R.* and θ_L are indeed dependent on the sample geometry; for multilayer films, in particular, they depend on the thickness of each layer. The obtained results are therefore reported in Table 2-5.

Table 2-5. Oxygen transfer rate and time-lag values in the various samples at 35°C and 50°C. (Maximum uncertainty: ± 2.5 % for *O.T.R.*.; ± 7.5 % for time lag values).

	35°C		**50°C**	
Code	***O.T.R.*** $cm^3(STP)/(cm^2 \cdot d \cdot atm)$	**Time-lag** s	***O.T.R.*** $cm^3(STP)/(cm^2 \cdot d \cdot atm)$	**Time-lag** s
LDPE	0.675	4.7	1.413	1.9
H67	0.390	7.3	0.916	3.3
H50	0.436	7.0	1.001	3.1
H33	0.410	7.1	1.064	2.9
L67	0.523	6.5	1.135	2.8
L50	0.538	6.7	1.201	2.9
L33	0.501	6.8	1.122	3.0
H00	0.316	6.2	0.826	1.3

However, as the LDPE film used was the same for all the samples and the coating thickness is similar for all the coatings except H00, the *O.T.R.* results give a first qualitative indication of the intrinsic effectiveness of the hybrid for the improvement of the barrier properties towards oxygen. Although the overall thickness of the hybrid coating is typically lower than 1 μm, in most cases the permeance of LDPE is reduced after addition of the coating, up to 37% at 35°C and to 29% at 50°C, as shown in Figures 2-11 and 2-12.

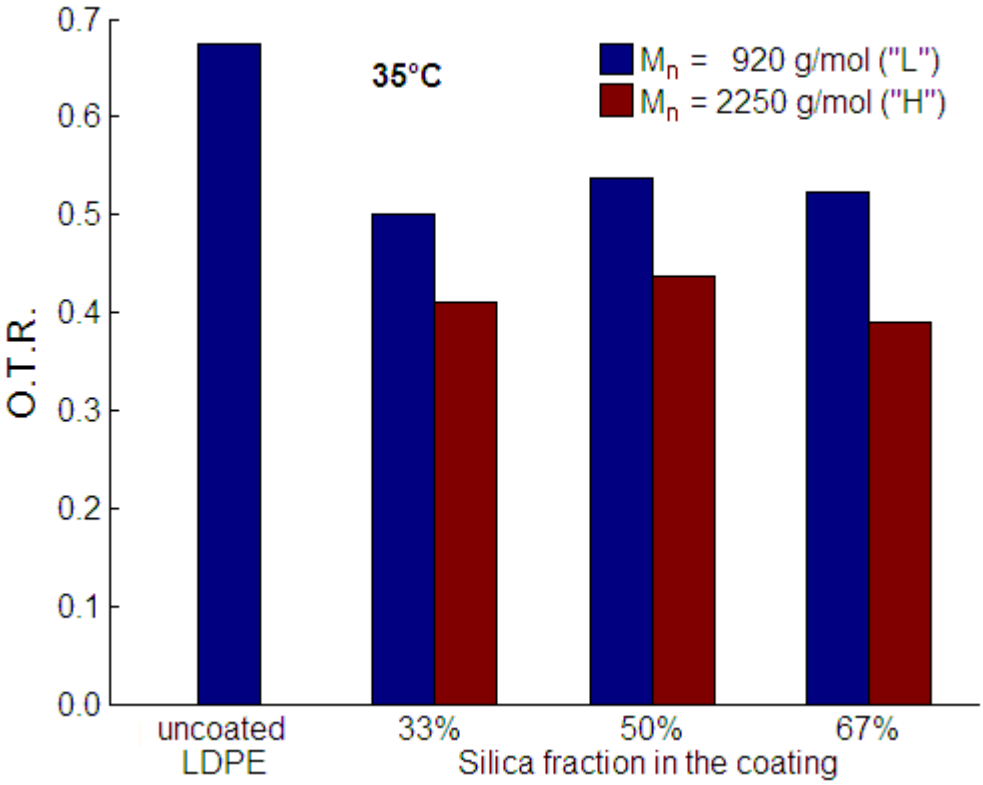

Figure 2-11, *O.T.R.* of the LDPE samples coated by PE-PEG-Si/SiO_2 hybrid at 35°C (L: M_n (PE-PEG) = 920 g/mol, H: M_n = 2250 g/mol).

It is important to note that the *O.T.R.* decrease, obtained by using 1 µm thick hybrid coating on a 45 µm thick LDPE support, is similar to that observed for plastic filled with Montmorillonite [25-27]. The hybrid coating also allows to slow down remarkably the permeation process, the time-lag value of the hybrid coated LDPE being about 60% higher than the value of pure LDPE both at 35 and 50°C due to a slower kinetics of diffusion.

When the effect of O/I ratio is considered, it should be noticed that there is not a monotonous trend of the *O.T.R.* for coatings having the same organic component (Figure 2-11). Assuming that oxygen permeation occurs mainly or exclusively within the organic phase, it is expected that a decrease of the O/I ratio would improve the barrier properties. Indeed this happens only at 50°C for samples H33, H50, H67. On the contrary, sample L33 exhibits a slightly lower *O.T.R.* value, both at 35 and at 50°C, with respect to sample L67, which contains a higher amount of inorganic phase.

However it has to be considered that *O.T.R.* results are affected by the coating thickness, which increases by increasing the organic-inorganic ratio.

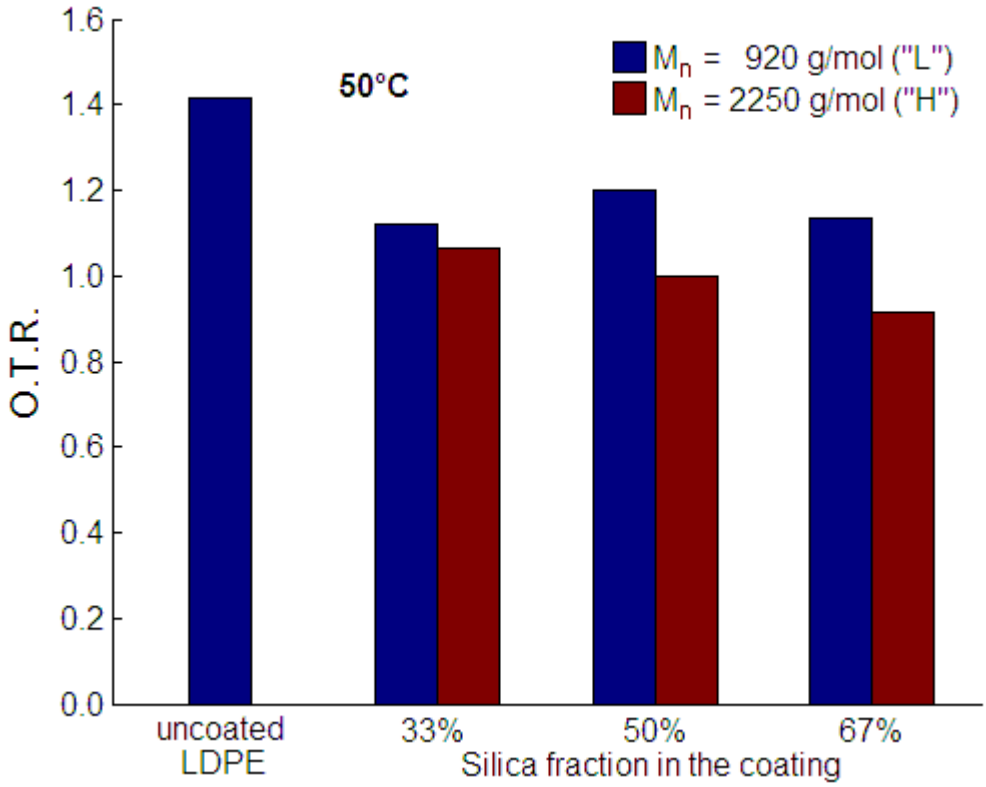

Figure 2-12, *O.T.R.* of the LDPE samples coated by PE-PEG-Si/SiO_2 hybrid at 50°C (L: M_n (PE-PEG) = 920 g/mol, H : M_n = 2250 g/mol).

Analogously, it can be stated that higher reduction in permeance measured for sample H00 is mainly due to the thickness of the coating, which is 5 times higher than for the other samples. While there is only a limited effect of the organic-inorganic ratio on both *O.T.R.* and time-lag, a significant increase of *O.T.R.* (10-20%) and a slight decrease of time-lag (about 5%) are due to the decrease of the molecular weight of the PE-PEG organic component from 2250 to 920 g/mol. The higher free volume in organic domains associated with the lower molecular weight may be responsible of the observed increase in *O.T.R.*

In order to have a more meaningful comparison between the properties of the different hybrids, the permeabilities of the pure coatings have been evaluated according to the simple series resistance formula reported in Eq. (18) and are reported in Table 2-6.

Table 2-6, Oxygen permeability in LDPE and pure coatings at 35 and 50°C (Uncertainty: ± 10 %).

Code	Permeability (35°C) Barrer	Permeability (50°C) Barrer
LDPE	4.625	9.683
H67	0.101	0.285
H50	0.154	0.428
H33	0.159	0.657
L67	0.247	0.615
L50	0.332	1.003
L33	0.296	0.831
H00	0.451	1.512

The coating in sample H67 (67 wt.% of inorganic phase, about 50% by volume), has a permeability 46 and 34 times lower than LDPE at 35 and 50°C, respectively, comparable and lower than the one of a good barrier material such as poly-vinyl chloride, and one order of magnitude lower than that of oriented poly-propylene, oPP. Also the H33 sample (with only 33 wt.% inorganic phase, about 20% by volume) has a permeability value much lower than LDPE, 29 and 15 times at 35 and 50°C, respectively.

These results, together with the data of pure PE-PEG coating, are shown in Figure 2-13: the oxygen permeability of high molecular weight samples decreases with the silica weight fraction. In particular, the permeability of pure PE-PEG, after addition of inorganic phase at loading of 33 wt.%, drops of a factor equal to 2.8 at 35°C and to 2.3 at 50°C. These factors increase up to 4.5 and 5.3, at 35 and 50°C, respectively, when the loading of silica is equal to 67 wt.%.

It is interesting to compare the permeability reduction obtained with the present hybrid material to the one that would be achieved with a traditional composite filled with a similar content of spherical silica particles, evaluated with the Maxwell model that accounts for both the reduction of surface area available for permeation and the increased tortuosity [28] and gives the following expressions for diffusivity, solubility and permeability of composites:

$$\frac{D}{D_0}=\frac{1}{1+\phi/2} \qquad \frac{S}{S_0}=1-\phi \qquad \frac{P}{P_0}=\frac{1-\phi}{1+\phi/2} \tag{31}$$

where P and P_0, D and D_0, S and S_0 are the permeabilities, diffusivities and solubilities in the hybrid and in the pure material, while ϕ is the volume fraction of the

inorganic phase, which has been estimated by assuming the density of the organic and inorganic phases equal to 1 and 2 g/cm^3, respectively.

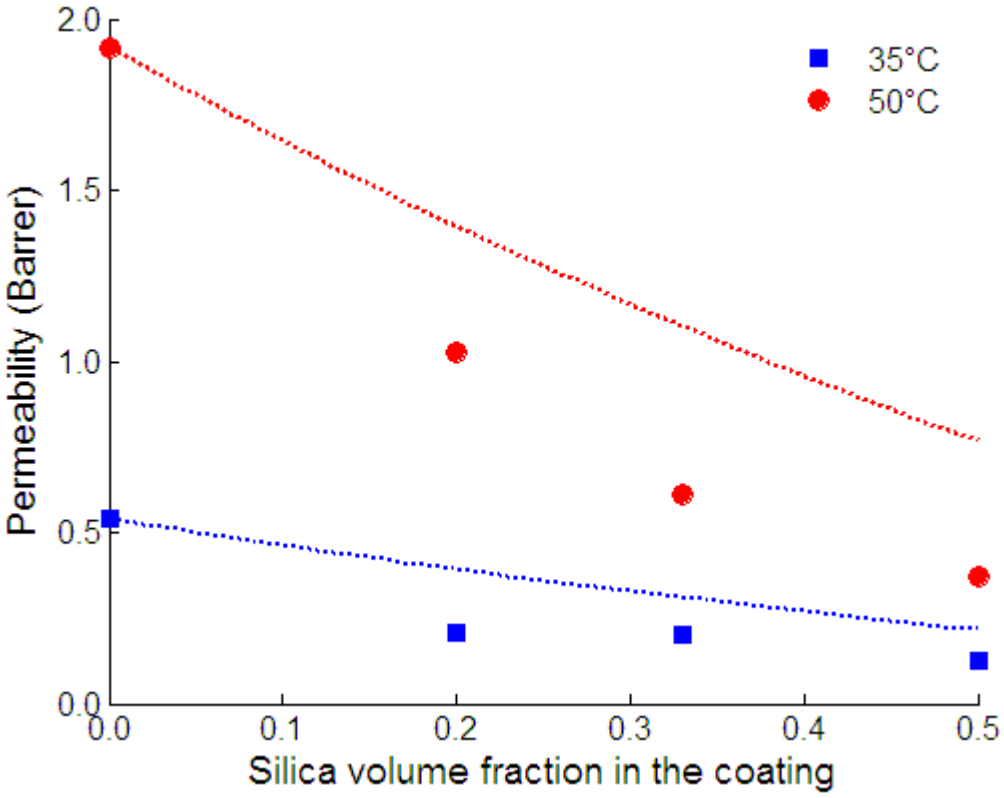

Figure 2-13, Oxygen permeability of coatings containing PE-PEG with M_n = 2250 g/mol at 35 and 50°C (dotted lines are the prediction with Maxwell model).

The data calculated from Eq. (31) are plotted as dashed lines in Figure 2-13. As one can see, the experimental points, both at 35 or 50°C, lie below the curves calculated by the Maxwell equation. This evidence suggests that, for the organic-inorganic hybrids prepared under acidic conditions, the improvement of the barrier properties is more significant than predicted by Eq. (31) for a conventional composite material in which the two phases do not interact.

As an extended interface between organic and inorganic domains is expected when coatings are prepared under acidic conditions, a synergetic effect between the two phases is supposed to occur and it is due to: *i*) covalent links between organic and inorganic domains; *ii*) hydrogen bonds between the organic and inorganic phase, as PEG segments contain ether groups able to form hydrogen bonds with the silanol

groups (SiOH). Both these factors can contribute to induce a relevant reduction of the polymer chain flexibility, even at relatively low content of silica.

Contrary to what observed for coatings prepared using acidic catalyst, no increase in barrier properties was observed for coatings prepared under basic catalysis. This evidence seems a support to the previous hypothesis, as it is well known that under basic catalysis the sol-gel process leads to inorganic domains with a particulate morphology [29], with a less extended interface between organic and inorganic domains.

The permeability reduction seems to be more remarkable at 50°C: at this higher temperature, the chain mobility in the organic phase is higher and the effect of the hydrogen bonds between PEG segments and silanol groups is reasonably more relevant. Moreover, it cannot be excluded that, at 35°C, other mechanisms, able to induce stiffening in the organic phase, may take place, such as the formation of small crystalline domains (with a melting temperature in the 30-50°C range, not detectable by experimental techniques such as DSC). This phenomenon is expected to reduce the chain mobility of the pure organic phase and the importance of immobilization-induced decrease of the permeability by the inorganic phase.

Although an Arrhenius-like correlation could describe the temperature dependence of permeability, this calculation seemed hazardous in our case, due to the limited number of temperatures investigated and also to the possible presence of a thermal transition within the thermal range inspected, as discussed above. However, on a qualitative point of view, some of these data suggest that the dependence of permeability on temperature becomes less marked with increasing inorganic content in the hybrid.

2.5.1.2 PE-PEG/PHS/Si-SiO_2 hybrids

The obtained results have also shown that the oxygen path within the coating involves mainly or exclusively the organic domains and, as a consequence, any further improvement of the coating barrier against oxygen diffusion can be achieved either by reducing the organic to inorganic ratio or by modifying the organic phase composition.

In the case of the LDPE substrate, both a further increase of the inorganic weight fraction in the coating (> 67 wt%) and the complete replacement of the PE-PEG block copolymer with PVOH or PHS would lead to a very poor adhesion.

By considering that the oxygen diffusivity within an organic medium is expected to be related to the chain mobility, that a significant concentration of silanol groups (Si-OH) is present at the interface between organic and inorganic domains, and that the ether bonds in the PEG segments can form only weak hydrogen bonds, the problem of improving the coating barrier properties has been approached firstly by the addition of products supposed to be able to form stronger hydrogen bonds.

Either low molecular weight or high molecular weight products were used for this purpose (set 1.b). Malic acid contains both hydroxyl and carboxyl groups and each molecule is potentially able to form three hydrogen bonds with ether and silanol groups. It was added to the coating formulation in different amounts (5, 10 and 20 wt% with respect to the overall amount of organic phase).

On the other hand, a high molecular weight species, poly(4-hydroxystyrene), PHS, with M_n = 14400 g/mol, has also been tested to take advantage both of its ability of promoting hydrogen bonds and for its attested barrier properties to oxygen [10]. Samples containing various weight fractions of PHS were prepared in combination with PE-PEG or PE-PEG-Si/SiO_2 in order to cover the broadest possible range of formulations. The amount of PHS added to the coating was varied between 0 and 40 wt% in the silica-free PE-PEG coating (samples H00, H00-S20, H00-S40), between 0 and 44 wt% in the hybrid coating containing 33 wt% of silica (samples H33, H33-S22, H33-S44) and between 0 and 11 wt% in the hybrid containing 67 wt% of silica (samples H67, H67-S11).

Analyzing at first the results in terms of overall barrier effect, the *O.T.R.* data, reported in Table 2-7, show that the addition of malic acid has the effect of increasing the oxygen flux with respect to the corresponding formulations not containing malic acid. When 20 wt% of malic acid is added, the *O.T.R.* value of the coated film is similar to that of pure LDPE.

The addition of hydrogen-bond forming low molecular weight products, such as malic acid, was motivated by the idea that such component might promote the formation of a network of hydrogen bonds (with ether bonds within the organic domains and with

silanol groups at the interface) able to enhance the stiffness of the polymer chains. However, the permeation results suggest that such effect is either negligible or, more probably, accompanied by a dramatic increase of the free volume of the final hybrid structure, that leads to a worse barrier performance; for this reason, a higher molecular weight species has been attempted to achieve a remarkable enhancement of the barrier effect.

Table 2-7, Oxygen transfer rate and time-lag values of coated LDPE films at 35°C and 50°C.

Code	35°C		50°C	
	O.T.R. $cm^3(STP)/(cm^2 \cdot d \cdot atm)$	**Time-lag** s	***O.T.R.*** $cm^3(STP)/(cm^2 \cdot d \cdot atm)$	**Time-lag** s
LDPE	0.675	4.7	1.413	1.9
H50-M05	0.455	1.9	1.031	1.1
H50-M10	0.576	4.9	1.179	1.5
H50-M20	0.711	1.0	1.441	2.1
H33-S22	0.194	6.2	0.615	2.6
H67-S11	0.358	6.0	0.737	4.2
H33-S44	0.296	9.4	0.572	1.4
H00	0.316	6.2	0.826	1.3
H00-S20	0.253	5.3	0.843	1.0
H00-S40	0.291	10.3	0.836	2.5
H50-DL	0.205	3.2	0.622	0.9
H67P	0.338	7.8	0.821	3.6
H50P	0.489	6.2	1.002	2.9
H33P	0.708	4.2	1.333	1.8

The results in terms of permeance show that in all cases, the addition of PHS leads to significant improvement of the barrier properties. Indeed, it is interesting to note that the *O.T.R.* is reduced by a factor of 2.1 and 1.7 at 35 and 50°C respectively, when 22 wt% of PHS is contained in the coating (sample H33-S22). It is also interesting to observe that, when the amount of PHS is raised to 44 wt%, the *O.T.R.* value shows no further reduction, but rather it increases, at 35°C, from 0.194 to 0.296 $cm^3(STP)/(cm^2$ d atm), with respect to the hybrid containing a lower amount of PHS (H33-S22). At 50°C, the increase of PHS weight fraction to 44% leads to a further reduction of the *O.T.R.* value (from 0.615 to 0.572 $cm^3(STP)/(cm^2$ d atm) for the H33-S22 sample), but the reduction is quite low. This means that the effect of PHS is not linearly related to its weight fraction: at both 50 and 35°C there is not a monotonous dependence of the *O.T.R.* value on the amount of PHS. The saturation of the hydrogen bonds that

silanol groups can form with PHS, or the separation of PHS in a separate phase (from PE-PEG, in the organic domains) may be suggested as possible explanations of this behavior.

In particular, at 35°C the dependence of the *O.T.R.* value on PHS content shows a minimum at 22% weight fraction, while at 50°C the *O.T.R.* values seem only slightly affected by PHS addition. This seems a further indication that the more significant contribution of PHS derive from its interactions with silanol groups, even though a minor contribution due to the formation of hydrogen bonding with ether groups of PE-PEG cannot be ruled out. The effect of PHS in decreasing the *O.T.R.* of SiO_2-rich coatings (67 wt%, samples H67 and H67-S11), indeed, is still significant (about 15%), although less important with respect to coating with a lower silica content.

The addition of PHS has also a significant effect on the kinetics of diffusion of oxygen, especially at 35°C. In the case of the time-lag values, however, the trend with PHS content is somewhat opposite to the one observed for the *O.T.R.* values.

Another way that was explored to improve the barrier effect of the coating was to replace PE-PEG with a high oxygen-barrier polymer such as PVOH. However, a coating containing only PVOH as organic component has a very poor adhesion to LDPE because of poor chemical affinity, therefore the problem was overcome by applying to LDPE a first coating layer containing PE-PEG and SiO_2, to ensure adhesion, and a second layer consisting of PVOH and SiO_2 (sample H50-DL). The presence of silanol groups on the surface of the first coating layer should provide thermodynamic affinity and reactive groups, able to react with silanol and/or alkoxy silane groups after application of the second layer allowing to obtain PVOH containing coatings with good, or at least acceptable, adhesion to LDPE. The *O.T.R.* results for such sample are quite good both at 35 and 50°C, and their values are comparable to those obtained on the less permeable samples containing PHS (sample H33-S22, H33-S44). By considering that the coating thickness in the sample H50-DL is nearly twice that of the other samples, the results are not as good as expected, and the time lag values are particularly low.

In order to investigate the role of the chemical composition of the surface of the LDPE substrate, three different coating compositions were applied to LDPE films previously submitted to plasma treatments. In this case, the polar groups generated on

the surface of the LDPE substrate should improve either wettability and/or adhesion either by dipole and hydrogen bond interactions and/or by leading to strong covalent bonds if they would be able to react with silanol groups or Si-OR groups of the reactants [30].

It is interesting to compare the results with those obtained by applying coatings with the same composition onto untreated LDPE surfaces. It can be observed that the plasma treatment has a positive effect only on the sample with the highest inorganic content (H67), while for samples richer in organic phase the best performance is observed when they are coated on untreated LDPE surface.

Once again, the permeance values have been treated in order to extrapolate the barrier properties of the different coatings, oxygen permeability values of the ‘‘pure” hybrids have been then evaluated according to Eq. (18) and are reported in Table 2-8.

Table 2-8, Oxygen permeability of pure LDPE and pure coatings at 35°C and 50°C.

Code	**Permeability** Barrer	
	(35°C)	(50°C)
LDPE	4.625	9.683
H50-M05	0.170	0.464
H50-M10	0.529	0.952
H50-M20	-	-
H33-S22	0.041	0.166
H67-S11	0.087	0.176
H33-S44	0.080	0.146
H00	0.451	1.512
H00-S20	0.307	1.590
H00-S40	0.389	1.561
H50-DL	0.083	0.313
H67P	0.074	0.215
H50P	0.221	0.431
H33P	-	-

All coatings containing PHS showed permeability values lower then that in the PE-PEG-Si/SiO_2 hybrids, both at 35 and 50°C. At the lowest temperature, the addition of a small percentage (11 wt%) of PHS to samples containing 67 wt% of SiO_2 (H67) leads to a further decrease in permeability of 1.2 times, the addition of a somewhat higher percentage (22 wt%) of PHS to the sample containing 33% of SiO_2 leads to a

reduction factor of four and a further increase of PHS percentage (44 wt%) leads to a 2 times reduction with respect to the PHS-free sample (H33). The lowest permeability values (100 and 50 times lower than that of LDPE alone, at 35 and 50°C, respectively) were obtained for the coating with intermediate amount of silica and PHS (H33-S22). However, the effect of the addition of PHS on permeability is not monotonous with PHS content, but there exists a minimum, that has to be located at around 20 wt% of PHS. The existence of a critical concentration of PHS above which there is no further reduction of permeability is visible in both the samples containing 33% of silica and the silica-free samples, while in the case of samples rich in silica (H67) the inspected interval of PHS concentration is too narrow to evidence such a behavior.

The existence of a minimum is not surprising and may be due to different issues that occur at high concentrations of PHS such as *i*) the saturation of the hydrogen bonds that silanol groups can form with PHS, and, to a lower extent, with ether groups of PE-PEG: *ii*) poor miscibility between the two organic components, that can induce phase separation of PHS, limiting the formation of hydrogen bonds with silanols, and *iii*) changes in the final morphology.

In order to gain an insight into the permeation mechanism within the system PE-PEG-Si/SiO_2/PHS, it is useful to compare the behavior of the present hybrid system with the one obtainable from a nanocomposite material that could be prepared by dispersion of silica spherical particles in the blend formed by the two polymers.

To describe the permeation behavior of the polymer blend we used a simple mixing rule that neglects the mutual interactions between the two polymers:

$$P_{org} = x_{PHS} P_{PHS} + x_{PE-PEG} P_{PE-PEG} \quad (32)$$

where x_{PHS} and $x_{PE\text{-}PEG}$ are the molar fractions (calculated considering the average molecular weights of the organic species) of the two components in the organic phase and P_{PHS} and $P_{PE\text{-}PEG}$ are the pure polymers permeabilities. The permeability of the organic phase is now entered in the Maxwell model of Eq. (31), obtaining:

$$P_{hybrid} = P_{org} \frac{1-\phi}{1+\phi/2} = \left(x_{PHS} P_{PHS} + x_{PE-PEG} P_{PE-PEG}\right) \frac{1-\phi}{1+\phi/2} \quad (33)$$

In Figure 2-14, the data estimated by Eq. (33) are reported as continuous lines and are compared to the experimental ones and to the value of pure PHS permeability taken from the literature at 35°C [10].

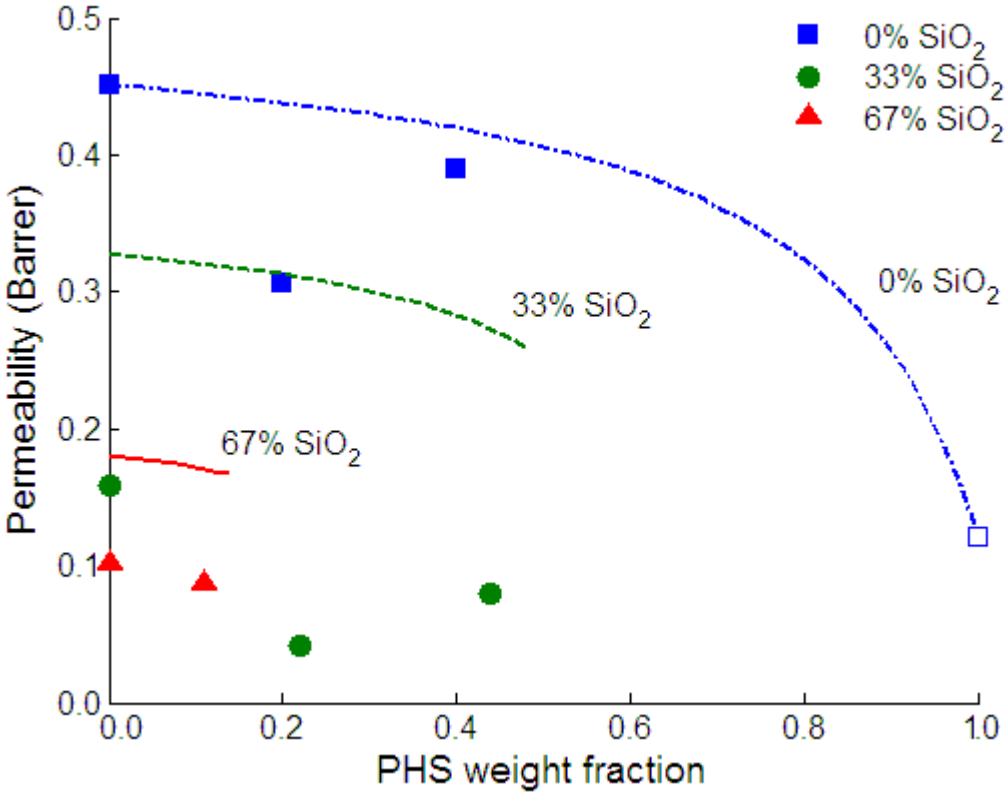

Figure 2-14, Permeability in organic-inorganic hybrid at 35°C (the open symbol is taken from the literature [10]); curves are due to the model in Eq. (33).

Considering at first just the polymer blend by itself, and comparing the experimental data with those calculated by the additive rule expressed by Eq. (32), it should be noticed that, at low PHS content the experimental permeability of the system is lower than that predicted by the additive rule, meaning that a synergic effect takes place between the two polymers, that may be due to the formation of hydrogen bonds between PHS and PE-PEG segments. For higher PHS content, the system seems to follow more closely the additive behavior represented by Eq. (32).

When considering the ternary system, containing also the inorganic component, it can be seen that the hybrid permeability is much lower than that calculated on the basis of Eq. (32), representative of the permeability of a filled system obtained by physically dispersing the same volume fraction of spherical silica, as already observed for the

system with just PE-PEG constituting the organic phase. This result can once again be attributed to the fact that the coating molecular architecture consists of a highly interpenetrated network of organic and inorganic phases rather than of a physical dispersion of spherical silica particles in the organic phase.

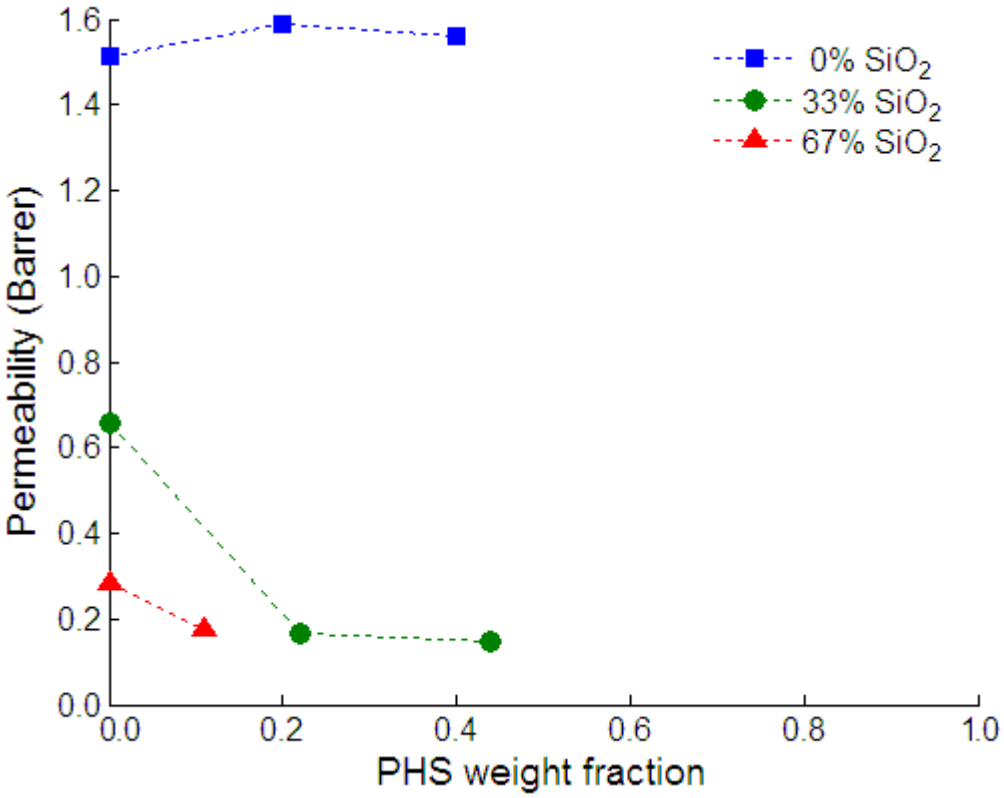

Figure 2-15, Permeability in organic/inorganic hybrid at 50°C.

At 50°C, the behavior is quite different as shown in Figure 2-15: in the silica-free samples, PHS addition seems to have no effect on the permeability: and for sample containing 33% of silica we observe a plateau rather than a minimum for the permeability. Once again, thermal transitions associated with the melting of small crystalline domains in the PE-PEG phase may account for this. In this last case, it was not possible to develop the same calculations carried on the data at 35°C, as no data of permeability of the pure PHS at 50°C are available.

Figure 2-16 summarizes the effect of composition on permeability. As one can see, the optimal conditions are obtained for a sample containing 33 wt% of silica and 22 wt% of PHS.

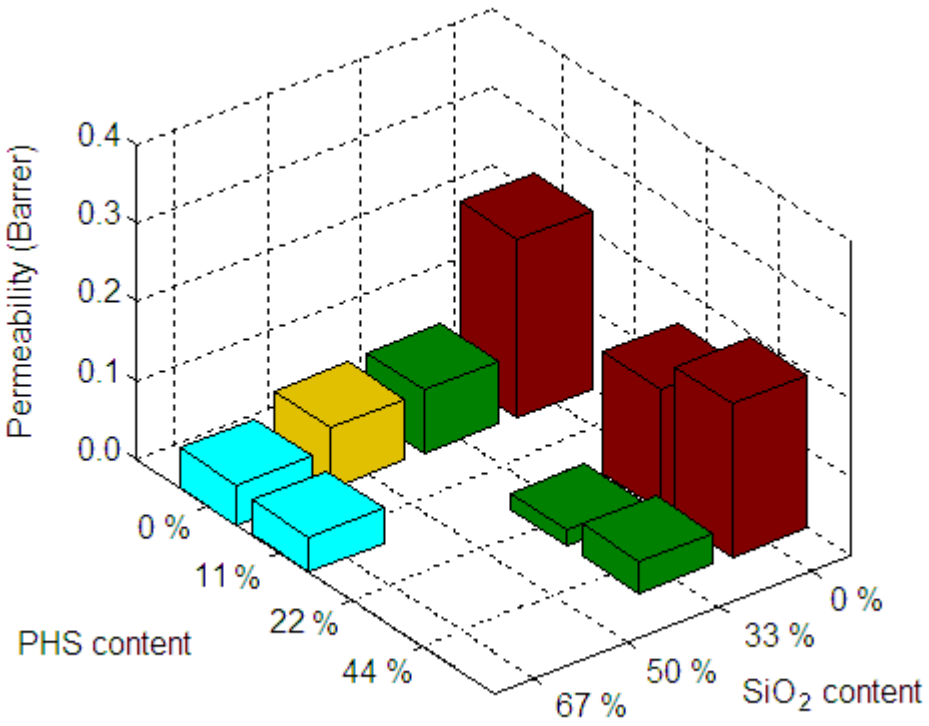

Figure 2-16, Resume of oxygen permeability data in hybrids of set 1 at 35°C.

From these results it is clear that the permeability is significantly dependent on molecular structure and morphology of the coating, which in turn are the results of complex phenomena, mainly involving reactions and phase separations.

2.5.2 PVOH based hybrids

Pure oxygen (0% R.H.) permeation experiments were carried out at 65°C on the various samples of set 2 inspected and listed in Table 2-3. All tests were carried out after a proper evacuation of samples to fully remove moisture and gases absorbed from air for 4-5 days.

At least two experiments were carried out on each sample and the confidence interval was determined considering both the uncertainty on single measurements, as previously explained, and the repeatability of the data. The value reported in the table is the arithmetic mean between the minimum and maximum value obtained.

The hybrid coating with an O/I ratio of 70/30 (Co1) was applied on several different polymeric supports in order to test the effect of the substrate on the properties of the multilayer film. The most interesting samples, i.e. the ones that showed the lowest permeation rates, were selected and characterized more thoroughly: the effect of the O/I ratio on the oxygen permeability and water vapor uptake was tested on samples supported on PET by varying the O/I ratio of the coating from 100/0 (Coating Co0) to 50/50 (Coating Co2). The effect of water ageing on the oxygen permeability values of the coatings was also studied and determined on PET-based laminates. The permeability of O_2, N_2, and CO_2 at 35 and 65°C was determined on a multilayer film of oPP and Co1 coated on one side (oPP1-Co1).

2.5.2.1 Hybrid coatings on different substrates

In Table 2-9 (lines 1-9, 11), the transport properties, in terms of *T.R.* and time-lag, are reported for different polymeric substrates coated by the hybrid coating Co1 (O/I ratio 70/30), at 65°C.

Table 2-9, Oxygen transfer rates and time-lag values in the multilayer samples at 65°C.

		T.R. $cm^3(STP)/(cm^2 \cdot d \cdot atm)$	**Time-lag** s
1	oPP	1.7 ± 6%	3.7 ± 15%
2	oPP-Co1	1.3×10^{-3} ± 6%	1.2×10^{4} ± 1.5%
3	cPP	0.94 ± 7%	10 ± 18%
4	cPP-Co1	1.1×10^{-2} ± 9%	~ 10^2
5	LLDPE	1.0 ± 8%	8.2 ± 5%
6	LLDPE-Co1	1.38×10^{-2} ± 6%	~ 10^3
7	COEX	2.3 ± 7%	2 ± 25%
8	COEX-Co1	8.8×10^{-3} ± 8%	~ 10^2
9	PET	1.8×10^{-2} ± 6%	95 ± 10%
10	PET-Co0	2.0×10^{-4} ± 7%	1.40×10^{4} ± 2%
11	PET-Co1	1.7×10^{-4} ± 13%	2.6×10^{4} ± 5%
12	PET-Co2	6×10^{-4} ± 18%	4.7×10^{4} ± 31%
13	PET-Co0 [a]	- [c]	- [c]
14	PET-Co1[a]	8.3×10^{-4} ± 8%	~ 10^3
15	PET-Co1[b]	7.7×10^{-4} ± 6%	- [d]
16	PET-Co2[b]	2.0×10^{-3} ±8%	~ 10^3

[a] Immersion in liquid water for 3 days and evacuation.
[b] Immersion in saturated water vapor for 4 days and evacuation.
[c] After the treatment the coating was dissolved: the transport properties of this sample can be assumed equal to those of neat PET.
[d] The permeation curve exhibited an anomalous transient behavior.

Lower temperatures were also inspected but, for this specific laminated material, the transport rates were too small to be efficiently detected in reasonable time.

In all cases, the *T.R.* of coated samples is lower than that of the neat substrate, by two to three orders of magnitude, and the time-lag is increased after addition of the coating to a similar extent. A general improvement of the oxygen barrier properties is thus observed, that makes these materials certainly suitable for packaging applications. The size of the variations of the transfer rate and time-lag values depends strongly on the transport properties of the substrate, as it is obvious: for instance, the relative reduction of transfer rate in the case of the most permeable polymer (COEX) is more significant than in the case of the less permeable one (PET). However, in order to compare the absolute performance of the coatings one has to look at the values of the material properties *P*, *D* and *S*, listed in Table 2-10.

Table 2-10, Oxygen permeability and diffusivity in the pure coatings at 65°C

		P Barrer	***D*** cm^2/s	***S*** $cm^3(STP)/(cm^3\ atm)$
1	oPP	7.5 ± 6%	4.1×10^{-7} ± 15%	0.15 ± 21%
2	Co1 on oPP	3.8×10^{-4} ± 16%	1.3×10^{-12} ± 22%	2.2 ± 38%
3	cPP	11 ± 7%	1×10^{-6} ± 18%	9×10^{-2} ± 25%
4	Co1 on cPP	34×10^{-4} ± 19%	~ 10^{-11}	~ 10^{0}
5	LLDPE	17 ± 8%	2.5×10^{-6} ± 5%	5.3×10^{-2} ± 13%
6	Co1 on LLDPE	43×10^{-4} ± 16%	~ 10^{-11}	~ 10^{0}
7	COEX	23 ± 7%	3×10^{-6} ± 25%	6×10^{-2} ± 32%
8	Co1 on COEX	27×10^{-4} ± 18%	~ 10^{-11}	~ 10^{0}
9	PET	0.10 ± 6%	2.3×10^{-8} ± 10%	3.4×10^{-2} ± 16%
10	Co0 on PET	0.6×10^{-4} ± 17%	6.5×10^{-12} ± 22%	7×10^{-2} ± 39%
11	Co1 on PET	0.5×10^{-4} ± 23%	6.3×10^{-13} ± 25%	0.6 ± 48%
12	Co2 on PET	1.9×10^{-4} ± 28%	1.6×10^{-13} ± 51%	9.1 ± 79%
13	Co0 on PET [a]	- [c]	- [c]	- [c]
14	Co1 on PET [a]	2.7×10^{-4} ± 18%	~ 10^{-12}	~ 10^{-1}
15	Co1 on PET [b]	2.5×10^{-4} ± 16%	- [d]	- [d]
16	Co2 on PET [b]	6.7×10^{-4} ± 18%	~ 10^{-11}	~ 10^{-1}

[a] Immersion in liquid water for 3 days and evacuation.
[b] Immersion in saturated water vapor for 4 days and evacuation.
[c] After the treatment the coating was dissolved: the transport properties of this sample can be assumed equal to those of neat PET.
[d] The permeation curve exhibited an anomalous transient behavior that did not allow to interpret it with the time-lag method.

It can be seen that, for coating Co1 applied on cPP, LLDPE and COEX, the permeability is of the order of 10^{-3} Barrer, while for the same coating applied on oPP the permeability is equal to about 10^{-4} Barrer and for those applied on PET the

permeability is one order of magnitude lower (10^{-5} Barrer). For coatings applied on cPP, LLDPE, COEX only the order of magnitude of diffusivity could be assessed, that is equal to 10^{-11} cm^2/s in all cases. The value of oxygen diffusivity in oPP and PET-based coatings could be evaluated more accurately and is equal to 1.3×10^{-12} and 6.3×10^{-13} cm^2/s for coatings applied on oPP and PET, respectively.

From the comparison of these values, one can conclude that the properties of the hybrid coating depend rather markedly on the properties of the substrate film, which is a result that deserves some further discussion. First of all, it can be noticed that coatings deposited onto PET exhibit the lowest oxygen permeability, while those applied onto the poly-olefinic substrates have worse barrier performance. As far as adhesion is concerned, PET is the optimal support for the present coatings, as verified directly through pull-off and scratch experiments. Indeed, PET has several sites that can interact with the organic phase of the coating, while the poly-olefinic substrates are less compatible to PVOH based hybrids [21]. Previous studies show that the coating permeability is affected, to some extent, by the surface treatment of the support before deposition [12]. These results seem to indicate that the stronger the adhesion, the best the barrier effect of the coating: such behavior can partly be attributed to the presence of an interfacial layer whose transport properties depend on the interactions between the support and the coating and that was neglected in the present approach. However, the magnitude of the deviations between the properties of similar coatings on different substrates is so large that other factors might be involved, that need to be further investigated.

In the following, the study of the effect of O/I ratio and other factors on the transport properties of the coating will be performed on the multilayer materials based on the most effective substrates, namely PET and oPP.

2.5.2.1 O/I ratio effect in PET-supported hybrid coatings

The *T.R.* and time-lag values obtained from the experimental tests on the coated PET systems at 65°C, without any previous treatment, are listed in Table 2-9 (lines 9-12). As it can be seen, the permeance (*T.R.*) of PET is reduced by about two orders of magnitude after addition of the coatings Co0, Co1, Co2, having increasing silica contents. From the comparison of these values, one can notice that the permeance

reduction caused by the hybrid coating Co1 is of the same order of magnitude than that obtained with pure PVOH (Co0). It can also be observed that the trend of permeance reduction versus silica content in the coating is not monotonic: such behavior will be discussed more thoroughly in the following paragraphs. The time-lag increases by two orders of magnitude with respect to the PET support after addition of organic and hybrid coatings and it increases with a monotonic trend with increasing silica content.

The permeability varies from 0.6×10^{-4} Barrer, for pure PVOH, to 0.5×10^{-4} Barrer for Co1 and 1.9×10^{-4} Barrer for Co2. Clearly, all these coatings have a permeability which is 3-4 orders of magnitude lower than that of the PET support. The great barrier performance given by the PVOH coating on PET is not surprising, due to the fact that the oxygen fed to the film is completely dry; the obtained permeability value is in good agreement with literature data for pure PVOH [31-32].

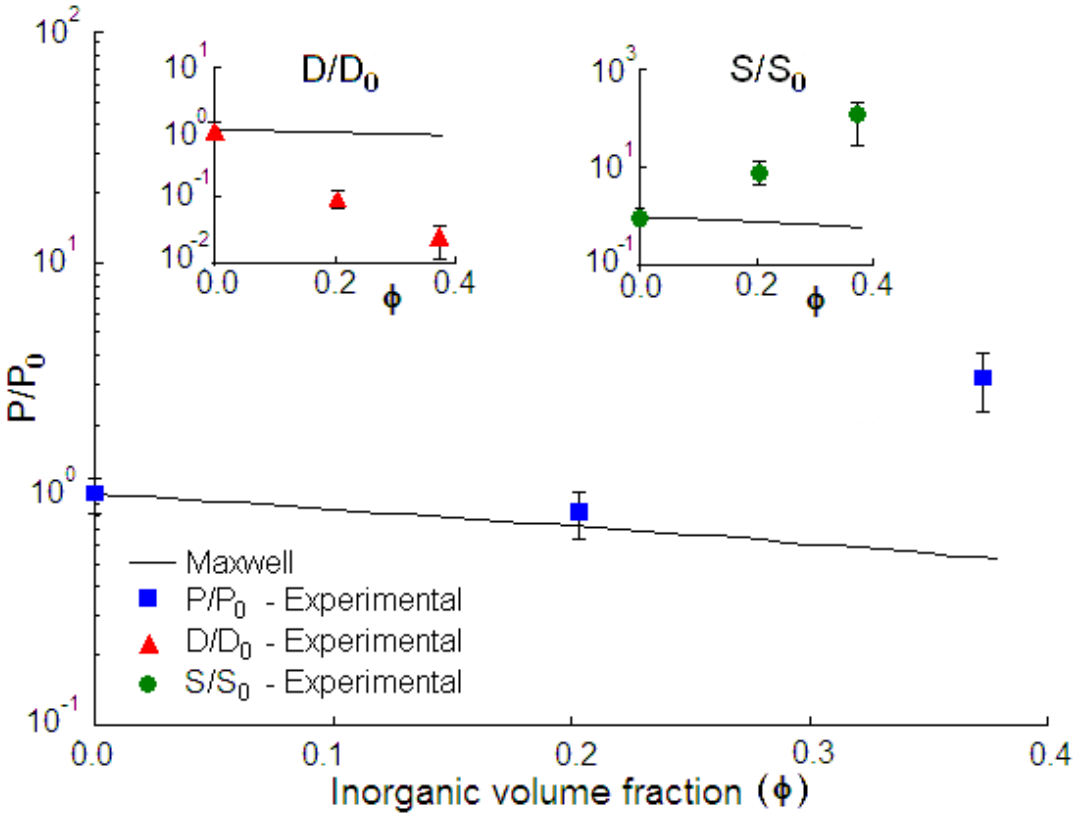

Figure 2-17, Permeability, diffusivity and solubility ratio at 65°C of the coating versus filler fraction and comparison with the Maxwell model.

The values of permeability, diffusivity and solubility variation caused by the addition of silica to pure PVOH are reported in Figure 2-17, expressed as P/P_0, D/D_0 and S/S_0. In the *x*-axis the volume fraction of silica is reported as estimated from the mass fraction by assuming volume additivity.

The transport behavior of the hybrid materials can be interpreted by considering, as reference, the behavior predicted by the Maxwell model for non-interacting composite materials with impermeable, spherical particles, neglecting the interactions between the two components. Several studies indicate that silica domains into hybrid networks such as the one inspected here can be approximately considered nano-spheres [19,33-35].

The diffusivity decreases, as Maxwell model predicts, with decreasing silica content, but the two data points inspected lie much below the predicted trend: such behavior can indicate that there is an interaction between the two phases, and in particular that the diffusivity of the polymeric phase is further reduced by contact with silica. On the other hand, the permeability of coating Co1 lies close to the Maxwell curve, while the behavior of the coating with the higher inorganic content is higher than the predicted behavior. One has to remember that the permeability, in the solution-diffusion framework, is the product of the diffusivity *D* and the solubility coefficient *S*. In the panel in Figure 2-17, it can be seen that the oxygen solubility *S* increases with filler content, which is opposite to what predicted by the Maxwell model according to Eq. (31). This behavior can be attributed to the fact that impermeable silica domains adsorb oxygen onto their surface. After noting this, one may conclude that for the coating with lower inorganic content the permeability behavior is governed by the diffusion process, which is affected by the increased tortuosity induced by silica. For a higher inorganic content, the increase of tortuosity seems to be less significant than other factors that contribute to enhance the solubility and permeability, such as the adsorption of gas by silica.

2.5.2.2 Effect of water ageing on the oxygen transport

It is known that, as in several hydrophilic polymers, the oxygen permeability of PVOH under humid conditions increases with respect to the value measured in a dry environment; but, most significantly, PVOH may dissolve when exposed to liquid

water or high activity water vapor [32,36]. For packaging applications the materials have to be stable and maintain the intrinsic properties also in humid environments. In view of this requirement, oxygen permeability tests were performed on PET based samples before and after immersion in both liquid water and saturated vapor of water at 65°C. In particular, the oxygen permeability was measured on samples previously immersed for 3 days in liquid water (Treatment A) and for 4 days in saturated water vapor (Treatment B) and the results are reported in Tables 2-9 and 2-10 (lines 13-16) in comparison with those relative to the "as-received" films (lines 10-12). The same test was carried on the sample coated with pure PVOH, but after the treatment the coating was practically dissolved and could not be used for permeation tests.

The oxygen permeability of the sample PET-Co1 increases by a factor of 5 after immersion in liquid water; the effect is similar after immersion in water vapor. For coatings with higher inorganic content (Co2) the increase of permeability is equal to 3 after treatment with vapor, which shows that samples with higher inorganic content are less sensitive to water degradation, as shown in Figure 2-18.

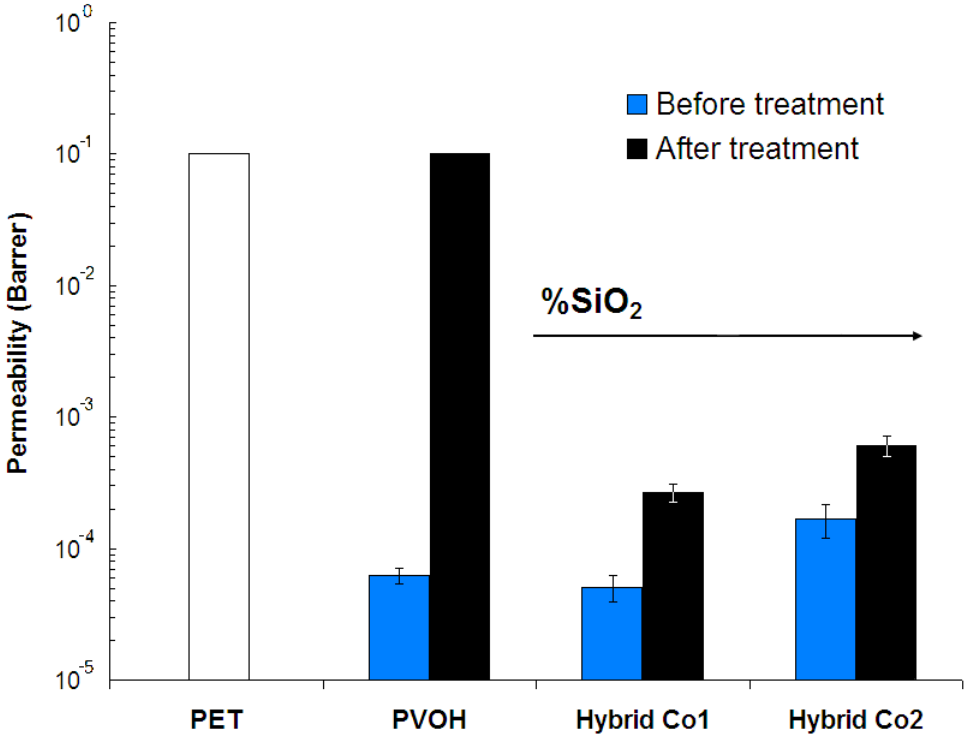

Figure 2-18, Permeability of pure PET and coatings at different O/I ratios at 65°C, before and after water treatment (with liquid water for pure PVOH and hybrid Co1 and water vapor for hybrid Co2).

The behavior observed on the hybrid coatings can be explained by the fact that the hybrid structure allows to depress water-induced plasticization, preventing the dissolution. In order to further investigate this aspect we performed direct moisture sorption experiments on the samples, as explained in the following section.

2.5.2.3 Effect of O/I ratio on the water vapor uptake

Due to the highly hydrophilic behavior of the organic phase of the coating, the samples were tested with respect to water vapor sorption in order to evaluate the properties of the hybrid materials in comparison to pure PVOH. The water vapor solubility isotherms were measured on pure PET samples and on samples coated with layers of PVOH, Co1 and Co2. The results have been manipulated in order to obtain the water uptake in the coating, assuming a mass-additive behavior of water solubility. The results are shown in Figure 2-19 and 2-20, which are relative to the temperature of 35 and 65°C, respectively, and display the grams of water absorbed per total mass of solid phase versus water activity.

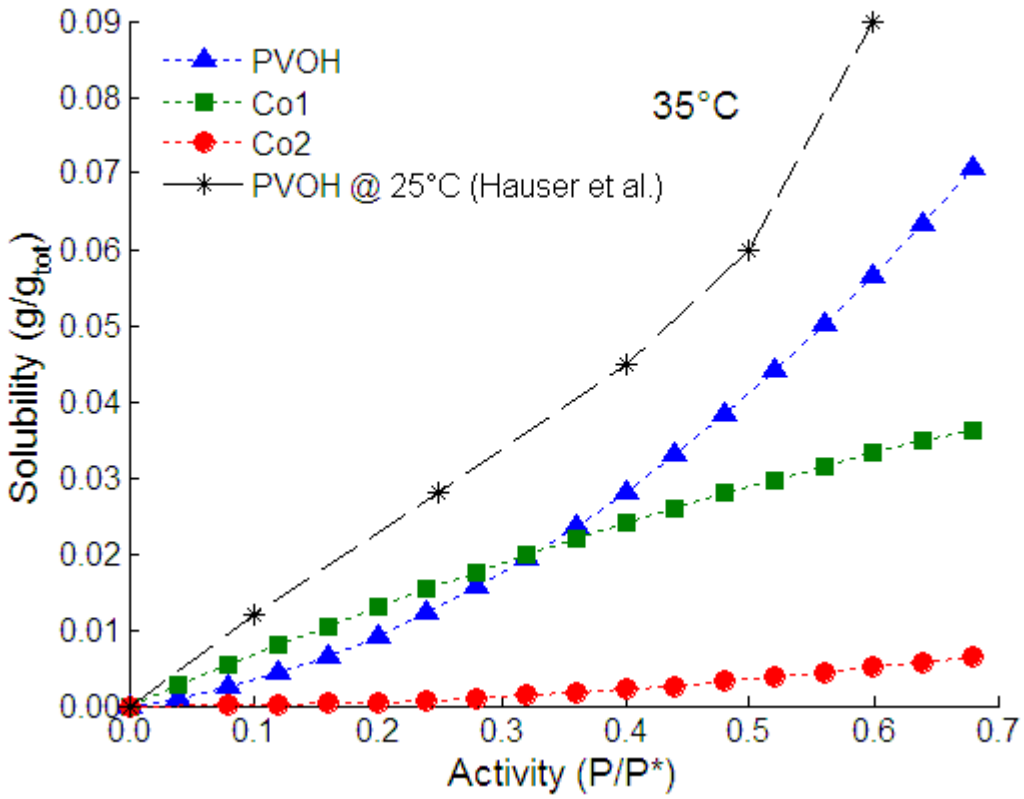

Figure 2-19, Water vapor solubility isotherm of the pure coatings at 35°C in comparison with literature data for pure PVOH at 25°C [36].

For pure PVOH, the water uptake isotherm shows a marked positive concavity, which is in good agreement with literature data [36-38]. The hybrid coating Co1 sorbs more water than pure PVOH at low activity (below 0.35), but at higher activity the water uptake in PVOH becomes higher than that in the hybrid, due to swelling of the polymeric matrix. Interestingly, the concavity of the solubility isotherm of Co1 shows a glassy behavior which indicates the absence of any relevant plasticization phenomenon. The same behavior is observed in the coating with a higher content of silica (Co2), for which the absolute values of water uptake are extremely low and comparable to those of pure PET, not reported in the plot for the sake of clarity. Even neglecting the silica sorption capacity (Maxwell's hypothesis), by referring the water uptake to the mass of PVOH rather than to the total mass, its value is still lower than that measured in the pure PVOH coating. This result indicates that a synergy takes place between the phases of the hybrid material: the water sorption of PVOH is a swelling-enhanced process and silica lowers the ability to swell of the polymeric phase and consequently, its sorption capacity.

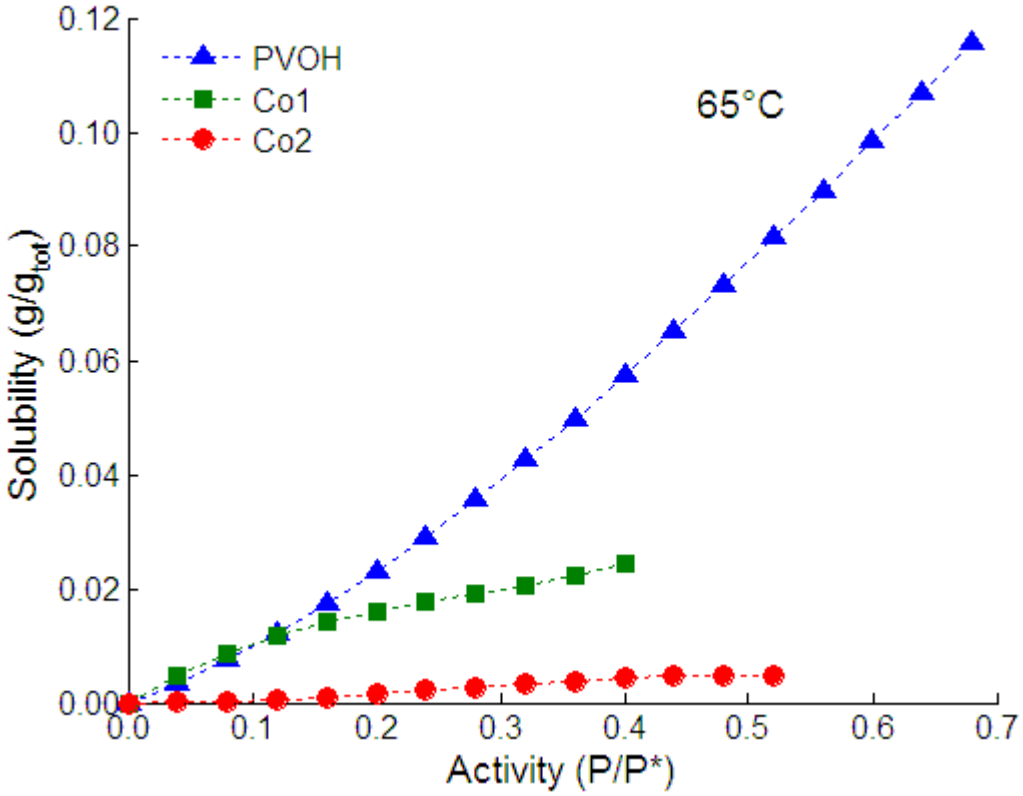

Figure 2-20, Water vapor solubility isotherm of the pure coatings at 65°C.

It has to be noticed that while the oxygen solubility increases with silica content, as discussed before, the water solubility decreases with it. This behavior can be explained by the fact that the processes of water and oxygen sorption differ significantly from one another, because water sorption into PVOH is presumably much higher than that onto silica surface and involves a more significant swelling.

2.5.2.5 Effect of penetrant type and temperature on dry gas transport

In order to investigate the permeability of different gases and different temperatures, a multilayer material with intermediate barrier properties, namely oPP1-Co1, was used, in order to get results in a reasonable amount of time. The sample has an oPP substrate and a single layer of Co1 applied with a roll coating technique (thickness of 1 ± 0.1 μm). The gases inspected were dry nitrogen, carbon dioxide and oxygen, at the temperatures of 35 and 65°C. The gas transport properties are listed in Table 2-9 in terms of gas *T.R.* and time-lag while material properties, such as permeability, diffusivity and gas solubility of the different layers are reported in Table 2-10.

The hybrid material Co1 shows a great barrier toward all gases, as indicated by the extremely low values of permeability; the diffusivity varies between 10^{-13} and 10^{-12} cm^2/s for all penetrants and oxygen shows the highest diffusivity value at both temperatures. The permeability varies over two orders of magnitude (10^{-5}-10^{-3} Barrer) among the various penetrants. In order to explain this fact, a different solubility of the gases in the hybrid coating has to be invoked: for instance, CO_2 is remarkably more soluble in the hybrid matrix than nitrogen. The gas solubility in polymers is known to be correlated with measures of the penetrant condensability such as the critical temperature, T_C [39-40]; also in the case of the polymer (oPP) and of the hybrid material inspected, there is a linear correlation between ln S and T_C, at both the temperatures inspected (Figure 2-21).

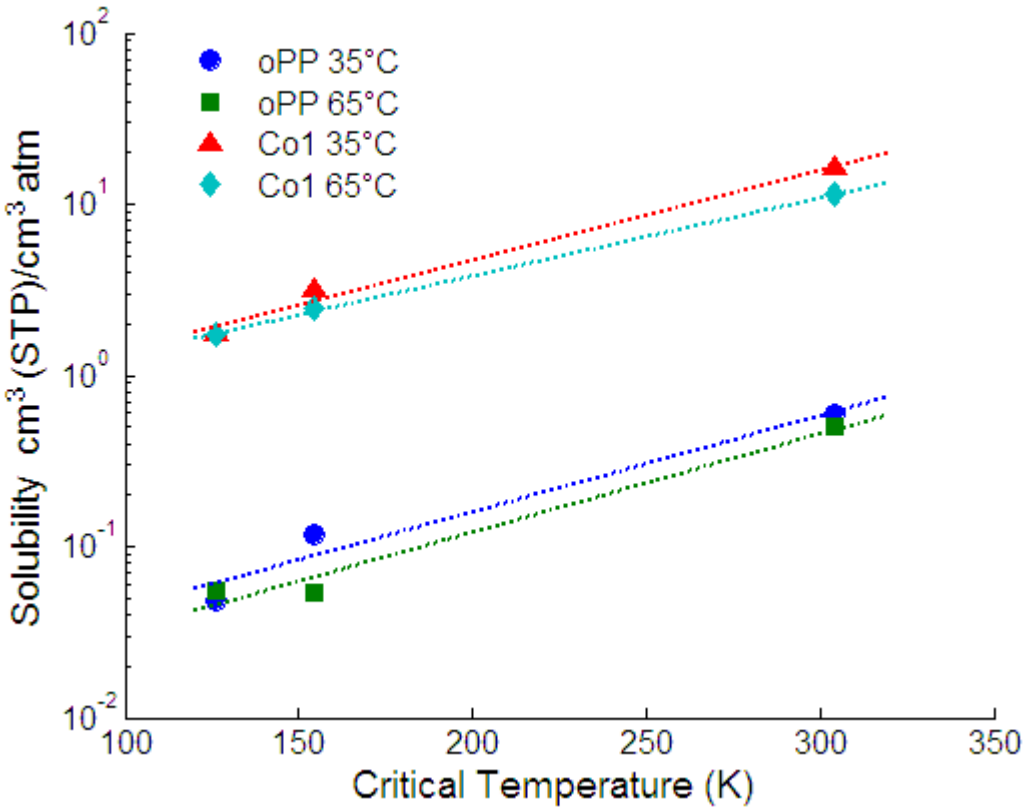

Figure 2-21, Gas solubility in pure oPP and in Co1 hybrids as function of the penetrant critical temperature.

The temperature effect on diffusivity is practically the same for all the penetrants inspected: one can estimate an activation energy value of about 44 kJ/mol for all gases. The activation energy of permeability, on the other hand, varies between 33 kJ/mol, for CO_2, and 44 kJ/mol, for O_2, due to a negligible sorption heat in the case of nitrogen.

2.5.3 Microfibrillated cellulose

Four samples obtained from the two generations (namely G1 and G2) of microfibrillated cellulose with and without glycerol as plasticizer (labeled with letter P), as reported in Table 2-4, have been investigated thoroughly in order to evaluate their transport and barrier properties in different conditions.

First at all, water vapor sorption tests were carried out considering the extreme hydrophilic character of such cellulosic material that is a crucial point for the

investigation of the transport properties. Then pure oxygen permeation experiments were performed on samples completely dry (R.H. = 0) in the permeometer, and at different humidity levels of the membranes (RH. 0-100) by means of the humid permeometer device, which was also employed to carry out water vapor permeation tests. In all cases, temperature was kept constant at the value of 35°C.

2.5.3.1 Water sorption

The differential sorption experiments of water vapor in MFC samples were carried out in the pressure decay apparatus at 35°C exploring a rather wide range of water activities (0-80%); in all cases, the tests were performed at least twice in order to ensure the repeatability of the measurement. This characterization provides the four sorption isotherms at 35°C as well as the diffusivity profiles, as function of the water content in the cellulosic material. The results, in terms of solubility, are reported in Figure 2-22, which compares the different behaviors of the two generations of MFC and the role of the plasticizer.

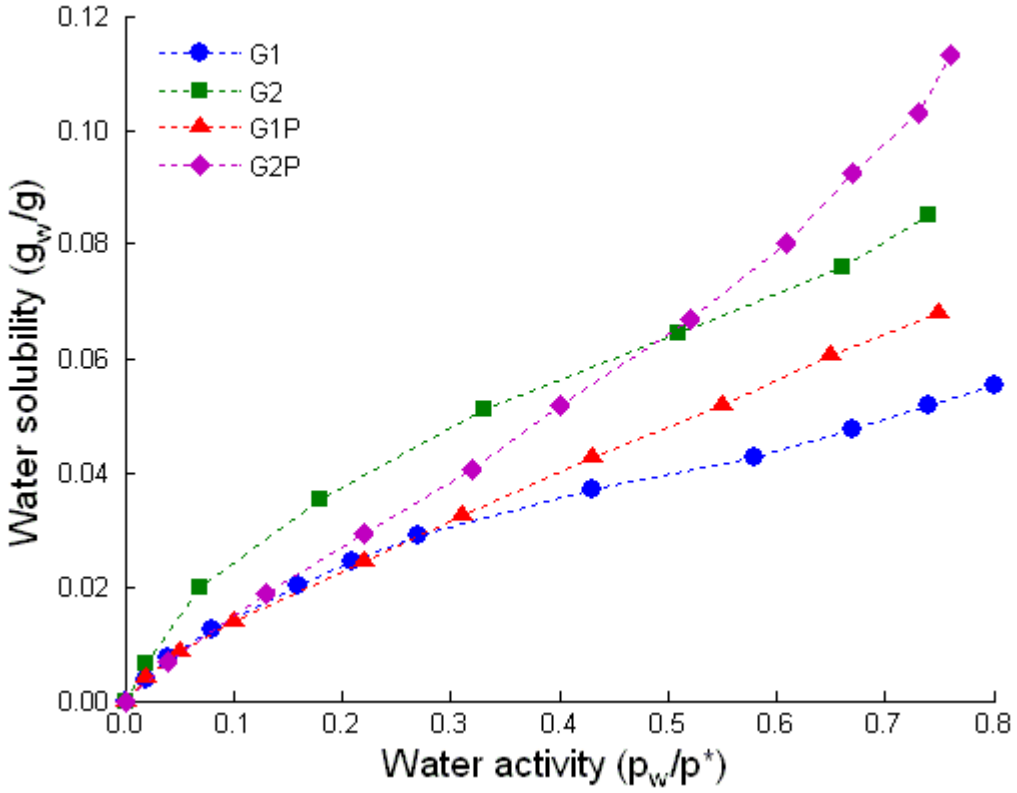

Figure 2-22, Water vapor sorption isotherms in MFC samples at 35°C.

As one can see, all the four materials have similar behavior and the isotherms present the same shape with an initial downward curvature at low activities while the trend tends to change with increasing water content. Indeed, water diffusion in cellulosic system involves a physical adsorption on the fibers surface and a complementary absorption in the amorphous phase: the solubility profile is thus often approached by a BET equation [41]. The obtained values of water uptake at different activities seem to be in good agreement with literature data for cellulosic materials [41-45]. However, it should be noted that at higher activity of the one here investigated, the solubility is expected to present a remarkable increase around 85-90% relative humidity, but these water activities are not achievable with a pressure-decay technique.

Figure 2-22 shows that the MFC of second generation, both with and without plasticizer, present higher water solubility, indicating likely a structural effect due to the different preparation technique. Indeed, even if it has been showed that the fibrils are not significantly shortened during the homogenization [46-47], this second generation presents a straightened structure and it appears more rod-like due to large amount of charged groups created with the treatment. This probably enhances the ability of the fibrils to coordinate water molecules onto the surface and causes the increased water uptake for samples of MFC of second generation in comparison with the first.

Considering the glycerol effect, it can bee seen that, at low activity, the presence of the plasticizer decreases the water solubility: this effect is remarkable in case of G2 and not so evident for G1, while at higher water activity there is an inversion and the glycerol enhances this hydrophilic behavior; the sorption isotherm curves are indeed intersecting at about 20% RH (G1) and 50% (G2). A possible explanation of this feature is that at first the glycerol fills the voids in the cellulosic structure (pure MFC films indeed presents rather high porosity [47]), decreasing the system free volume and causing the reduction of adsorption sites available to water; on the contrary, at high activity, the swelling of the structure, further enhanced by the glycerol, is predominant.

Concerning the kinetics of water sorption, the diffusion coefficient has been determined in every step and the *D* profile as function of the average water concentration is reported in Figure 2-23.

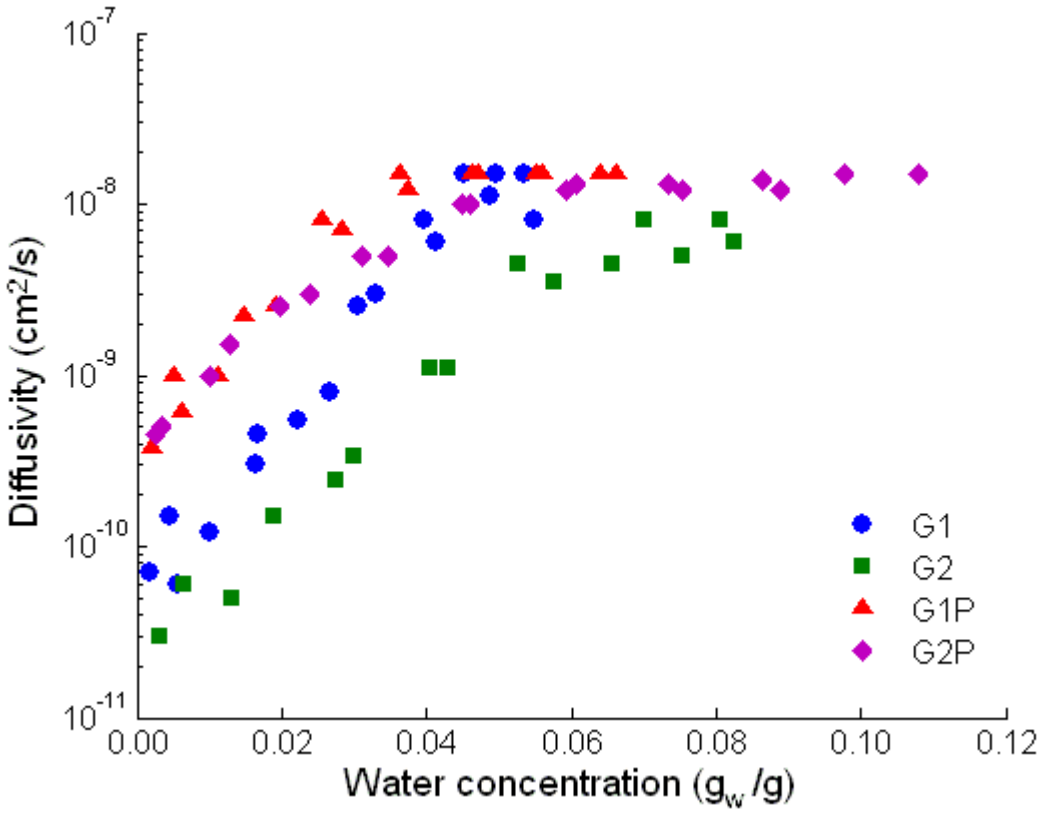

Figure 2-23, Water diffusivity at 35°C in the four different MFC samples.

The plot shows that, when a MFC system is dry, water penetrates the material extremely slowly, the sorption steps seem to be Fickian with a diffusion coefficient in the order of magnitude of 10^{-11} for the pure MFC and 10^{-10} when glycerol is added.

When water is present in the system, D rapidly increases with an exponential trend that can be fitted by the following equation:

$$D(c) = D_0 \exp(\beta \cdot c) \tag{34}$$

The diffusion coefficient increase leads to values up to two orders of magnitude higher than the diffusivity at infinite dilution D_0, but it converge to a constant value D_∞ when a critical concentration c_c, is reached, and it becomes fairly constant and very similar for the different samples. The values of D_0, β and D_∞ obtained from the best fitting of the experimental data are reported in Table 2-11 together with the critical concentration c_c.

It should be noted that, while in case of G1P and G2P there is a clear plateau at high concentration, in samples without plasticizer this is not equally pronounced and the resulting data, D_∞ and c_c, are therefore slightly less accurate.

Table 2-11, D_0, D_∞ and β values for water diffusion in MFC samples at 35°C, on the basis of Eq. (34).

	D_0 (cm^2/s)	β (g/g_w)	Cc (g_w/g)	D_∞ (cm^2/s)
G1	4.55×10^{-11}	124.0	0.045	1.2×10^{-8}
G2	2.27×10^{-11}	92.3	0.062	6.8×10^{-9}
G1P	4.06×10^{-10}	99.0	0.036	1.5×10^{-8}
G2P	4.87×10^{-10}	69.5	0.045	1.3×10^{-8}

As reported in Figure 2-23 and also in Table 2-11, the sample G2 shows the lowest diffusivity, both at low and high activities; the organization of fibrils in the second generation, due to the higher surface charge, seems to enhance the tortuosity for the diffusing path of water, leading therefore to lower diffusivity values. This double effect given by the high value of *S* and small *D*, especially in MFC of second generation, can be related to the formation of a complex structure in the pure MFC samples that allows to accommodate a high number of water molecules but presents kinetic constraints which slow down the sorption process; this seems to be supported by experimental observations of aggregates of microfibrils disposed onto layered structures [47].

The addition of glycerol induces basically the same effect on the two different matrixes: the plasticization enhances the mobility of the cellulose microfibrils and the water can enter the structure faster, the diffusivity shows an increase that can reach even one order of magnitude when this effect is more relevant, i.e. when the sample is dry.

Glycerol, which plasticizes the cellulosic matrix, plays a unique role in the diffusion kinetics increasing the diffusivity in all the investigated range of activity. However, even with the addition of this plasticizer, there seems to be a maximum value of diffusivity which cannot be overcome by the system, as proved by the presence of D_∞ value, which is rather similar for all the materials inspected. This fact suggests the existence of a limit to the system plasticization and swelling probably related to structural constraint. Further analyses are in program to better investigate this system.

2.5.3.2 Water permeation

Differential water vapor permeation experiments were carried out on these cellulosic systems at 35°C in the humid permeometer apparatus. The tests were performed at different water activities, that have been kept fixed at one side of the membrane, while on the other side the amount of permeate was detected by means of increase of pressure. The obtained values of permeability, in Barrer, are reported in Figure 2-24 as function of the average water activity in the films during the step.

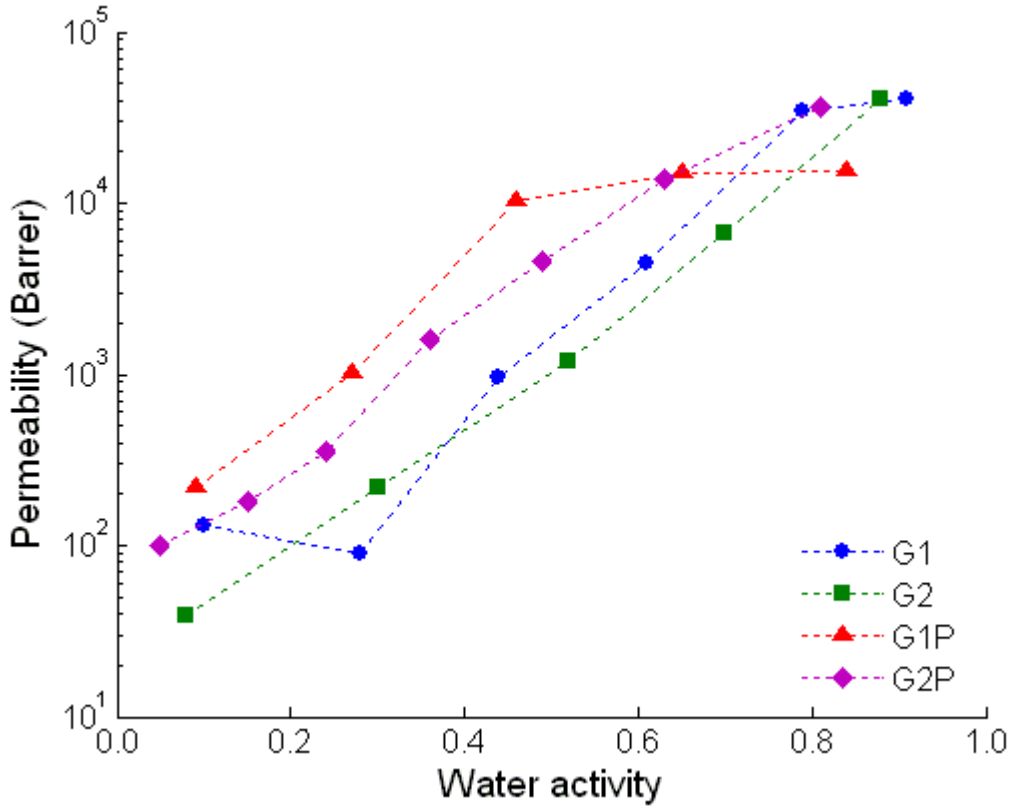

Figure 2-24, Water vapor permeability in MFC films at 35°C.

The figure shows that the two different generations of MFC, with or without the plasticizer, present the same exponential trend with the water activity, *P* gains even 2 or 3 orders of magnitude in the investigated range, due to the extreme hydrophilic behavior of such system.

Water vapor permeation tests reveal that *P* is higher in samples with glycerol (G1P, G2P) in the entire set of activities; the plasticized samples indeed showed faster kinetics and, only for the case of high relative humidity, also a larger solubility. The double effect that the glycerol plays on the solubility is not here observed, and this

indicates that the diffusivity is more significant than the solubility in defining permeation properties. However, in this case, the solution-diffusion mechanism seems to be inappropriate to describe the system, which cannot be assumed as a dense membrane, and other phenomena, such as the physical absorption on the fibril surfaces, are predominant. Hence, *P* cannot be strictly equal to the product *D* times *S* as previously stated for polymeric membranes in Eq. (8) as indicated in Figure 2-25 where the permeability from permeation tests is plotted in comparison with the product *D* times *S*, as determined from sorption experiments.

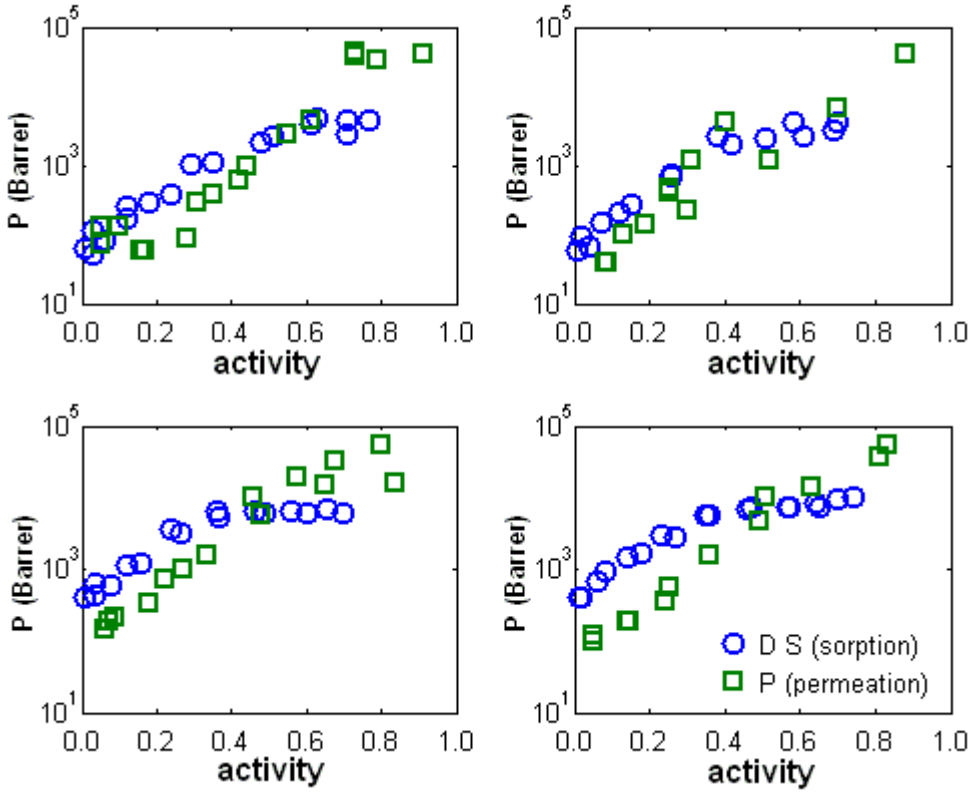

Figure 2-25, Comparison between permeability as obtained from permeation experiments with *P* calculated as *D* times S from sorption tests, for all the four MFC samples at 35°C.

In the charts indeed it can be noticed that the product of diffusivity and solubility shows, as a function of water activity, presents a similar increasing trend with respect to permeability; however, it has also been shown that values, at the same water activity, can differ by more than one order of magnitude, which is well above the experimental error for this kind of systems.

Concerning the water vapor permeability as determined with permeation tests (reported in Figure 2-24), one can see that there exists a sort of inversion at very high activity but the trends are not so clear being *P* rather similar for the four samples when the water activity is high, and close to R.H. = 100% the curves seem to converge almost to the same values.

The same argument should be used to compare the trends of the two different generations of MFC that indicate a higher permeability in the first generation, for the pure cellulose film as well as for the plasticized one. This is in agreement with the fact that *D* plays a dominant role in determining the permeability, because G1, as showed in Figures 2-22 and 2-23, presents higher diffusivity but lower water solubility than G2.

Moreover, these experiments allowed to determine the time-lag of diffusion from the analysis of the permeation curve. Unfortunately, the solution-diffusion mechanism cannot explain the phenomenon here considered and, the so-obtained values of diffusivity are rather inaccurate and therefore they are not here reported.

2.5.3.3 Oxygen permeation

Oxygen permeation tests were carried out on the four samples at 35°C, either in dry or humid conditions and the results by means of the two permeation apparatus.

Permeability values in dry conditions, reported in Table 2-12, show the excellent barrier properties toward oxygen of the MFC films, comparable with those for ultra-barrier application such as EVOH or PVOH [48], commonly used for specific applications. The characterization of barrier properties in specimens in dry conditions led to the calculation also of the oxygen diffusivity with the time-lag method, while it was not possible in the case of humidified samples due to the different technique used.

Table 2-12, Dry oxygen permeability and diffusivity in MFC samples at 35°C (R.H. = 0).

	P (Barrer)	***D*** (cm^2/s)
G1	7.9×10^{-4}	6.32×10^{-11}
G2	18.7×10^{-4}	3.06×10^{-11}
G1P	38.1×10^{-4}	4.18×10^{-11}
G2P	26.9×10^{-4}	1.47×10^{-11}

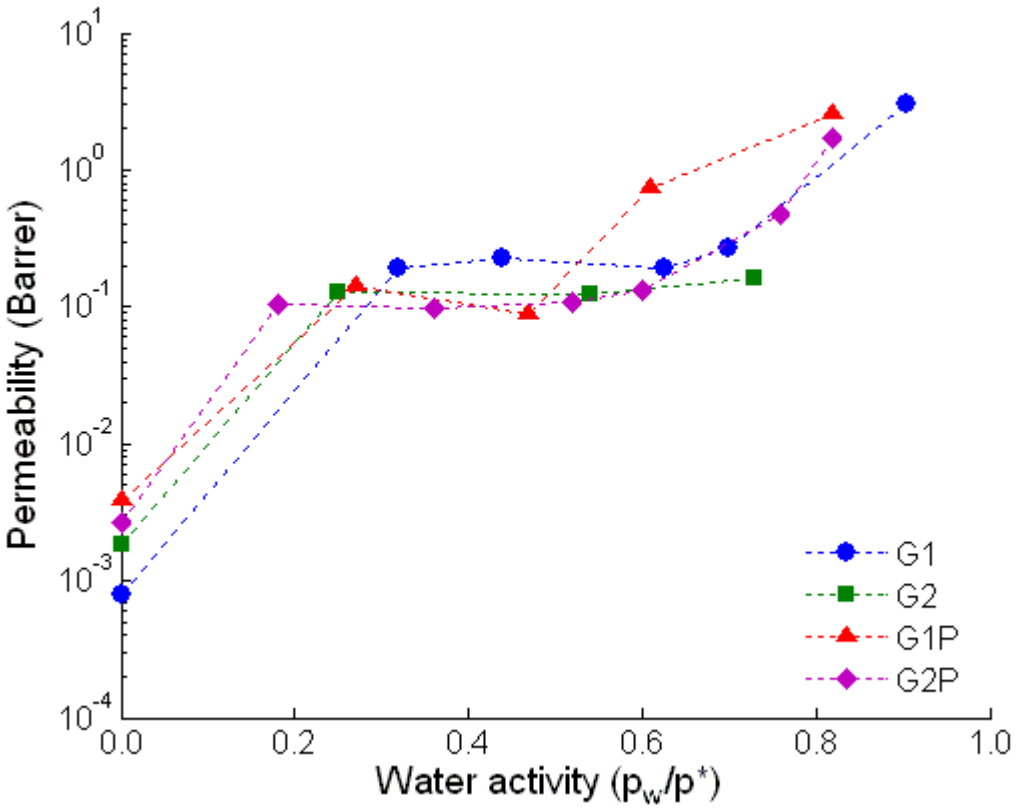

Figure 2-26, Oxygen permeability at 35°C at different relative humidity in the four MFC samples.

Figure 2-26 reports the oxygen permeability in the entire range of water activity explored. As previously observed, the cellulose network, when dry, presents a structure particularly compact and stiff; penetrating molecules encounter thus several physical hindrances which give this remarkable barrier effect; oxygen diffusivities are also rather small and comparable with those observed for water.

As one can see, the first generation of cellulose, with no glycerol, is the sample that can guarantee the strongest barrier effect in terms of permeability, while, concerning the diffusivity, sample G2P is the one with the lowest value.

The addition of plasticizer in the cellulosic matrix plays a double role: while the oxygen permeability results rather increased, the effect on the diffusion coefficient has been reduced by the addition of glycerol.

Figure 2-26 shows that, when the water content in the specimens is raised, there is a sudden jump of the permeability, which increases of about two orders of magnitude. This value seams then to remain stable up to an activity of about 60% before showing a further increase of permeability at the higher R.H. inspected. However, it should be

noted that, while permeability data in dry condition are quite safe, the humid oxygen permeation tests have been performed with a different instrument (the humid permeometer) endowed with a lower sensitivity, and they are not as accurate as the others: up to about 50% of R.H. indeed the estimated *P* is very closed to the sensitivity of the instrument. For this reason, no trend can be surely described in this range for the oxygen permeability at different humidity while *P* certainly increases quite significantly at higher water activities in most of the samples.

On the other hand, it has been often reported for hydrophilic membranes, and more specifically for cellulose [49], that there exists a clear behavior of permeability divided in two regions, a steep increase of *P* increasing the water content from dry conditions, and a sort of plateau when the structure results sufficiently swollen. In some cases it has also been observed a further increase, when the membrane is almost saturated.

Hence, the four trends reported in Figure 2-26, even if probably not too accurate, look rather reasonable for cellulose based materials.

2.6 Conclusions

In this chapter, it has been proved how the sol-gel route is suitable for the preparation of nanocomposite materials with improved barrier properties. This particular technique, indeed, allow to achieve composite materials in which the organic (polymeric) domains are highly interconnected with the silica Si-SiO_2 at the nano-scale, leading therefore to an improvement of the barrier properties. In this concern, two different approaches have been attempted and two different systems were studied. Fist at all, a highly permeable material, such as a polyethylene-based material, is considered as organic phase and it has been showed how the barrier performances were remarkably improved; oxygen diffusivities and permeabilities were indeed considerably lowered, making thus the system interesting for the food packaging applications. The barrier performances of the same system were further improved by the addition of a good barrier material, such as PHS, which is also able to promote

hydrogen bonds. This latter effect, indeed, was found to be the crucial point in the creation of the highly networked structure with interpenetrated organic and inorganic domains that provides the material the desired barrier effect.

A second study was then performed to develop an ultra barrier material for special applications; in this idea, as organic moiety, polyvinyl alcohol was selected, because of its incredible oxygen barrier properties; on the other hand, PVOH is particularly water sensitive and when exposed to water, that is a good solvent for the polymer, it tends to degrade and looses all the properties. Hence, the sol-gel route was used improve the resistance to water while the barrier effect, in this case, was guaranteed by the polymeric phase. In this idea, it has been showed that the great performance in barrier properties observed for the samples as received was basically kept for the nanocomposite systems, in which the inorganic domains stabilized the polymeric chains avoiding the swelling and the consequent dissolution of the polymeric phase.

The third part was about a recently developed fibrous material, microfibrillated cellulose, MFC. Two different generations of cellulose have been characterized in terms of oxygen and water transport properties through MFC films, pure or with glycerol as plasticizer. A remarkable barrier effect has been reported for the case of pure (dry) oxygen that increases, as expected for such hydrophilic materials, with increasing the water content in the membrane. The behavior of MFC films with respect to water was also investigated and the results were discussed on the basis of structural considerations regarding the two different generations, with or without plasticizer. It has been reported that MFC of second generation, present higher water solubility due its straightened rod-like structure, given by the large amount of charged groups created with the treatment; this enhances the ability of the fibrils to adsorb water onto the fibril surface. On the contrary, the higher surface charge seems to enhance the tortuosity for the diffusing path of water that lowers the water diffusivity. This double effect given by the high value of S and small D is probably related to a complex structure of the microfibrils which, supposedly, are arranged as layers.

From the comparison between sorption and permeation data, it has also been shown that water in a MFC system cannot be explained by a solution-diffusion mechanism. There is indeed a physical adsorption of water molecules on the microfibrils surface

that plays a relevant role in determining the water uptake, and the transport properties in general.

The revealed properties proved how MFC has interesting applications, due to its particular properties and its remarkable sustainability and biodegradability, as reinforcement in the field of bio-nanocomposites.

References:

[1] Crank J. The mathematics of diffusion. Oxford Press. London (1956).

[2] Barrie J.A., Levine J.D., Michaels A.S., Wong P. Diffusion and solution of gases in composite rubber membranes. *Trans. Faraday Soc.* **59** (1963) 869-878.

[3] Jaeger J.C. Conduction of heat in a solid in contact with a thin layer of a good conductor. *Quart. J. Appl. Math.* **8** (1955) 101-106.

[4] Toselli M., Marini M., Fabbri P., Messori M., Pilati F. Sol-gel derived hybrid coating for the improvement of scratch resistance of polyethylene. *J. Sol-Gel Sci. Tech.* **43** (2007) 73-83.

[5] Minelli M., De Angelis M.G., Doghieri F., Marini M., Pilati F., Toselli M. Oxygen permeability of novel organic-inorganic coatings: I. Effects of organic-inorganic ratio and molecular weight of the organic component. *Eur. Polym. J.* **44** (2008) 2581-2588.

[6] Peeters M.P.J., Wakelkamp W.J.J., Kentgens A.P.M. A ^{29}Si solid-state magic angle spinning nuclear magnetic resonance study of TEOS based hybrid materials. *J. Non-Cryst. Solids* **189** (1995) 77-89.

[7] Laridjani M., Lafontaine E., Bayle J.P., Judeinstein P. Structural studies of ideal organic-inorganic nanocomposites by high resolution diffractometry and NMR spectroscopy techniques. *J. Mater. Sci.* **34** (1999) 5945-5953.

[8] Geppi M., Mollica G., Borsacchi S., Marini M., Toselli M., Pilati F. Solid State NMR characterization of PE-PEG/Silica hybrid materials prepared by microwave-assisted sol-gel process. *J. Mater. Res.* **22** (2007) 3516-3525.

[9] Tian D., Dubois P.H., Jerome R. A new poly(epsilon-caprolactone) containing hybrid ceramer prepared by the sol-gel process. *Polymer* **37** (1996) 3983-3987.

[10] Puleo A.C., Muruganandam N., Paul D.R. Gas sorption and transport in substituted polystyrenes. *J. Polym. Sci. Part B Polym. Phys.* **27** (1989) 2385-2406.

[11] Lee C.F., Yang C.C., Wang L.Y., Chiu W.Y. Novel amphiphilic carbon black composite nanoparticles from TEMPO-terminated polymer and TEMPO-terminated block copolymer grafted carbon black. *Polymer* **46** (2005) 5514-5523.

[12] Toselli M., Pilati F., Marini M., Doghieri F., De Angelis M.G., Minelli M. Oxygen permeability of novel organic-inorganic coatings: II. Modification of the organic component with a hydrogen-bond forming polymer. *Eur. Polym. J.* **44** (2008) 3256-3263.

[13] Montenero A., Passera M., Rocchetti M. A Laminated material having a high oxygen-barrier effect. PCT Int. Appl. WO 2007042993 (2007).

[14] Hench L.L., West J.K. The sol-gel process. *Chem. Rev.* **90** (1990) 33-72.

[15] Mansur, H.S., Orefice R.L., Mansur A.A.P. Characterization of poly(vinyl alcohol)/poly(ethylene glycol) hydrogels and PVA-derived hybrids by small-angle X-ray scattering and FTIR spectroscopy. *Polymer* **45** (2004) 7193-7202.

[16] Andrade G.I., Barbosa-Stancioli E.F., Piscitelli Mansur A.A., Vasconcelos W.L., Mansur H.S. Small-angle X-ray scattering and FTIR characterization of nanostructured poly (vinyl alcohol)/silicate hybrids for immunoassay applications. *J. Mater. Sci.* **43** (2008) 450-463.

[17] Fonseca dos Reisa E., Campos F.S., Pereira Lage A., Cerqueira Leite R., Heneine L.G., Vasconcelos W.L., Portela Lobato Z.I., Mansur H.S. Synthesis and characterization of poly (vinyl alcohol) hydrogels and hybrids for rMPB70 protein adsorption. *Mat. Res.* **9** (2006) 185-191.

[18] Uragami T., Okazaki K., Matsugi H., Miyata T. Structure and permeation characteristics of an aqueous ethanol solution of organic-inorganic hybrid membranes composed of poly(vinyl alcohol) and tetraethoxysilane. *Macromolecules* **35** (2002) 9156-9163.

[19] Kim D.S., Park H.B., Rhim J.W., Lee Y.M. Preparation and characterization of crosslinked PVA/SiO_2 hybrid membranes containing sulfonic acid groups for direct methanol fuel cell applications. *J. Membr. Sci.* **240** (2004) 37-48.

[20] Xiong Y., Liu Q.L., Zhu A.M., Huang S.M., Zeng Q.H. Performance of organic-inorganic hybrid anion-exchange membranes for alkaline direct methanol fuel cells. *J. Pow. Sour.* **186** (2009) 328-333.

[21] Lee S.Y., Lee J.D, Yang S.M. Preparation of silica-based hybrid materials coated on polypropylene film. *J. Mater. Sci.* **34** (1999) 1233-1241.

[22] Li J.B., Gellerstedt G. Oxymercuration-demercuration kappa number: an accurate estimation of the lignin content in chemical pulps. *Nordic Pulp Paper Res. J.* **17** (2002) 410-414.

[23] Pääkkö M., Ankerfors M., Kosonen H., Nykänen A., Ahola S., Osterberg M., Ruokolainen J., Laine J., Larsson P.T., Ikkala O., Lindström T. Enzymatic hydrolysis combined with mechanical shearing and high-pressure homogenization for nanoscale cellulose fibrils and strong gels. *Biomacromolecules* **8** (2007) 1934-1941.

[24] Wagberg L., Decher G., Norgren M., Lindstrom T., Ankerfors M., Axnas K. The build-up of polyelectrolyte multilayers of microfibrillated cellulose and cationic polyelectrolytes. *Langmuir* **24** (2008) 784-795.

[25] Osman M.A., Mittal V., Morbidelli M., Suter U.W. Epoxy-layered silicate nanocomposites and their gas permeation properties. *Macromolecules* **37 (**2004) 7250-7257.

[26] Choia W.J., Kimb S.H., Kimc Y.J., Kim S.C. Synthesis of chain-extended organifier and properties of polyurethane/clay nanocomposites. *Polymer* **45** (2004) 6045-6057.

[27] Picard E., Vermogen A., Gérard J.F., Espuche E. Barrier properties of nylon 6-montmorillonite nanocomposite membranes prepared by melt blending: influence of the clay content and dispersion state. *J. Membr. Sci.* **292** (2007) 133-144.

[28] Maxwell C. Treatise on electricity and magnetism. Clarendon. Oxford (1904).

[29] Brinker C.J. Hydrolysis and condensation of silicates: effects on structure. *J. Non-Cryst. Solids* **100** (1988) 31-50.

[30] Mazzocchetti L., Scandola M., Amerio E., Malucelli G., Marano C. Preparation and characterization of hybrid nanocomposites coated on LDPE. *Macromol. Chem. Phys.* **207** (2006) 2103-2111.

[31] Brandrup J., Immergut E.H., Grulke E.A. Polymer handbook, 4th ed. John Wiley & Sons. New York (1999).

[32] Finch C.A. Poly vinyl alcohol. Wiley. New York (1992).

[33] Suzuki F., Nakane K., Piao J.S. Formation of a compatible composite of silica/poly(vinyl alcohol) through the sol-gel process and a calcinated product of the composite. *J. Mater. Sci.* **31** (1996) 1335-1340.

[34] Huang H.H., Wilkes G.L. Structure-property behavior of new hybrid materials incorporating oligomeric poly(tetramethylene oxyde) with inorganic silicates by a sol-gel process. 3. Effect of oligomeric molecular weight. *Polym. Bull.* **18** (1987) 455-462.

[35] Tian D., Blacher S., Dubois P.H., Jerome R. Biodegradable and biocompatible inorganic-organic hybrid materials: 2. Dynamic mechanical properties, structure and morphology. *Polymer* **39** (1998) 855-864.

[36] Hauser P.M., McLaren A.D. Permeation through and sorption of water vapor by high polymers. *Ind. Eng. Chem.* **4** (1948) 112-117.

[37] Shafee E.E., Naguib H.F. Water sorption in cross-linked poly(vinyl alcohol) networks. *Polymer* **44** (2003) 1647-1653.

[38] Lien L., Fellows C.M., Copeland L., Hawkett B.S., Gilbert R.G. Water-binding and oxygen permeability in poly(vinyl alcohol) films. *Austr. J. Chem.* **55** (2002) 507-512.

[39] van Amerongen G.J. Influence of structure of elastomers on their permeability to gases. *J. Polym. Sci.* **5** (1950) 307-332.

[40] Barrer R.M., Skirrow G.J. Transport and equilibrium phenomena in gas-elastomer systems. II. Equilibrium phenomena. *J. Polym. Sci.* **3** (1948) 564-575.

[41] Brunauer S., Emmet P.H., Teller E. Adsorption of gases in multimolecular layers. *J. Am. Chem. Soc.* **60** (1938) 309-319.

[42] Joly C., Gauthier R., Escoubes M. Partial masking of cellulosic fiber hydrophilicity for composite applications. Water sorption by chemically modified fibers. *J. App. Pol. Sci.* **61** (1996) 57-69.

[43] Topgaard D., Söderman O. Diffusion of water absorbed in cellulose fibers studied with ^{1}H-NMR. *Langmuir* **17** (2001) 2694-2702.

[44] Kocherbitov V., Ulvenlund S., Kober M., Jarring K., Arnebrant T. Hydration of microcrystalline cellulose and milled cellulose studied by sorption calorimetry *J. Phys. Chem. B* **112** (2008) 3728-3734.

[45] Kohler R., Dück R., Ausperger B., Alex R. A numeric model for the kinetics of water vapor sorption on cellulosic reinforcement fibers. *Comp. Int.***10** (2003) 255-276.

[46] López-Rubio A., Lagaron J.M., Ankerfors M., Lindström T., Nordqvist D., Mattozzi A., Hedenqvist M.S. Enhanced film forming and film properties of amylopectin using micro-fibrillated cellulose. *Carb. Polym.* **68** (2007) 718-727.

[47] Svagan A.J., Hedenqvist M.S., Berglund L. Reduced water vapour sorption in cellulose nanocomposites with starch matrix. *Comp. Sci. Tech.* **69** (2009) 500-506.

[48] Lagaron J.M., Català R., Gavara R. Structural characteristics defining high barrier properties in polymeric materials. *Mat. Sci. Tech.* **20** (2004) 1-7.

[49] Wu J., Yuan Q. Gas permeability of a novel cellulose membrane *J. Membr. Sci.* **204** (2002) 185-194.

CHAPTER III

Modeling transport properties in nanocomposite media

The barrier effect towards small penetrating molecules in heterogeneous systems, such as polymer-layered silicate nanocomposite, has been simulated from a continuum-scale point of view. A finite volume technique was employed to investigate the effect of such inorganic filler loading the organic phase to evaluate the improvement in barrier properties and to relate this with the structural parameters of the filler.

3.1 Modeling details

3.1.1 Diffusion in 2-D ordered structures:

The hindered diffusion in a heterogeneous system has been approached at first in the approximation of a 2-D based geometry that makes the problem solvable from an analytic point of view. This simplified approach also allows to save machine time when this phenomenon is simulated with a computational approach, and allows to test its reliability through the comparison of numerical results with the analytical solution.
The structure of regularly spaced flake filled system is illustrated in Figure 3-1 in the approximation of 2-D geometry. Layers of impermeable flakes are inserted in the structure, normally to the imposed macroscopic concentration gradient, which lies on ζ axis in Figure 3-1.

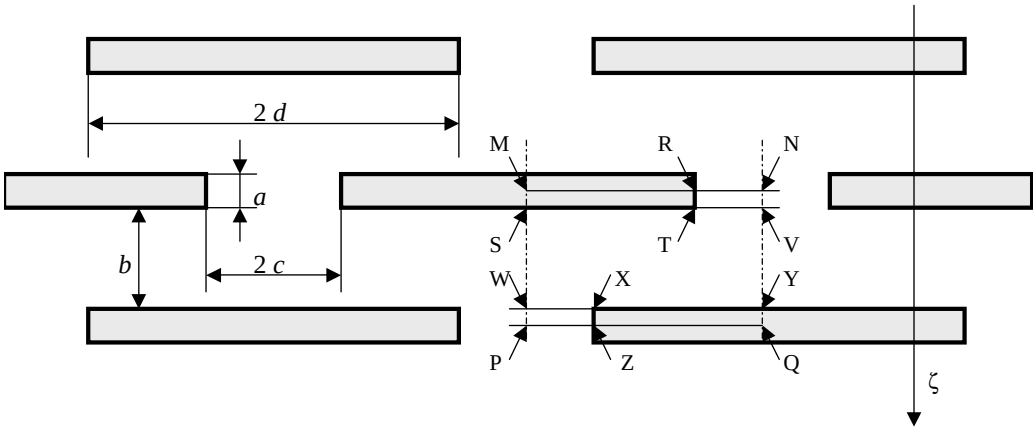

Figure 3-1, Scheme for structure of 2-D nanocomposite system.

Flakes semi-length and thickness are here accounted as *d* and *a* respectively, while *b* indicates the distance between flakes layers and *c* quotes half the distance between successive flakes on the same layer. In dimensionless terms, the structure can be represented by parameters "flake aspect ratio" α, "slit shape" σ and "loading" ϕ, defined as:

$$\alpha = \frac{d}{a} \tag{1}$$

$$\sigma = \frac{c}{a} \tag{2}$$

$$\phi = \frac{ad}{(b+a)(d+c)} \tag{3}$$

The first two parameters are the characteristic area of impermeable and the permeable section respectively on the flake layers, while the latter represents the volume fraction of flakes in the system.

In the geometry pictured in Figure 3-1, a repeating unit can be easily found as that represented by rectangle of vertexes M, N, P e Q, between symmetry lines MP and NQ, upstream line MN (in which inlet section RN is located) and downstream line PQ (in which outlet section PZ is located). The problem of pure diffusion of a penetrant across the flake filled membrane in Figure 3-1 can thus be studied modeling the process in the domain of boundary R-N-Y-X-Z-P-S-T-R, with assigned concentration on inlet section RN and on outlet section PZ, zero-flux condition across boundaries S-T-R, Y-X-Z and symmetry conditions on boundaries NY and SP.

3.1.1.1 An approximate expression from a rigorous approach

Both for the case of pure matrix and for that of flake-filled structure, the resistance to mass transport in MNPQ region of Figure 3-1 can be seen as the sum of the resistance in "hole" regions RNTV and WXPZ, whose properties will be labeled by subscript "H", and in "tortuous path" region SVWY, for which subscript "T" will be used. The ratio between overall resistance in flake-filled systems and in pure matrix can be expressed as in the following relation:

$$\frac{D_0}{D_{ff}} = \left(\frac{D_0}{D_{ff}}\right)_H \Psi_H + \left(\frac{D_0}{D_{ff}}\right)_T \Psi_T \tag{4}$$

where the ratio between resistances in flake-filled and pure matrix in homologous regions is indicated as the ratio between corresponding reciprocate "effective" diffusivities. In this respect, it should be noted that subscript "0" has been used for true diffusion coefficient in pure matrix, while "*ff*" is subscript used for effective diffusivity in flake-filled systems. In Eq. (1), ψ_H a ψ_T indicate weight of resistance to mass transport for "H" and "T" regions, respectively, in the pure matrix. Latter terms are easily derived from the pertinent area of the domain:

$$\Psi_H = 1 - \Psi_T = \phi \frac{\alpha + \sigma}{\alpha} \tag{5}$$

As far as ratio between resistances in "H" regions for the flake filled system and the corresponding pure matrix is concerned, this can be easily derived as the reciprocal of ratio between corresponding "width" of domains actually available to the diffusion of penetrant molecules. The result is indicated in the following equation:

$$\left(\frac{D_0}{D_{ff}}\right)_H = \frac{\alpha + \sigma}{\alpha} \tag{6}$$

The ratio between resistance in "T" region for flake filled system and pure matrix was considered by Aris [1], who derived a set of equations for the determination of its value in the general case. He also proposed an approximate expression for the mentioned ratio which, in terms used by Aris, is written as follows:

$$\left(\frac{D_0}{D_{ff}}\right)_T = \frac{1}{\chi}$$

$$\chi = \frac{r^2}{1-\frac{4r}{\pi}\ln\left(\frac{\pi}{2r}\right)+\frac{4r}{\pi}\ln\left(\frac{1}{\alpha'}\right)} \qquad (7)$$

$$r = \frac{b}{c+d} = \frac{\alpha-\phi(\alpha+\sigma)}{(\alpha+\sigma)^2\phi}$$

$$\alpha' = \frac{c}{c+d} = \frac{\sigma}{\sigma+\alpha}$$

The above expression provides reliable results for $(D_0/D_{ff})_T$ for low values of r and α'. In terms considered in this work, it could be stated that reliable predictions for $(D_0/D_{ff})_T$ are obtained through Eqs. (7) for $(\alpha\phi) > 1$ and $(\alpha/\sigma) > 2$. In this case, the following expression can thus be used to our purposes:

$$\left(\frac{D_0}{D_{ff}}\right)_T = \left[\frac{(\alpha+\sigma)^2\phi}{\phi\sigma-(1-\phi)\alpha}\right]^2 + \frac{4}{\pi}\left[\frac{(\alpha+\sigma)^2\phi}{\alpha-\phi(\sigma+\alpha)\alpha}\right]\ln\left[\frac{\alpha-\phi(\alpha+\sigma)}{\phi\sigma(\alpha+\phi)(\pi/2)}\right] \qquad (8)$$

Furthermore, while equation for χ in set of Eqs. (7) is correctly derived from the work of Aris (cfr. Eq. (21) and following rows in ref.[1]), in the same paper the final expression for χ is reported erroneously, in view of a mistake in the sign of the second term of the denominator. The relevance of this note is in the fact that several authors later used the final result from Aris in different ways and several models are today considered in the discussion of permeation results which ultimately rely on an erroneous expression for the term which refer to the tortuous path.

When results in Eqs. (4), (5), (6) and (8) are taken into account, the final expression for the ratio of overall resistance to mass transport in flake-filled systems and corresponding pure matrix is derived:

$$\frac{D_0}{D_{ff}} = \frac{\alpha\phi}{\sigma}\left(1+\frac{\sigma}{\alpha}\right)^2 + \frac{(\alpha\phi)^2(1+\sigma/\alpha)^4}{1-\phi(1+\sigma/\alpha)} + \frac{\alpha\phi}{\pi/4}\left(1+\frac{\sigma}{\alpha}\right)^2\ln\left[\frac{1-\phi(1+\sigma/\alpha)}{\phi\sigma(1+\sigma/\alpha)(\pi/2)}\right] \qquad (9)$$

The first term on r.h.s. of Eq. (9) ultimately results from the “hole region” contribution to the mass transport resistance and the remaining sum refers to the tortuous path for the diffusing molecule. The form of the first term resembles the simpler expression $(\alpha\phi/\sigma)$ used by other authors in the limit of $\sigma << \alpha$. It is useful

here to clarify that the latter result for the "hole term" resistance can only be derived when slit shape parameter is defined as stated in Eq. (2) [2], differently from what considered by other authors [3-6].

3.1.2 Previous models

3.1.2.1 Diffusion in ordered structures

Several empirical models have been proposed to predict the enhancement in barrier properties of 2-D structures obtained from the ordered inclusion of impermeable platelets. These works consider different contributions to transport, usually related to the "hole" or "tortuous path" resistance in the system, described in a simplified way. Expressions for the empirical models of largest use are reported in this section without attempting an analysis of assumptions and derivations in single models, for which the reader is referred to the original papers.

A simple model was first proposed by Cussler et al. [2], that correctly expresses the first order dependence of barrier enhancement on loading in those systems in which "hole" resistance dominates ($\sigma(1-\phi) << (\alpha\phi)$) and second order character of the same dependence in those systems in which "tortuous path" resistance is ruling:

$$\frac{D_0}{D_{ff}} = 1 + \frac{\alpha\phi}{\sigma} + \frac{(\alpha\phi)^2}{1-\phi} \tag{10}$$

Possible refinements of the same model were later proposed by Falla et al. [3], alternatively accounting for the results reported in the work by Aris [1]:

$$\frac{D_0}{D_{ff}} = 1 + \frac{\alpha\phi}{\sigma} + \frac{(\alpha\phi)^2}{1-\phi} + \frac{\alpha\phi}{(\pi/4)(1-\phi)} \ln\left[\frac{\pi\alpha^2\phi}{\sigma(1-\phi)}\right] \tag{11}$$

or those indicated by Wakeham and Mason [6]:

$$\frac{D_0}{D_{ff}} = 1 + \frac{\alpha\phi}{\sigma} + \frac{(\alpha\phi)^2}{1-\phi} + 2(1-\phi)\ln\left[\frac{(1-\phi)}{2\sigma\phi}\right] \tag{12}$$

The expressions in Eqs. (11) and (12) are here written with reference to slit shape σ defined as in the original work by Cussler [2], and ignoring the definition given in some of the following papers, which is indeed inconsistent with the first one and, more relevant, with the expression for "hole" resistance used. It is also important to

compare last two terms on the r.h.s. of Eq. (11) with “tortuous path” resistance in Eq. (8). The last terms in the two expressions cannot be reduced in equivalent terms, not even for the case of $\sigma << \alpha$, and this is ultimately due to the fact that Eq. (11) was derived starting from the expression in the work by Aris which is affected by the mentioned mistake in sign.

Eqs. (11) and (12) have been largely used for the comparison of predicted barrier enhancement with either experimental or simulation results. On the other hand, discrepancies in results from simulation efforts by different authors, did not allow to validate the above models in ultimate terms. Results in next sections offer a valid contribution to this specific theme.

3.1.2.2 Diffusion in random structures

The earlier theories of diffusion in a nanocomposite media were developed by Barrer [8], and few years later modified by Nielsen [9], in the idea of a highly simplified geometry and based on empirical considerations were able to capture the enhancement in barrier properties by means of just two parameters. The final relationship for diffusivity decrease, that in spite of the simplicity is still widely used, can be written as:

$$\frac{D_0}{D_{ff}} = 1 + \frac{\alpha\phi}{1-\phi} \tag{13}$$

An important contribution to the problem was then given by Cusser, who adapted his previous treatment for ordered structures in Eq. (10) to random systems [3], considering that the resistance is mainly due to the so-called wiggling, that accounts for both the increased distance for diffusion along the main dimension of the lamella and the reduced cross-sectional area between the flakes; hence, in the derivation of his equation all the other contributions were neglected and a sort of adjustable parameter depending on the flake geometrical characteristics, μ, was also introduced to give the following expression [10]:

$$\frac{D_0}{D_{ff}} = 1 + \mu\frac{(\alpha\phi)^2}{1-\phi} \tag{14}$$

Other works are directly focused on composite material characterized by randomly distributed platelets, as those of Fredrickson et al. [11], who examined the disorder and the effect of poly-dispersity considering dilute and semi-dilute regime in a 3-D configuration and solved the problem numerically with a finite element approach. Their work led to the following formula:

$$\frac{D_{ff}}{D_0} = \frac{1}{4}\left(\frac{1}{1+a_1\kappa\alpha\phi} + \frac{1}{1+a_2\kappa\alpha\phi}\right)^2 \tag{15}$$

where: $a_1 = \left(2-\sqrt{2}\right)/4$ and $a_2 = \left(2+\sqrt{2}\right)/4$ and $\kappa = \pi / \ln\alpha$.

The issue of the poly-dispersity of the flake dimensions has also been accounted in the work performed by Lape at al. [12], who developed a model to consider the effect of the distribution in the resulting barrier effect considering a typical Gaussian distribution. The same model is also suitable to mono-dispersed random distributions of flakes in a composite media and the relative diffusivity becomes:

$$\frac{D_0}{D_{ff}} = \frac{\left(1+\frac{2}{3}\alpha\phi\right)^2}{1-\phi} \tag{16}$$

Other interesting works were carried out by Bharadwaj et al. [13] and by Lusti et al. [14] in the idea of investigate the effect of the platelets misalignment, leading to useful considerations and relationships that, for sake of brevity however, are not here reported.

The models here described found applications in predicting the barrier properties of either 2-D or 3-D flake filled systems; in this concern, a particular care has to be applied in the definition of the aspect ratio α, that can be done in different ways, as it will be described more in detail in the following paragraphs. It should be noted that the largest part of the technical literature is focused on the 2-D approximation and the results were then extended in three dimensions considering the aspect ratio simply as the ratio width of the platelets to its thickness. However, in the present work a more accurate definition of the parameters α and σ has been proposed and discussed.

3.2 Previous numerical calculations

Several efforts have been carried out in the past to numerically evaluate the enhancement in barrier properties produced by ordered dispersion of impermeable flakes in a matrix which can be described in terms illustrated above. Calculations reported by Chen and Papathanasiou [4] were performed through a micromechanics-based direct numerical approach in 2-D membranes containing aligned flakes, using the fast multipole-accelerated boundary element method. It is a different numerical solution of the same continuous mechanics problem here considered for the discussion of the permeation process.

Simulations results reported by Falla et al. [3], as well as those by Swannack et al. [6], instead, refer to a Monte Carlo approach to the description of same hindered diffusion problem developed by Eitzman [16] and later modified by these authors. In this case, the simulation generates a composite medium in a unit volume, and a Monte Carlo algorithm gives the molecular trajectories, which are interpreted via a mean square displacement technique based on Browian motion [3].

Sridhar et al. [17] considered a computationally strategy, based on a resistance-in-series and resistance-in-parallel approach, to evaluate the transport properties in 2-D heterogeneous systems with aligned flakes

Goodyer et al. [18-19] developed a three-dimensional finite element code, which can handle the complex geometries to numerically simulate diffusion through a membrane from regularly spaced sources distributed on the membrane surface. The focus of this work was in reproducing experimental results obtained by Liu and Cussler [20] in order to investigate the different contributions to the resistance to the diffusion, even if their results have a general validity.

Gusev et al. [21-22] also developed a finite element algorithm in order to capture the barrier enhancement in 3-D periodic composite system where impermeable round platelets are randomly dispersed in an isotropic matrix. Particular care was devoted to create an unstructured morphology-adaptive mesh to solve the Fick’s law in the computation domain. The best fitting of the results which spanned over a wide range

of system configurations, was given by an exponential behavior for the relative diffusivity D_{ff}/D_0 with the factor $\alpha\phi$.

A similar work has been performed by Nagy et al. [23] who used a resistor representation to calculate the effect of tortuous diffusion paths on the overall diffusivity of three-dimensional flake filled systems. The results then highlighted that the enhancement in barrier properties is the sum of two different contributions, linear and quadratic with $\alpha\phi$, as previously stated by several theoretical models.

3.3 Numerical solution

The pure steady state diffusion process of a single penetrant species in the two-phase medium reported in Figure 3-1, governed by the Fick's law, has been here considered. The Laplace equation for gas concentration γ is the field equation for the domain of permeable (continuous) phase in the system:

$$0 = \nabla^2 \gamma \tag{17}$$

Boundary conditions are then considered to insure zero mass flux across the interface between permeable phase and impermeable platelets ($\underline{n}$ being a vector normal to the interface):

$$0 = (\underline{\nabla}\gamma) \cdot \underline{n} \tag{18}$$

while the steady state permeate flux across the nanocomposite material can be evaluated after the solution for concentration γ in the system, from the integration of mass flux density j_ζ across any plane normal to ζ direction in Figure 3-1:

$$j_\zeta = -D_0 \frac{\partial \gamma}{\partial \zeta} \tag{19}$$

where D_0 is the diffusion coefficient in the permeable phase.

3.3.1 2-D ordered flake-filled systems

The problem of steady state diffusion within the elementary domain previously described was specifically analyzed for the numerical solution, with assigned values

γ_{in} and γ_{out} ($\gamma_{in} > \gamma_{out}$) for the concentration at the inlet and outlet boundaries of the domain, respectively.

To approach the numerical solution of the problem, the mentioned geometry was meshed to achieve a proper discretization of the computational domain; in particular finer grids have been used in correspondence to the critical points (Figure 3-2), such as the slit area, in order to better capture the mass gradients. A particular care has been also devoted in this step to achieve mesh independent results and minimize the solution time.

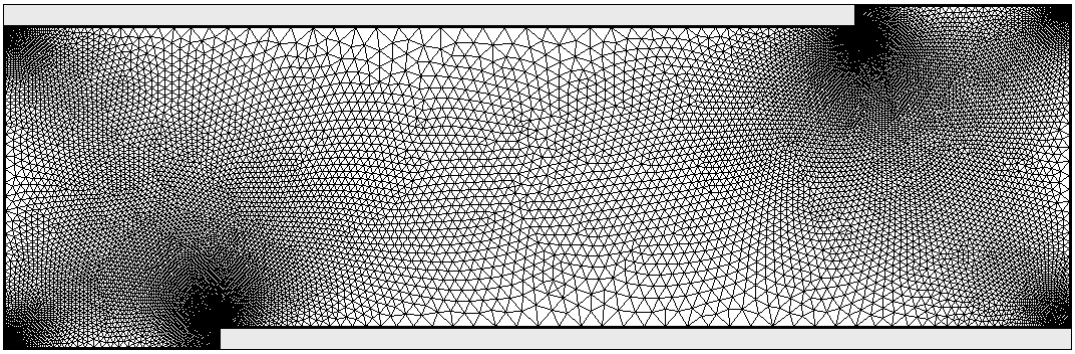

Figure 3-2, Discretized computational domain (α = 20, ϕ = 10, σ = 10).

The grid was then used to solve the above equations by using the well-established finite volume technique [15], which gives the concentration profile in the simulation box and allows to determine the gas flux at the inlet and outlet boundaries of the system considered; the diffusivity has been consequently calculated.

For all conditions considered, a simulation was performed also in a corresponding pure matrix domain, in order to validate the code and to obtain the correct reference for the unloaded homogeneous material. Indeed, all results are rescaled with values obtained for pure matrix and reported in terms of ratio between penetrant fluxes and indicated hereafter as effective diffusivity ratio.

3.3.2 2-D randomly distributed flake-filled systems

The different geometries were built through a purposely written algorithm that randomly places platelets of fixed thickness and variable length (standard deviation equal to 10% of the average aspect ratio) in the computational domain; no constraints in the polymer were imposed for the flakes position and only a check to avoid

overlapping was inserted in the code. The orientation of the platelets was kept fixed and parallel to the film surface, to limit the number of free parameters in the simulation and in view of the fact that, in many real systems, similar orientations are induced by the film forming procedures. The final disordered structures were similar to that shown in Figure 3-3 which presents a structure obtained for value of ϕ and α equal to 50 and 2.5% respectively the presence of periodic geometry distribution on the boundary parallel to average concentration gradients is visible which allows substantial reduction of the computational domain extension [4].

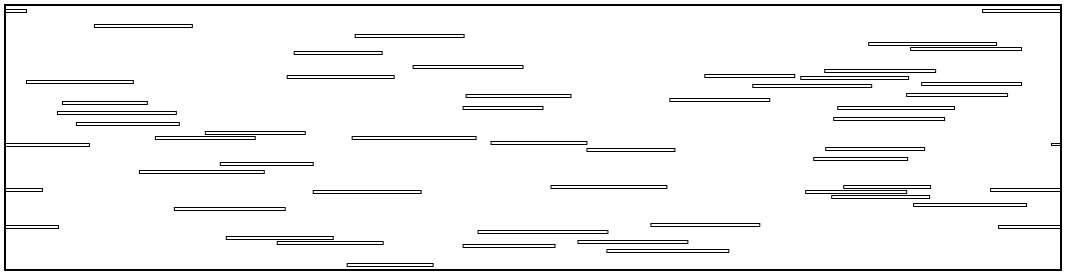

Figure 3-3, 2-D geometry filled by randomly distributed platelets (α = 50, ϕ = 2.5%).

During the simulative work, structures with aspect ratios of 10, 20, 50, 100, 150, 250 and 500 were explored at different filler concentrations, from 0.005 up to 0.20.

For each set of parameters (loading and filler aspect ratio) 10 different geometries were built and the obtained data were then averaged in order to obtain results that could be considered as not influenced by the particular structure tested and dependent only on mean values of α and ϕ.

The simulations performed converged after a certain time with residual dropped to values of 10^{-5} or less; the standard deviations obtained for diffusivity in the different structures instead were fairly dependent on the size of the structure, however they were ranging between 5 of 10 % in most of the cases and never exceeded the value of 15% even in the most complex structures. In this concern, it should be also noted that some authors stated a difference in the behavior of random system with mono-disperse rather than poly-disperse flake aspect ratio [12], however, as shown in Chen et al. [4], such differences are rather limited and in general lower than 10% which is close to the average value of standard deviation obtained for the present simulations. Therefore, in this work the problem was not directly addressed and only random arrays of poly-dispersed flakes, closer to real geometries, were considered.

3.3.3 3-D flake-filled systems

The lamellar structure, as usually considered in 2-D, has been transposed in a three-dimensional space by developing different ordered configurations, as shown in Figure 3-4, giving to the flakes several shapes. 3-D structures also require a new definition of the parameters α and σ that have to be unique for the different shapes of the platelets; hence the flake aspect ratio and the slit shape parameters become:

$$\alpha = \frac{S_n}{S_L} \tag{20}$$

$$\sigma = \frac{S_{n,H}}{S_L} \tag{21}$$

where S_n and $S_{n,H}$ are the areas of the surfaces normal to the flux direction of the flake and the hole region, respectively, while S_L is the area of the flake lateral surface.

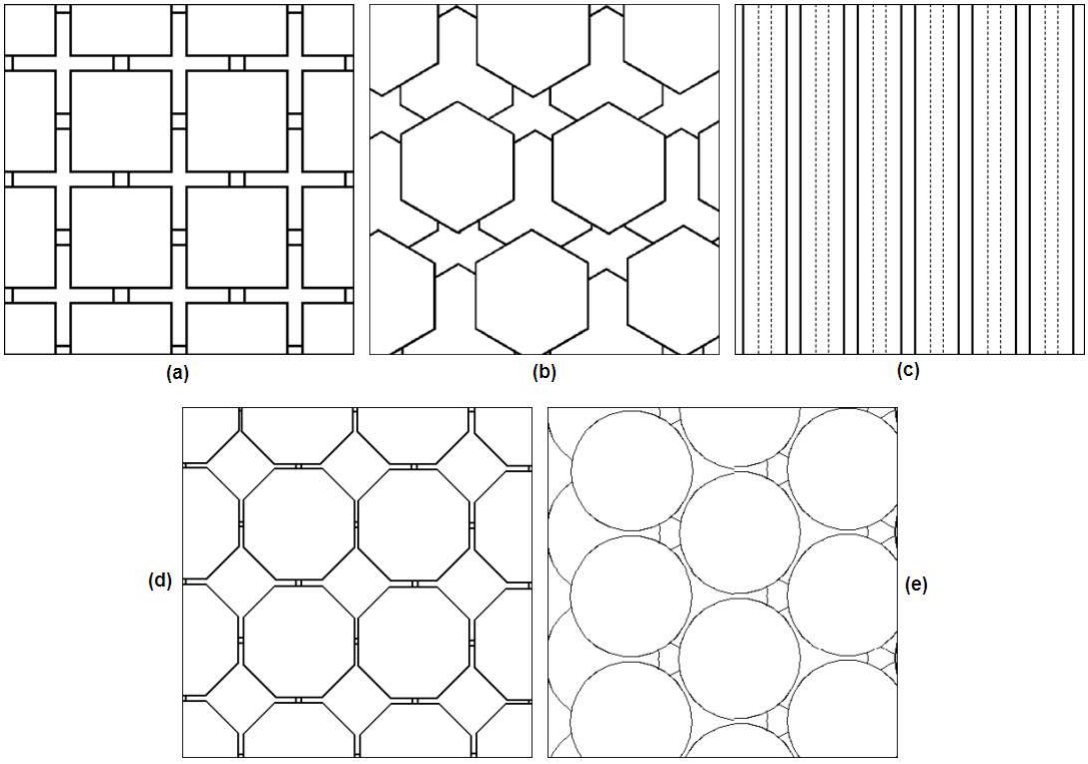

Figure 3-4, Three-dimensional heterogeneous ordered geometries in five different configurations: a) squares, b) hexagons, c) ribbons, d) octagons, e) circles.

As on can see from the layouts illustrated in Figure 3-4, ribbons (c) are developed by basically extruding the 2-D lamellae in the third direction; in fact, they have been

primarily considered to have a direct comparison of the two different approaches. In this case and also for squares and hexagons, a wide range of slit dimensions can be explored, because in these configurations, in the limit consecutive flakes when their edges are overlapped, the structure is blocking completely the diffusing molecules and the resistance has to be assumed as infinite. On the contrary, this cannot be achieved for octagonal or circular platelets, and so, although they probably are able to better mimic the shape of real flakes, their investigation at this stage is limited to very few cases.

Similarly to what have been done in the case of 2-D ordered systems, a wide range of aspect ratios has been investigated, from 5 to 300 with loadings between 0.5 and 10%; slit shape was also varied between 0.5 and 5.

3.3.3.1 3-D randomly distributed flake filled systems

In the case of random systems, geometries were defined by randomly placing a certain number of circular, or squared platelets (in this case just those two configurations have been taken in account) in the simulation box, the overlapping of the flakes was the only restriction considered. In this way, random structures were obtained as the one showed in Figure 3-5.

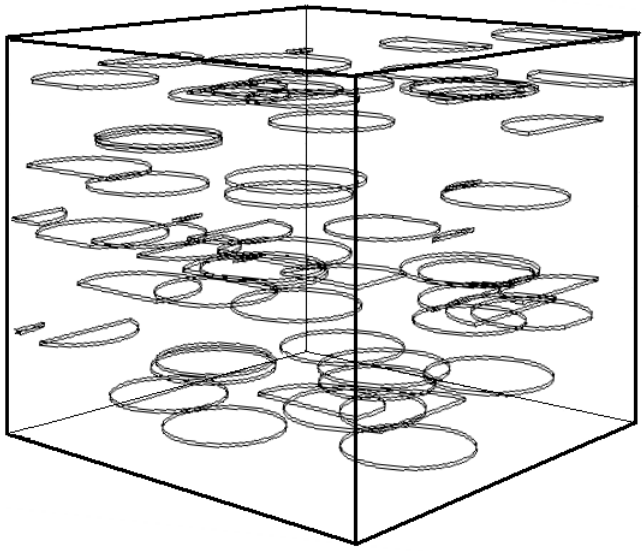

Figure 3-5, Layout of a 3-D random geometry with circular platelets.

In order to mimic the poly-dispersity of filler dimension in the real composite the aspect ratio α of the platelets was allowed to vary, a standard deviation of about 10% of the average value of α was indeed used to obtain a normal distribution of such parameter in the geometry.
The same procedure and the same solver previously described were used in case of 3-D randomly distributed systems. It should be noticed that, for same set of parameters (namely α and ϕ), simulations were performed on different geometries in order to obtain results independent from the particular structure tested.

3.4 Results

3.4.1 2-D ordered flake-filled systems

Rather different values have been explored for structure parameters in flake filled systems, aspect ratios in the range from 10 to 200 were explored, while slit shape different up to three orders of magnitude were considered, from highest value 5 down to lowest value 0.005. Attention was then focused on relatively low loading range not exceeding 25% of volume fraction. Specific values of α, σ and ϕ were chosen to allow specific comparison with results from previous simulations, while in general terms preference has been given to simulation at relatively low α/σ ratio, which should correspond to more severe conditions for the prediction of the above described simplified model. Table 3-1 summarizes the results for enhancement in barrier properties of flake filled system as obtained in simulations performed in this work.

Table 3-1a, (D_0/D_{ff}) results from simulations for ordered flake filled 2-D systems (α=10, 20).

ϕ (%)	α = 10				α = 20			
	σ = 0.005	σ = 0.05	σ = 0.5	σ = 5	σ = 0.005	σ = 0.05	σ = 0.5	σ = 5
0.5	11.6	2.32	1.29	1.12	22.2	3.73	1.65	1.27
1.25	27.2	4.31	1.71	1.30	53.6	7.81	2.63	1.67
2.5	53.4	7.61	2.46	1.60	106	14.6	4.26	2.37
5	106	14.2	3.93	2.34	211	28.4	7.67	4.24
7.5	158	20.9	5.44	3.40	317	42.5	11.5	7.00
10	211	27.6	7.06	4.86	423	57.1	15.8	10.8
15	316	41.4	10.7	9.17	636	87.6	26.1	22.0
20	423	55.8	15.1	15.7	853	121	39.5	39.2
25	527	70.9	20.5	25.1	1070	157	56.7	63.9

Table 3-1b, (D_0/D_{ff}) results from simulations for ordered flake filled 2-D systems (α=30, 50).

ϕ (%)	α = 30				α = 50			
	σ = 0.005	σ = 0.05	σ = 0.5	σ = 5	σ = 0.005	σ = 0.05	σ = 0.5	σ = 5
0.5	32.7	5.17	2.04	1.44	53.8	8.10	2.88	1.82
1.25	81.1	11.5	3.61	2.09	135	18.9	5.72	3.09
2.5	160	21.9	6.25	3.31	266	36.8	10.7	5.65
5	319	43.2	12.1	6.74	540	74.8	22.5	13.3
7.5	478	65.6	18.8	11.8	803	115	32.2	25.2
10	638	88.7	26.7	18.9	1080	159	55.3	41.8
15	964	139	46.8	40.1	1630	258	104	92.1
20	1295	196	73.9	72.5	2210	377	173	169
25	1634	261	110	119	2810	519	265	278

Table 3-1c, (D_0/D_{ff}) results from simulations for ordered flake filled 2-D systems (α=75, 100).

ϕ (%)	α = 75				α = 100			
	σ = 0.005	σ = 0.05	σ = 0.5	σ = 5	σ = 0.005	σ = 0.05	σ = 0.5	σ = 5
0.5	64.5	12.2	4.01	2.37	103	15.6	5.18	2.96
1.25	205	28.3	8.60	4.57	254	38.3	11.7	6.29
2.5	406	56.4	17.1	9.38	540	79.6	24.4	13.9
5	805	117	38.5	24.6	1080	162	57.9	39.1
7.5	1216	184	67.0	48.7	1637	260	104	79.8
10	1630	259	104	83.0	2210	373	166	138
15	2500	437	205	187	3399	649	340	314
20	3410	659	352	345	4680	1010	594	584
25	4372	934	554	571	6037	1454	947	968

Table 3-1d, (D_0/D_{ff}) results from simulations for ordered flake filled 2-D systems (α=150, 200).

ϕ (%)	α = 150				α = 200			
	σ = 0.005	σ = 0.05	σ = 0.5	σ = 5	σ = 0.005	σ = 0.05	σ = 0.5	σ = 5
0.5	101	23.3	7.67	4.28	214	31.7	10.3	5.77
1.25	379	58.2	18.7	10.4	471	79.9	26.5	15.3
2.5	805	121	41.4	25.5	1087	166	61.4	40.2
5	1637	266	107	78.1	2217	377	168	130
7.5	2502	436	202	165	3396	642	330	280
10	3394	646	332	290	4629	969	553	497
15	5302	1173	708	669	7315	1828	1209	1156
20	7383	1881	1266	1250	10378	3010	2188	2170
25	9680	2807	2044	2070	13743	4579	3556	3600

As expected, the barrier enhancement effect increases as flake loading increases at constant α and σ. Similarly, the higher the aspect ratio of flakes, the higher the decrease of permeability for the flake filled system. It should be noted however, that the enhancement in barrier effect is not monotonous with slit shape, at constant α and ϕ. Indeed, at constant aspect ratio and loading, the larger the distance between adjacent flakes on the same plane, the shorter the distance between two successive flakes plane. Then, at low slit shape, where "hole" resistance dominates, an increase in slit shape results in a decrease of the overall barrier effect. At relatively high slit shape, on the other hand, an increase in σ can induce a decrease in permeability as result from the increase in "tortuous path" resistance.

Those two different contributions to the overall resistance to the diffusion are shown in Figure 3-6, where the results are reported in a double logarithmic scale to highlight the behavior of the (D_0/D_{ff} - 1) factor with the parameter $\alpha\phi$, which allows, considering the mathematical model above described (Eqs. (9-12)), to easily evaluate the dominant resistance in the system through the analysis of the results with a simple power law:

$$\left(\frac{D_0}{D_{ff}} - 1\right) = A \cdot (\alpha\phi)^n \qquad (22)$$

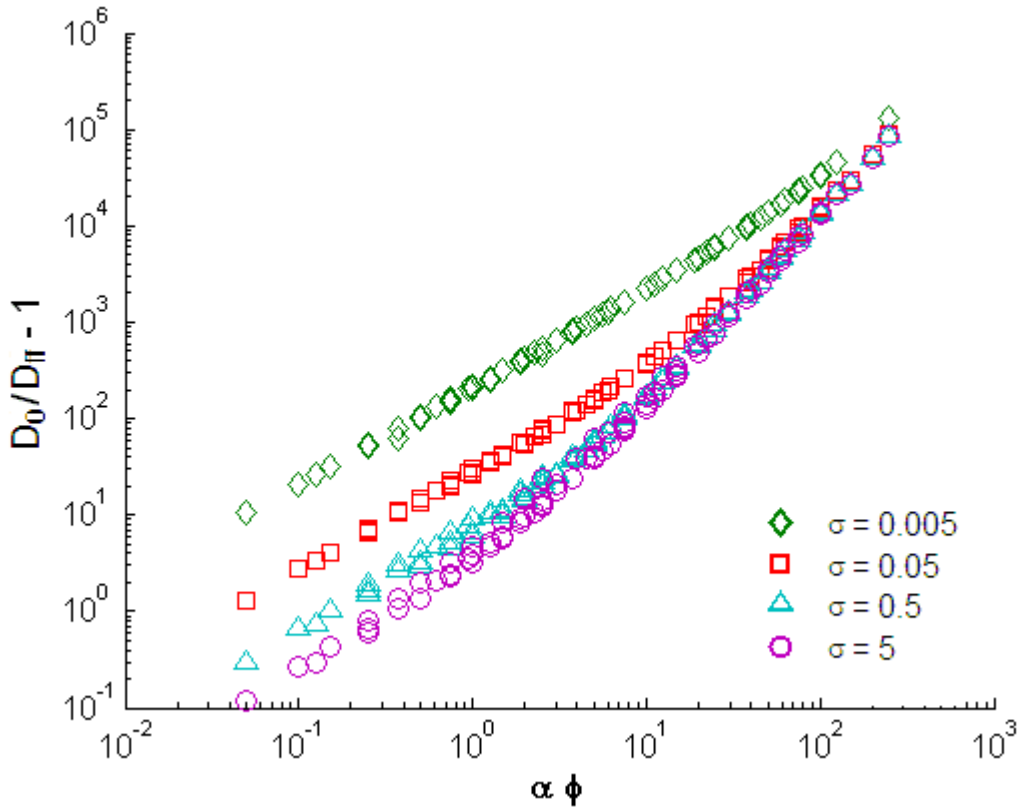

Figure 6, Trends for the enhancement in barrier properties (D_0/D_{ff} - 1) in flake filled systems for different slit shapes (σ = 0.005, 0.05, 0.5, 5).

There exists, indeed, a double behavior for all the cases considered (σ = 0.005, 0.05, 0.5 and 5). When the platelets are relatively small and the system is not so concentrated ($\alpha\phi$ small), there is a linear dependence of the barrier effect with the $\alpha\phi$ parameter; in this range indeed the largest contribution is given by the resistance within the slit between two consecutive flakes while the tortuosity plays a marginal role. On the contrary, at high values of $\alpha\phi$, the barrier properties behave with a quadratic trend, as the wiggling effect gains relevance with respect to the "hole" resistance. It should also be noticed that at very high $\alpha\phi$, on the right side of the plot, the four curves at different slit shape values converges to the same trend; this is further proof of the fact that when the aspect ratio is high and the system is concentrated the hole resistance is negligible.

3.4.1.1 Comparison with previous simulations

Several efforts have been carried out in the past to evaluate the enhancement in barrier properties produced by ordered dispersion of impermeable flakes in a matrix which can be described in terms illustrated above. Simulations reported by Chen et al. [4] were performed through a different numerical solution of the same continuous mechanics problem here considered for the discussion of the permeation process. Simulation results reported by Falla et al. [3] and Swannack [6], instead, refer to a Monte Carlo approach to the description of same hindered diffusion problem.

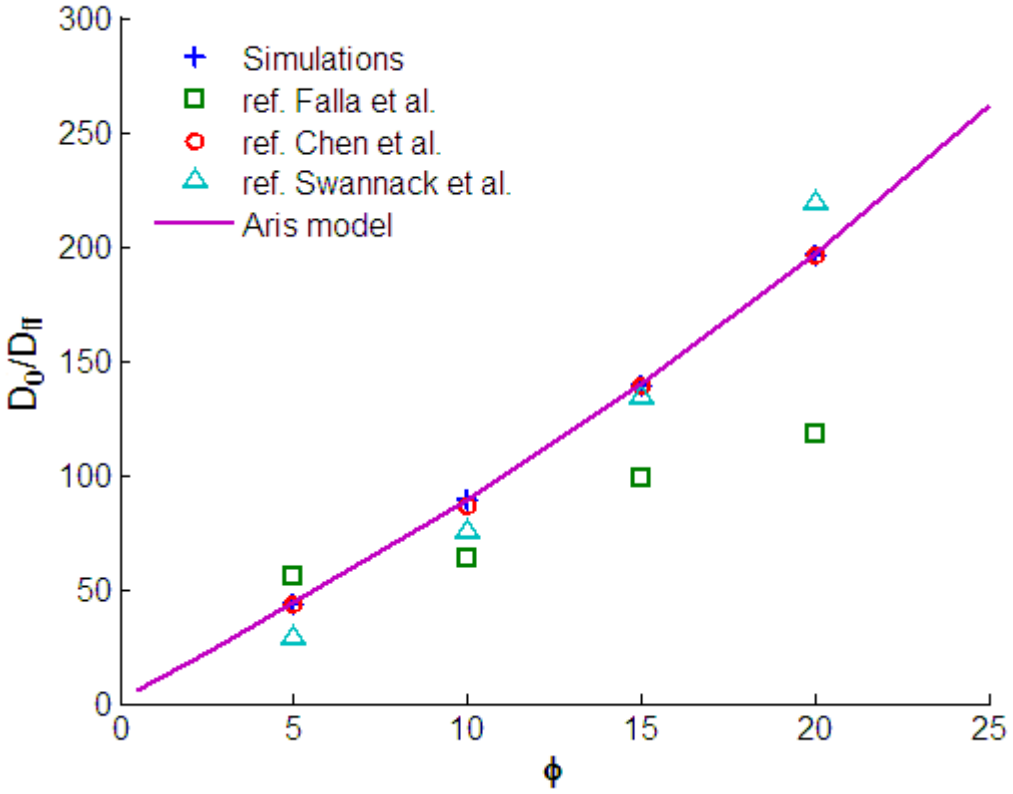

Figure 3-7, Comparison of simulation results for enhancement in gas barrier properties for 2-D ordered flake filled systems ($\alpha = 30$, $\phi = 0.05$)

In Figures 3-7, 3-8 and 3-9 data for enhancement barrier effect for the case of $\alpha = 30$ as obtained from simulations performed in this work are compared with corresponding value obtained in mentioned works, together with the prediction from the model due to Aris, Eq. (9). In all cases, relative increase in permeation resistance from pure matrix to flake filled systems form simulations, expressed as (D_0/D_{ff} - 1), are reported as function of particle loading.

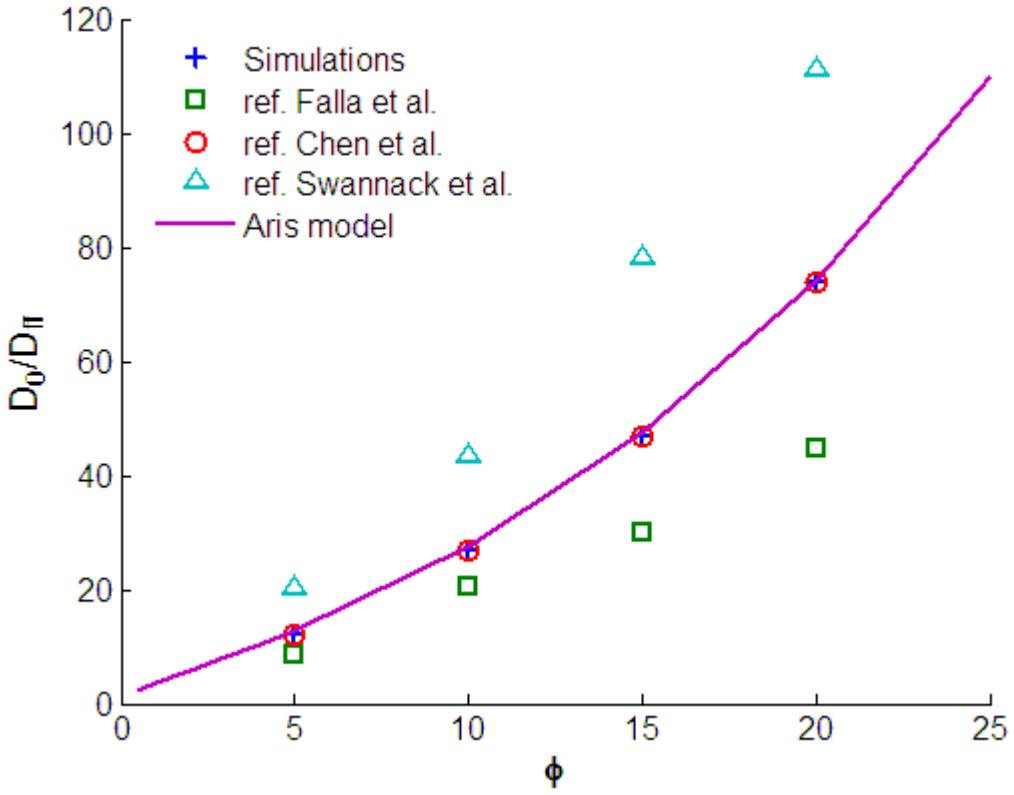

Figure 3-8, Comparison of simulation results for enhancement in gas barrier properties for 2-D ordered flake filled systems ($\alpha = 30$, $\phi = 0.5$).

In Figures 3-7, 3-8 and 3-9 data are shown for the case of $\sigma = 0.05$, $\sigma = 0.5$ and $\sigma = 5$, respectively. It clearly results from comparison in these plots that while results from this work and those by Chen are definitely consistent with each other, results obtained from different modeling approaches show values significantly different, sometimes difficult to interpret in terms of parameter effects.

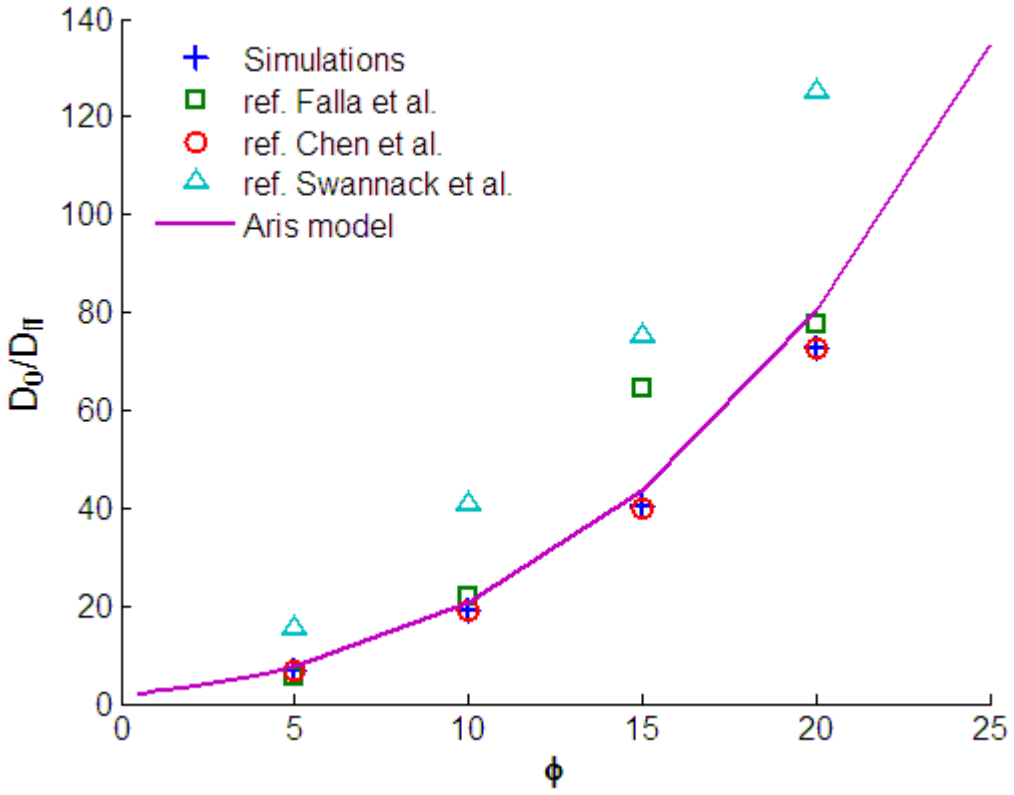

Figure 3-9, Comparison of simulation results for enhancement in gas barrier properties for 2-D ordered flake filled systems (α = 30, ϕ =5).

As a further analysis of the set of data from simulation obtained from different approaches, data have been shown in the plots also for the results of model in Eq. (9). Comparison of predictions from latter model and output from simulations put in evidence an excellent agreement in the inspected range of α, σ and ϕ between numerical results and simplified analytical model considered in this work, while questions the data obtained in some of the simulations performed in earlier works.

3.4.1.2 Comparison with previous model predictions

In order to compare results from the simplified expression proposed in this work for the enhancement in barrier properties for flake filled systems (Eq. (9)) and those considered in previous works, a series of parity plots have been built (Figures 3-10, 3-11, 3-12 and 3-13), which separately account for the accuracy of distinct models in predicting the results obtained by numerical calculations performed in this work.

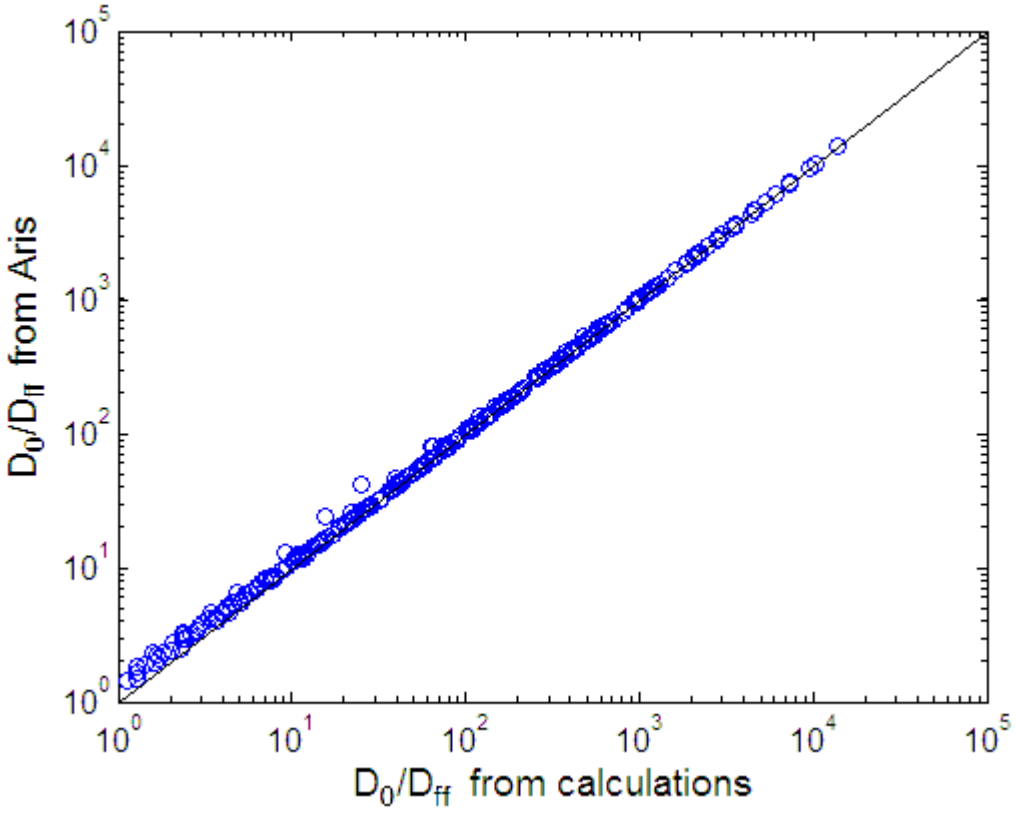

Figure 3-10, Comparison between numerical results for enhancement in gas barrier properties for 2-D ordered flake filled systems and prediction from Aris, Eq. (9).

In Figure 3-10, the parity plot for calculated (D_0/D_{ff}) and from model in Eq. (9) is shown for all sets of structure parameters considered in this work. It can be appreciated that an excellent agreement is obtained in all cases, with few exceptions, more frequently observed at low enhancement in barrier properties, i.e. low (D_0/D_{ff}) values, pertinent to the case of low ($\alpha\phi$) or low (α/σ) values, for which the accuracy of Eq. (8) in representing "tortuous path" resistance is not satisfactory.

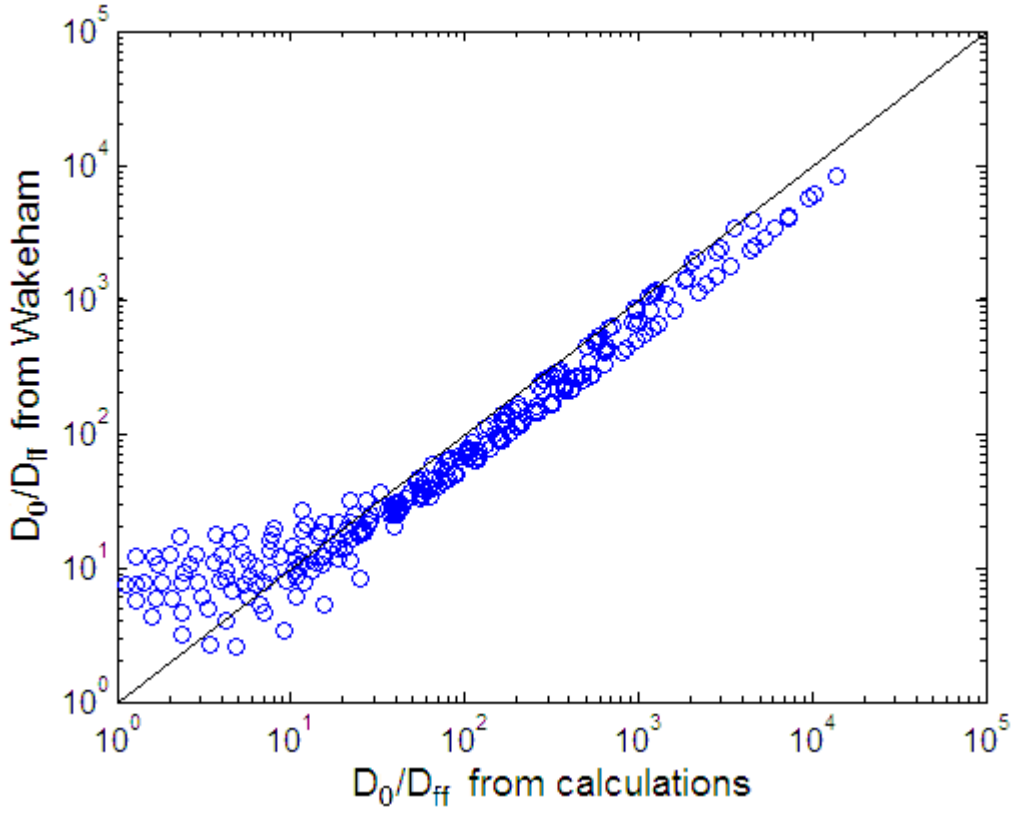

Figure 3-11, Comparison between numerical results for enhancement in gas barrier properties for 2-D ordered flake filled systems and prediction from Wakeham, Eq. (12).

In Figures 3-11 and 3-12 parity plots are shown for the comparison of the numerical calculation results with prediction obtained from models by Wakeman and Mason or by Cussler, first or second approximation, respectively. Previous models here considered clearly offer a less accurate representation of the barrier enhancement in flake filled ordered systems with respect to the new expression in Eq. (9). This is partly due to the effect of correction for ratio σ/α in the "hole" resistance which is missing in previous models, but it is mainly the result of the incorrect expression assumed for the contribution by "tortuous path" resistance to the mass flow in earlier works.

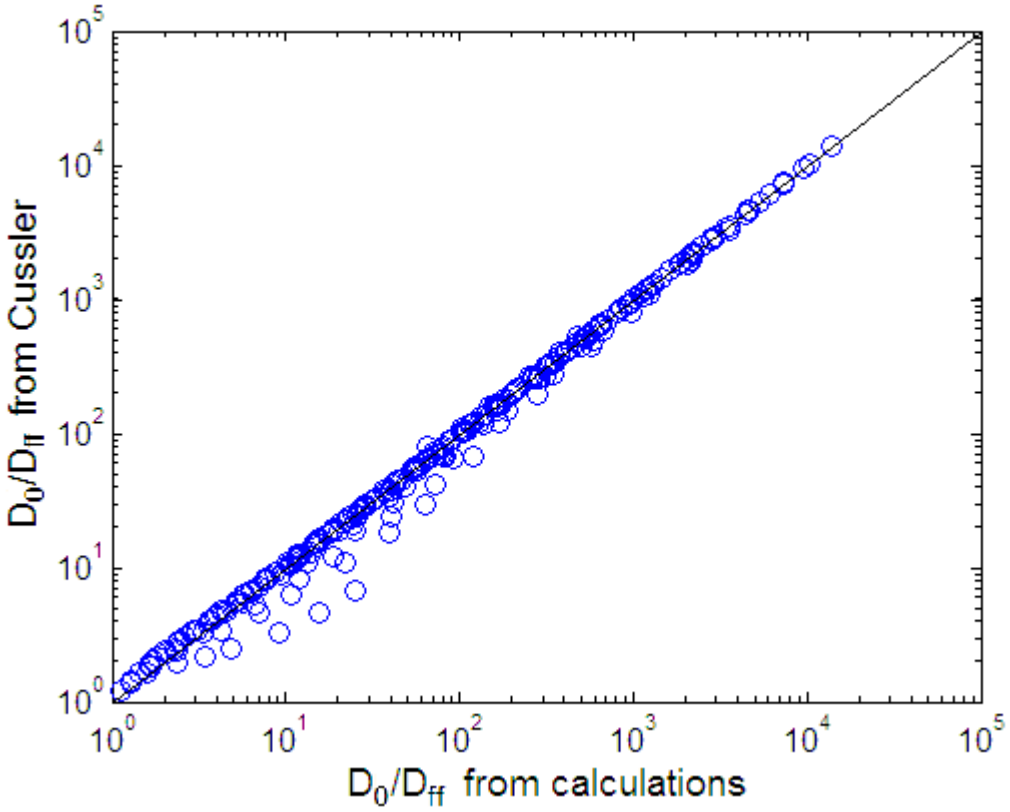

Figure 3-12, Comparison between numerical results for enhancement in gas barrier properties for 2-D ordered flake filled systems and prediction from Cussler, Eq. (10).

This is also evident from the comparison of parity plot for calculated results against prediction from Eq. (10) and that against results from Eq. (11). Indeed from the above comparison, it cannot be concluded that Eq. (11) represents a refinement of predictions obtained by Eq. (10) as the average distance between numerical analysis and predictions in Figure 3-13 is even larger than corresponding value in Figure 3-12.

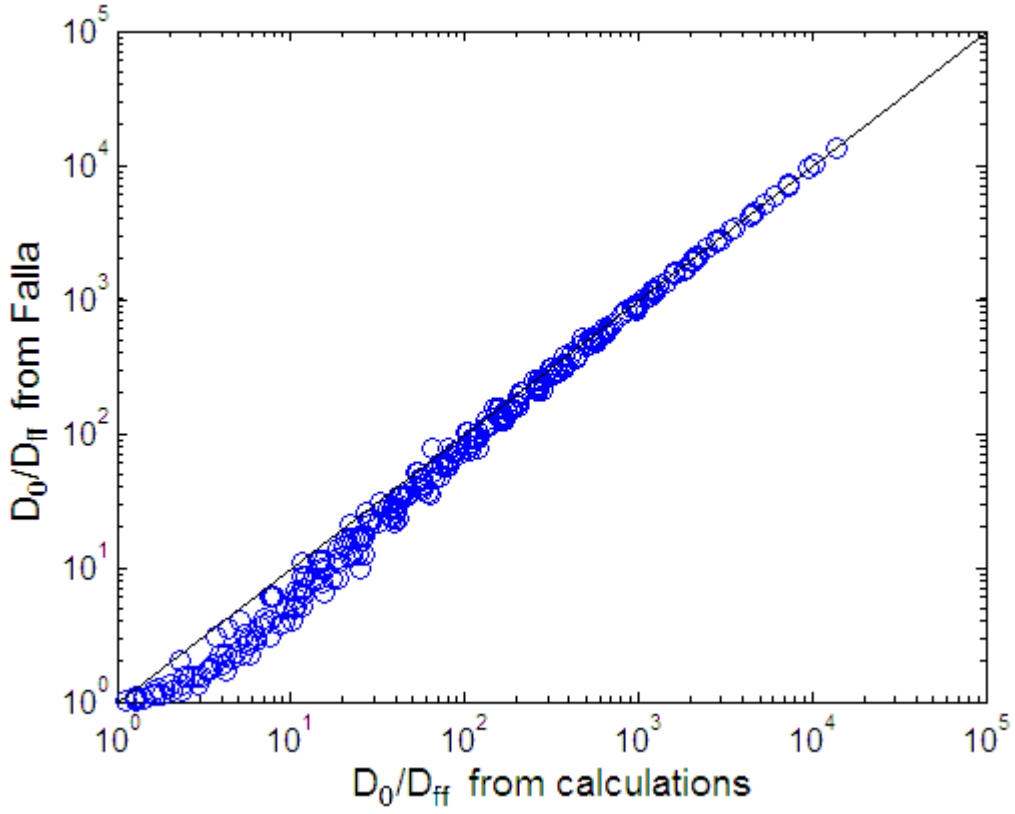

Figure 3-13, Comparison between numerical results for enhancement in gas barrier properties for 2-D ordered flake filled systems and prediction from Falla, Eq. (11).

In fact, additional contribution in Eq. (11) with respect to Eq. (10) is just derived from the incorrect expression of tortuous path resistance reported in the original work by Aris.

The results that have been shows provide the necessary background for the proposed method of calculation and prove the ability of the latter to mimic the effect of the dispersion of an impermeable phase into a continuous moiety in the comparison with the almost complete and rigorous solution given by Aris.

3.4.2 2-D randomly distributed flake-filled systems

The numerical calculations were then focused on disordered systems where the impermeable phase was randomly distributed in the simulation box. In order to investigate all the possible regimes, different geometries were built with α values varying from 10 to 500, while the loading was in the range 0.005 to 0.25. The

corresponding results are reported in Table 3-2 in terms of enhancements in barrier effect, D_0/D, of flake filled system as obtained in the performed calculations.

Table 3-2, (D_0/D_{ff}) results from simulations for ordered flake filled 2-D systems

α	ϕ	D_0 / D_{ff}
10	0.005	1.05
	0.0125	1.14
	0.025	1.30
20	0.005	1.11
	0.025	1.63
	0.05	2.56
	0.10	4.56
50	0.025	3.03
	0.05	6.38
	0.10	14.6
75	0.025	4.58
	0.05	10.7
	0.10	26.5
100	0.025	6.49
	0.05	16.1
	0.10	41.4
	0.15	69.1
	0.20	95.4
200	15	226
	20	341
500	10	685
	15	1215
	20	1748

As expected, and as already showed for the case of ordered structures, the barrier enhancement effect increases as flake loading increases at constant α and, similarly, the higher is the aspect ratio of flakes, the higher is the decrease of permeability for the composite system.

Figure 3-14 reports the factor (D_0/D_{ff} - 1) as function of a unique parameter $\alpha\phi$ in a double logarithmic scale as calculated from the simulations in random structures to show the two different trends already described for the case of ordered geometries (as indicated in Eq. (22)).

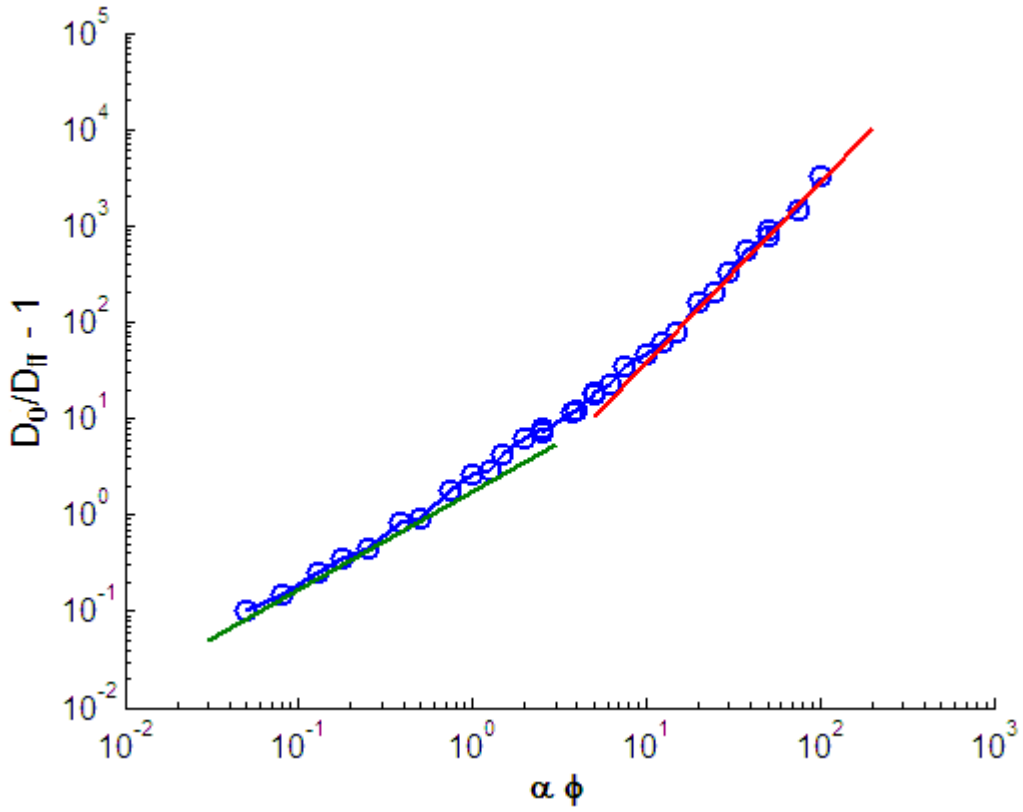

Figure 3-14, Trends in enhancement in barrier properties (D_0/D_{ff} - 1) for 2-D randomly distributed systems.

The random flake-filled structure can be completely described, as far as diffusion properties are concerned, by a single parameter given simply by the product of filler loading and platelet aspect ratio. This behavior is substantially different from what observed in the case of ordered flakes arrays where another parameter was required to describe the system, namely the slit shape σ, which, however, looses its physical meaning in random geometries. Moreover, it can be noticed that when a geometry is developed in a random configuration, the barrier effect that can be guaranteed is always smaller then the one in ordered structures, as will be better discussed later indeed the general shape of the different curves presented in Figure 3-15 for ordered and disordered systems is rather similar, but the random curve seems somewhat shifted toward smaller diffusivity reductions.

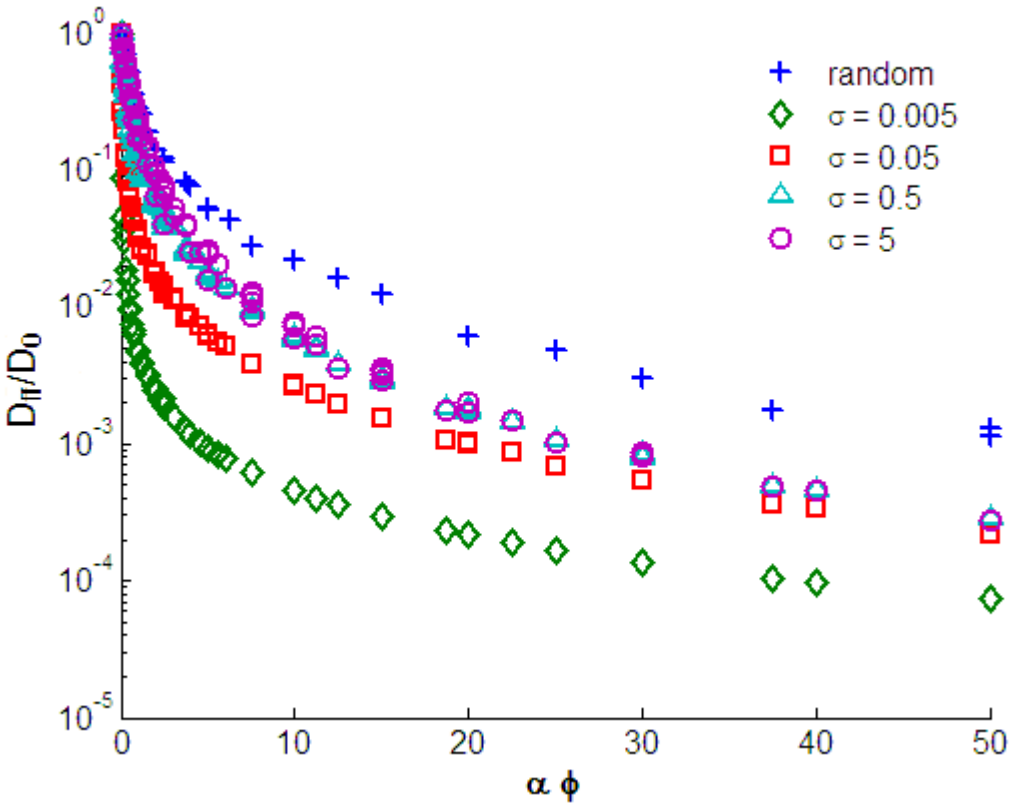

Figure 3-15, Diffusivity decrement (D_0/D_{ff}) in randomly distributed systems in comparison with results from calculations in ordered geometries.

From a qualitative point of view, such behavior is easily predictable; in highly ordered systems, indeed, the regular disposition of the platelet avoids any shortcut inside the composite and maximizes the path of the diffusing molecule. On the contrary, in random structures it is possible to find clusters of lamellae as well as areas with lower filler concentration; the presence of shortcuts is therefore unavoidable and such easy paths are preferentially used by the penetrant molecules to diffuse across the membrane.

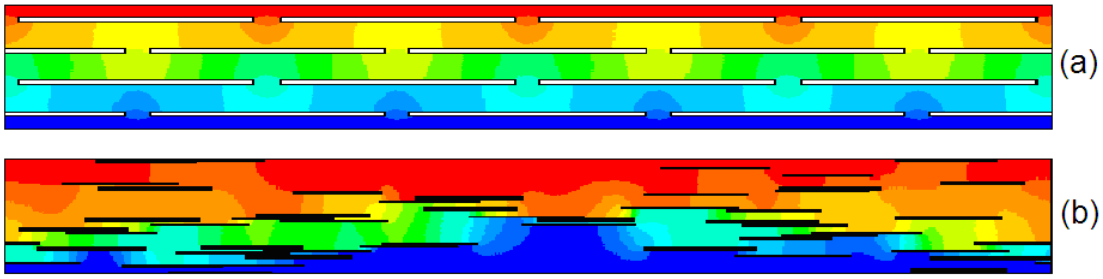

Figure 3-16, Concentration profiles in ordered (a) and random (b) distributed flake filled systems.

In this concern, Figure 3-16 shows the concentration profile for both ordered (a) and random geometries (b). As it can be seen, the concentration across the membrane gradually decreases following the paths with lower tortuosity for both types of structure. In case of ordered geometries, however, there exist a periodic structure which is repeated and the tortuosity is homogeneously distributed throughout the system: the flux of the diffusing species leaving the system will be therefore periodic with maxima in correspondence of the position of the slits; on the other hand, in the random system, the same flux is randomly distributed along the outlet boundary of the computational domain.

To account for the different flakes distribution, it can be stated that, in actual fact, there exists, for every given random composite, an equivalent ordered structure, which, as expected, is characterized by lower flakes aspect ratio then the ones in "real" system; in random geometry indeed the flakes are often not distributed homogeneously, they tends to form sort of clusters which, obviously, have lower aspect ratio with respect to the single lamella.

In order to compare the results obtained in this work with all the models proposed in case of random distribution of flakes in a polymeric phase, a series of parity plot have been proposed in the following figures.

In Figure from 3-17 to 3-20 four different parity plots of (D_0/D_{ff}) from simulations in 2-D random flake filled geometries and from the four models that are above described are presented.

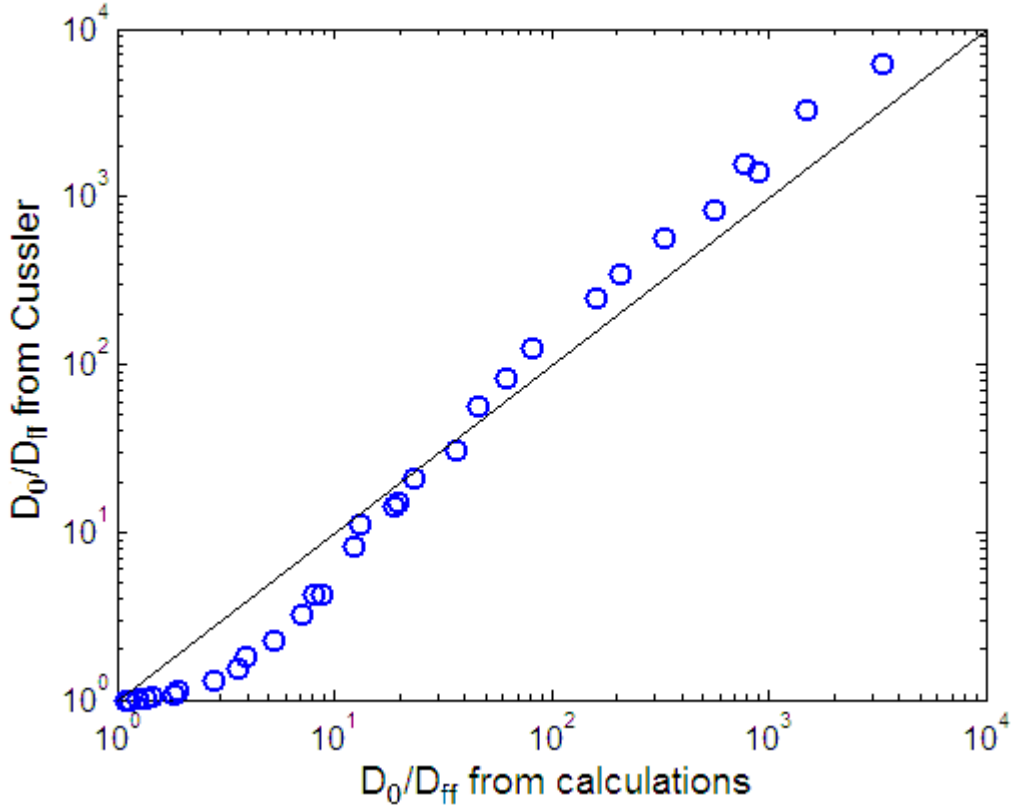

Figure 3-17, Comparison between numerical results for enhancement in gas barrier properties for 2-D random flake filled systems and prediction from Cussler, Eq. (14).

In Figure 3-17, the enhancement in barrier properties obtained from the numerical calculations has been compared with the prediction from Cussler equation (Eq. (14)) in which the adjustable parameter μ, supposed to account for the misalliance of the flakes, has been considered as equal to 0.5 as suggested in a following paper [10] for the case of long ribbon-like platelets.

The trend seems to be fairly correct at high values of the diffusivity enhancement, corresponding to large $\alpha\phi$, where the simulations show a quadratic behavior but the absolute value of the predictions are rather different to the results from the numerical calculations; on the contrary, at small $\alpha\phi$, the model shows a completely different trend with respect to numerical results and completely overestimates the barrier effect in such systems.

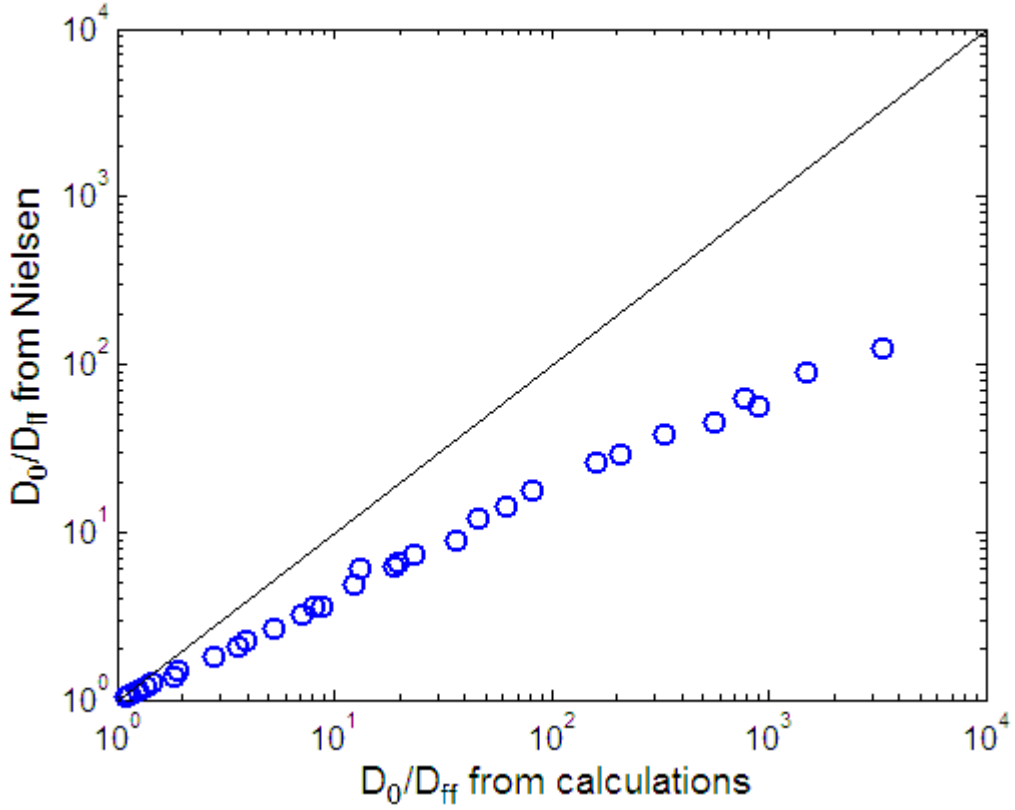

Figure 3-18, Comparison between numerical results for enhancement in gas barrier properties for 2-D random flake filled systems and prediction from Nielsen, Eq. (13).

On the other hand, in the range of small $\alpha\phi$, Nielsen model, reported in Figure 3-18, is able to mimic the initial (linear) behavior of barrier enhancement effect, but, when that parameter is further increased, Eq. (13) predict a D_0 / D_{ff} much lower then the one obtained in the simulations. In case of Fredrickson model reported in Figure 3-19, the parity plot shows that the predicted behavior seems to be reasonable and able to capture the trend only in the range of very small α and ϕ. However, for higher values the model predictions look quite different to the results obtained from numerical calculations, and completely not too accurate in describing the problem. It has to be noticed that the Fredrickson model was developed considering a slightly different point of view because its approach was performed in three dimensions.

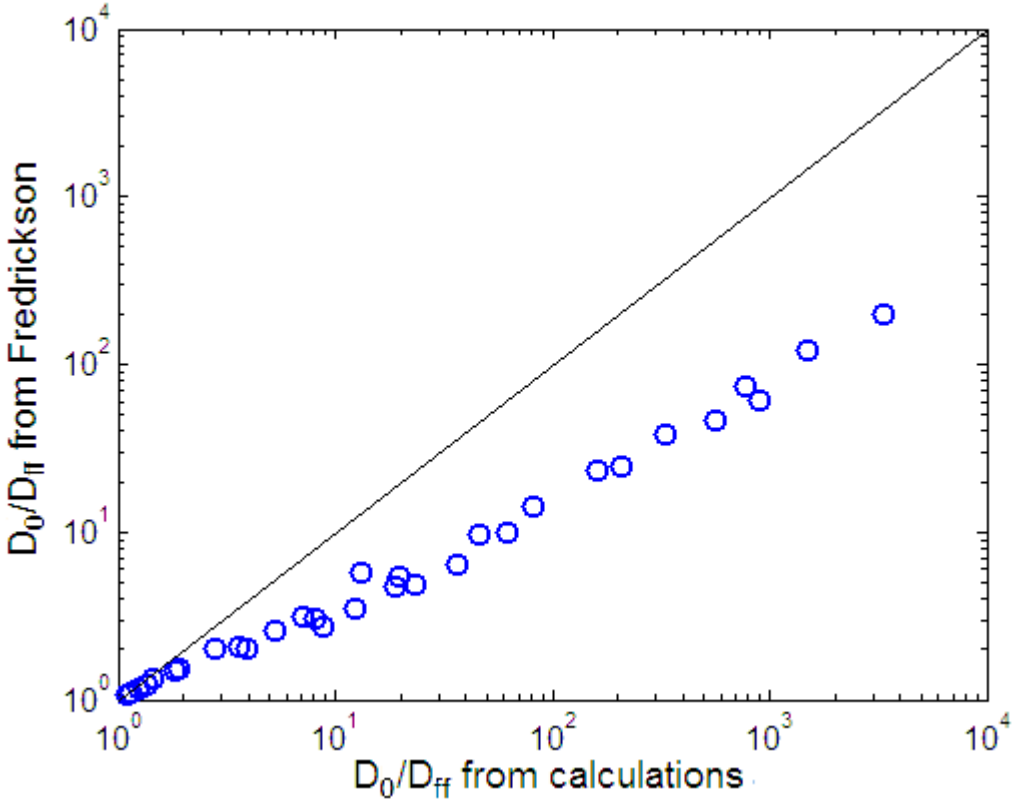

Figure 3-19, Comparison between numerical results for enhancement in gas barrier properties for 2-D random flake filled systems and prediction from Fredrickson, Eq. (15).

Figure 3-20 reports the parity plot for the simulation results and the model due to Lape, and as one can se, the agreement is remarkable; even if at high values of $\alpha\phi$, where the barrier effect is small, there is a slight deviation, there is not any drift at smaller values. The ability of this equation to mimic the enhancement in barrier effect is probably due to its approach directly focused in the conditions here discusses of randomly distributed geometries and specifically developed in two dimensions.

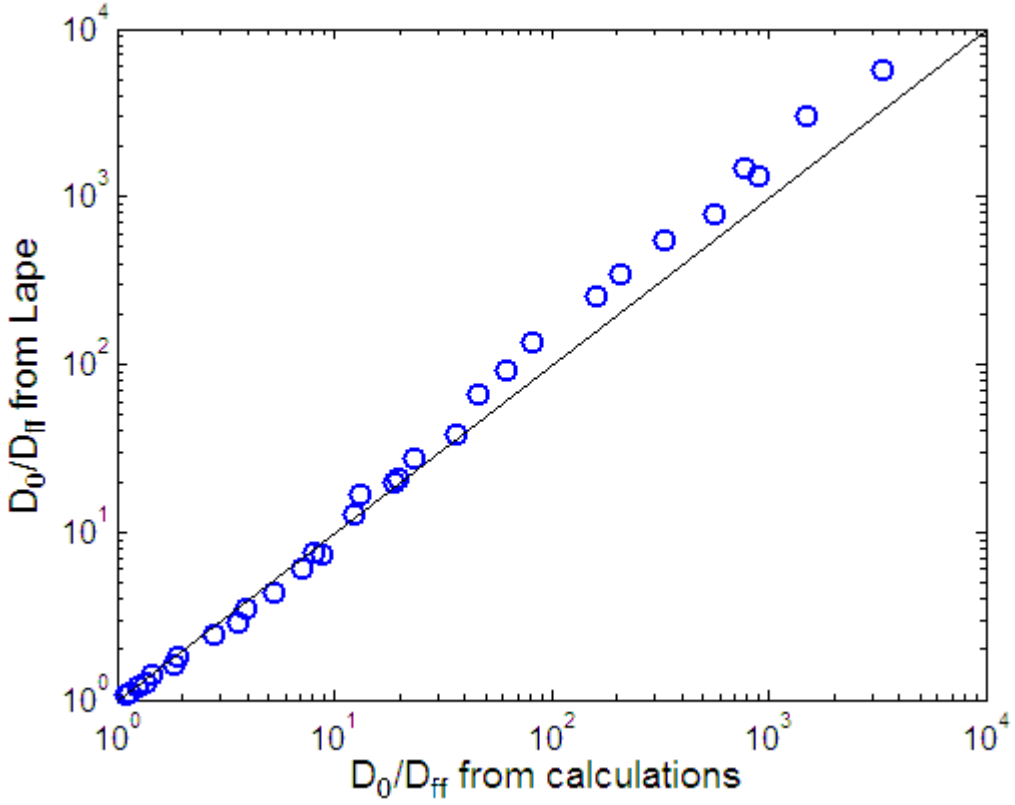

Figure 3-20, Comparison between numerical results for enhancement in gas barrier properties for 2-D random flake filled systems and prediction from Lape, Eq. (16).

3.4.3 Effect of a third phase

The proposed algorithm is able to capture the behavior of the barrier effect given by heterogeneous systems where an impermeable phase fills a polymer matrix. This method is based on the assumption that the properties of the organic phase are not affected by this addition, i.e. the diffusivity of the system is punctually equal to D_0 (pure polymer diffusivity) anywhere in the structure except in correspondence to the impermeable flakes where there is a discontinuity and D is zero.

In real systems, several events can occur during the synthesis, or the filming procedure, and the properties of the organic phase might change. In some cases the adhesion between the two phases is poor and several voids are concentrated in correspondence to the flake interface where the diffusivity can be assumes as very high; on the contrary, the presence of a new element in the polymeric matrix can promote a more connected and stronger network of the macromolecules, or, in case of

semi-crystalline polymer, the crystallinity can be locally enhanced. This leads to a third layer close to the filler surface with a diffusion coefficient smaller then the one in the pure polymer.

In this concern, it is of interest to see how these two phenomena influence the overall diffusivity; consequently, a series of simulations have been performed on randomly distributed 2-D systems considering three different phases (polymer, interlayer and flakes). A single aspect ratio has been explored, 50, with 2 different loadings, 0.05 and 0.10; the thickness of the interlayer, t_i, was chosen equal to 0.5, 1 and 5 times the thickness of the lamella, t, while its diffusivity D_i has been varied in the range 0.1 - 10 times the pure polymer diffusivity (D_0). Figure 3-21 shows an example of this three-phase structure.

Figure 3-21, Layout of 2-D geometry with randomly distributed platelets ($\alpha = 10$, $\phi = 5$) with interlayer: a) overall structure; b) detail of the third phase, in red.

Then, once the geometry has been developed, the same procedure above described was applied solving the Fick's law in the computational domain; the concentration profiles and the transport properties in the composite media were thus determined.

This route allows the calculation of the effective diffusion coefficient, and the results are listed in Table 3-3 in terms of enhancement in barrier properties with respect to the unfilled pure polymeric matrix (D_0/D_{ff}).

Table 3-3, (D_0/D_{ff}) results in three-phases 2-D random flake filled systems (α = 50; ϕ = 0.05, 0.10)

	ϕ = 0.05			ϕ = 0.1		
D_i/D_0	t_i/t = 0.5	t_i/t = 1	t_i/t = 5	t_i/t = 0.5	t_i/t = 1	t_i/t = 5
0.1	10.2	12.2	12.6	22.7	24.0	38.6
0.5	10.0	10.3	11.1	21.1	22.5	24.6
1	8.94	8.80	8.61	17.7	17.4	17.1
3	8.14	7.27	4.31	14.4	11.1	8.84
5	7.68	6.28	3.20	11.5	8.57	6.15
10	5.69	4.47	2.14	9.58	6.49	3.74

This third phase is able to play a relevant role in changing the transport properties of these barrier membranes; depending on the size of the interlayer and also on the configuration of the system, D_0/D_{ff} can change even of a factor 5.

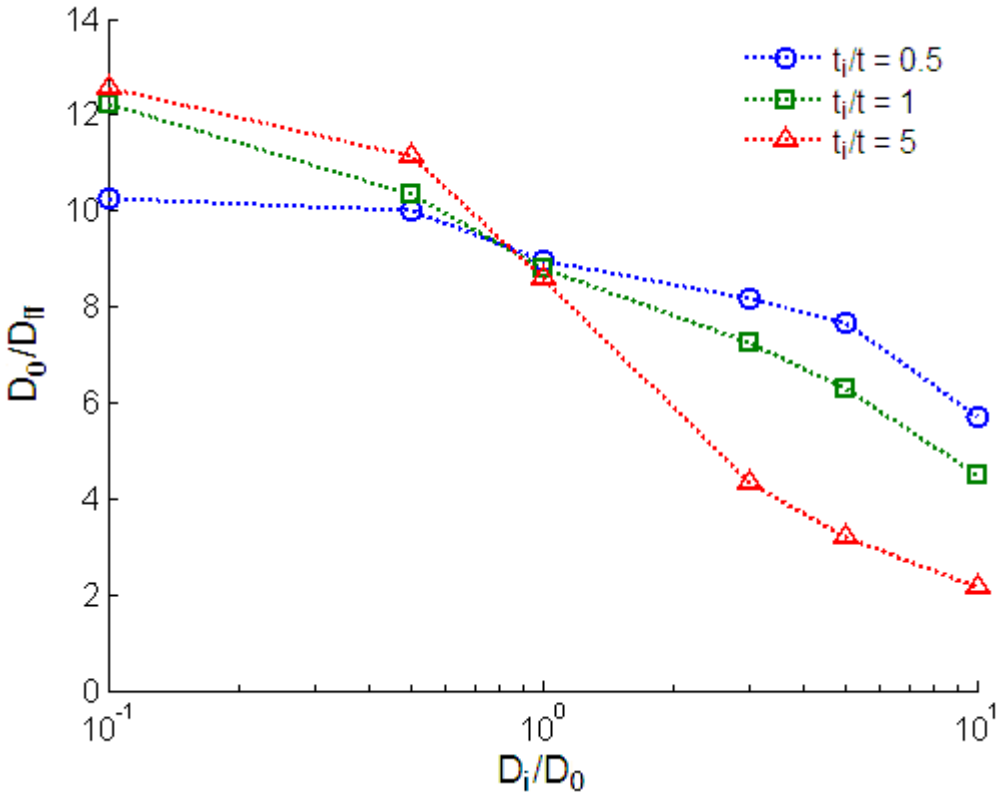

Figure 3-22, (D_0/D_{ff}) for 2-D systems with randomly distributed platelets and with an interlayer of variable diffusivity (α = 50, ϕ = 0.05).

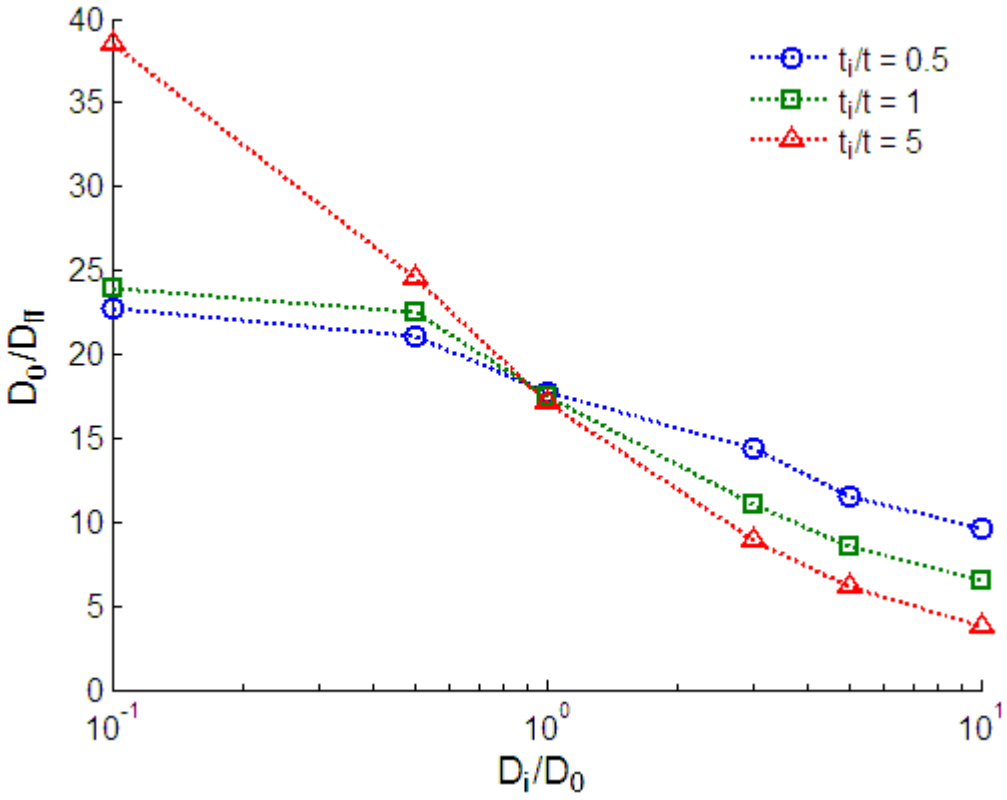

Figure 3-23, (D_0/D_{ff}) for 2-D systems with randomly distributed platelets and with an interlayer of variable diffusivity ($\alpha = 50$, $\phi = 0.10$).

Figures 3-22 and 3-23 show the effect of the presence of this interlayer as function of its intrinsic diffusivity (in the *x*-axis the ratio D_i/D_0 is reported) for the two different filler concentrations. It should be noted that when this layer between the polymer and the flake is rather impermeable ($0 < D_i < D_0$) the barrier effect is enhanced of a factor 2, at the most, with respect to the system with no interlayer; on the contrary when this third phase is quite permeable ($D_i > D_0$), the reduction of D_0/D_{ff} is more relevant, up to a factor 5.

Figure 3-24, reports the different effects of this interlayer on the barrier properties for the two filler concentrations inspected, 5 and 10%, in terms of diffusivity ratio between the flake filled system with ($D_{ff,i}$) and without (D_{ff}) considering this third phase.

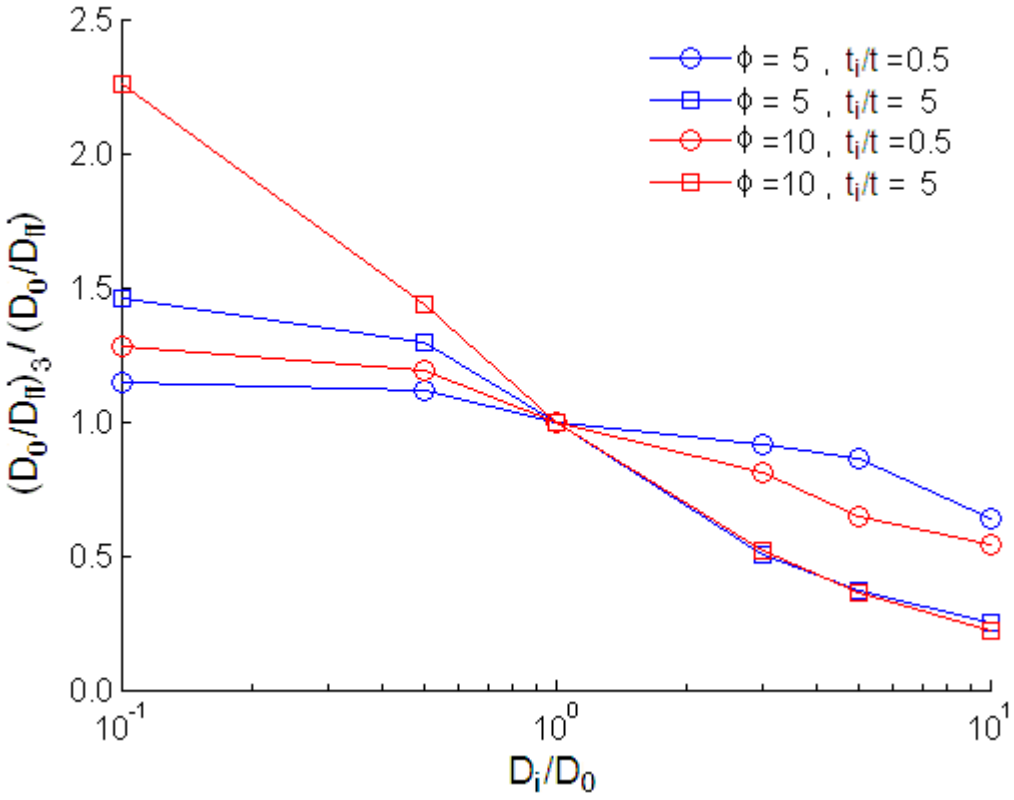

Figure 3-24, (D_0/D_{ff}) decrease due to the presence of an interlayer (labeled with 3) in 2-D systems with randomly distributed flakes with interlayer of variable diffusivity ($\alpha = 50$, $\phi = 5, 10$).

In both cases ($D_i / D_0 < 1$ and $D_i / D_0 > 1$), the system is more affected by the presence of the interlayer when is more concentrated: being the flakes close to each others indeed allow the third phase to be highly interconnected creating thus physical blocks where the permeating molecule is entrapped or easy paths where it can easily diffuse. Therefore, when a polymer layered nanocomposite is prepared, a particular care has to be focused on the adhesion between the two phases, the creation of nano-voids, indeed, promote the creation of easy paths for the diffusing species that harms the barrier effect provided by the flakes disperse in the matrix. It is also noted that it is possible to further lowers the gas diffusivity by creating a more compact structure around the flakes, but the overall effect is not remarkable; hence, this effect cannot be widely exploited in the idea of preparing ultra barrier materials, but other method should be applied.

3.4.4 3-D flake-filled systems

On the basis of the complete development of the 2-D approach, more realistic structures were then considered, distributing, in either ordered or in random way, impermeable platelets of different shapes and sizes in a three-dimensional simulation box.

3.4.4.1 3-D ordered flake-filled systems

Aspect ratios between 5 and 500, filler volume fractions, ϕ, in the range 0.005 - 0.10, and, when possible, slit shapes from 0.5 up to 10 were considered to investigate the influence of the loading on the composite transport properties. The obtained results are reported in Table 3-4.

Table 3-4, (D_0/D_{ff}) results in 3-D ordered flake filled systems with platelets of different shapes.

α	ϕ	**hexagons**		**ribbons**		**squares**		**circles**	**octagons**
		$\sigma = 0.5$	$\sigma = 5$	$\sigma = 0.5$	$\sigma = 5$	$\sigma = 0.5$	$\sigma = 5$	$\sigma = 0.5$	$\sigma = 5$
5	*0.005*	1.14	1.06	1.13	1.04	1.15	1.06	1.09	1.05
	0.0125	1.37	1.16	1.33	1.13	1.37	1.16	1.22	1.15
	0.025	1.74	1.33	1.66	1.28	1.74	1.34	1.45	1.31
10	*0.005*	1.33	1.13	1.29	1.11	1.33	1.14	1.20	1.13
	0.025	2.68	1.69	2.45	1.60	2.68	1.72	2.03	1.72
	0.05	4.39	2.52	3.94	2.33	4.43	2.67	3.12	2.71
	0.10	8.07	5.02	7.09	4.88	8.42	4.90	5.62	5.73
25	*0.05*	11.3	6.04	10.2	5.44	11.8	6.40	-	-
	0.10	24.7	15.5	21.7	14.8	26.6	13.7	-	-
50	*10*	66.4	46.7	57.2	42.7	73	36.5	-	-
100	*10*	193	152	173	141	207	107	-	-
150	*10*	384	331	339	295	387	211	-	-
200	*10*	646	574	572	502	616	341	-	-
250	*10*	936	869	880	774	886	510	-	-
300	*10*	1170	1280	1190	1100	1210	907	-	-

As previously mentioned, not all the configurations considered in this work are equivalent. In fact, while three of them, namely ribbons, squares and hexagons, perfectly packed in their elementary cell, have a slit area with constant width, in the case of octagons or circles, the hole has a further contribution because they cannot be

displaced in a perfect array. Hence, for these configurations, it was not possible to achieve small values of slit shape or high values of aspect ratio.

Figure 3-25 reports the enhancement in barrier properties in 3-D ordered systems with a slit shape value equal to 5 filled with flakes of different shapes.

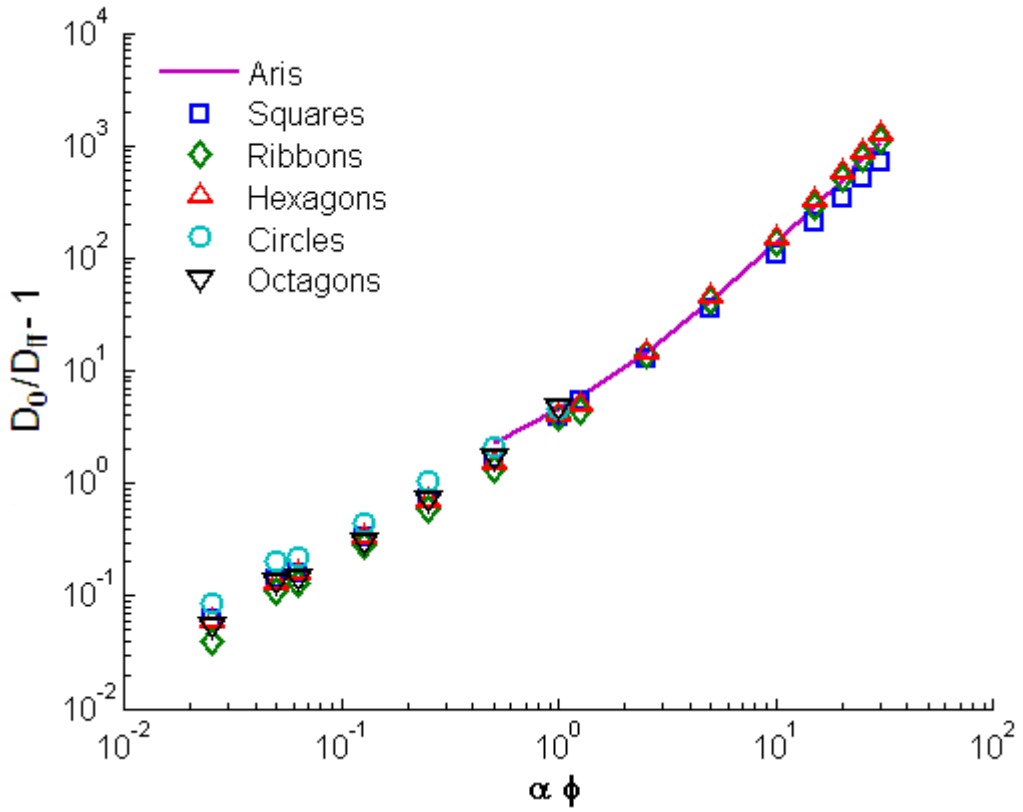

Figure 3-25, Enhancement in barrier properties (D_0/D_{ff} - 1) in 3-D flake filled systems, with platelets of different shapes (σ = 5).

In the plot, it has been also included, in its range of validity, the model due to Aris, which is proved being accurate in predicting the transport properties in 2-D nanocomposite ordered systems. The same trends have been also observed for smaller slit shapes and the results for σ = 0.5 are reported in Figure 3-26.

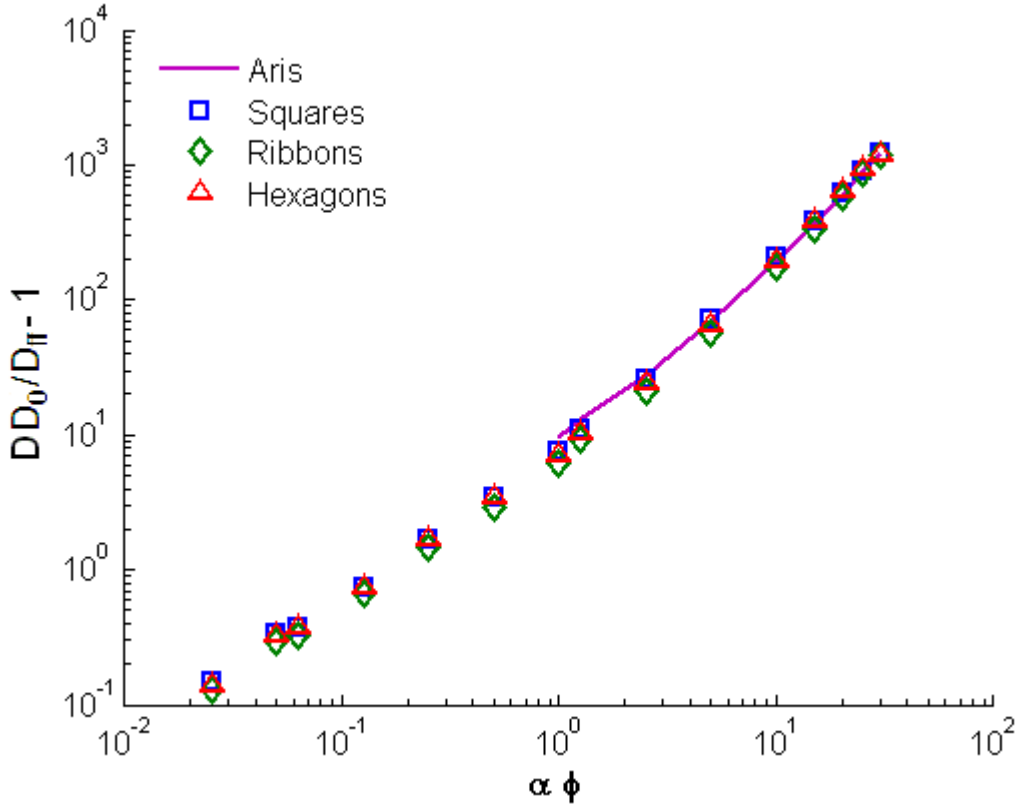

Figure 3-26, Enhancement in barrier properties (D_0/D_{ff} - 1) in 3-D flake filled systems, with platelets of different shapes (σ = 0.5).

As one can see, Figures 3-25 and 3-26 show how the different types of platelets give approximately the same barrier effect, if the geometrical parameters are calculated as above described. Therefore, the shape of the flakes does not affect the barrier properties of nanocomposite systems, which are uniquely described by the set of the three variables α, ϕ and σ.

The three-dimensional systems show the typical behavior previously observed for the case of 2-D geometries where, when $\alpha\phi$ is rather low, the trend is clearly linear with this parameter while in the rest of the range Aris equation is able to accurately predict the value of D_0/D_{ff}.

In this concern, the agreement observed with all the configurations considered and the Aris equation developed in 2-D approximation validates the new definition of the parameters aspect ratio and slit shape; this parallelism, indeed, finds the correlation between the modeling work carried out by several authors in two dimensions with more realistic structures developed with one dimension more.

It is interesting to compare the results obtained with this approach with those reported by other authors who performed numerical calculations using a Montecarlo technique such as Swannack et al. [6] or through a finite volume algorithm, such as Goodyer et al. [18]. For this purpose, several geometries were generated, following the parameters used by the authors, as described in their paper.

Figure 3-27 and 3-28 are the parity plot between enhancement in barrier properties as calculated with the present approach and the one obtained from simulations due to Swannack and Goodyer, respectively.

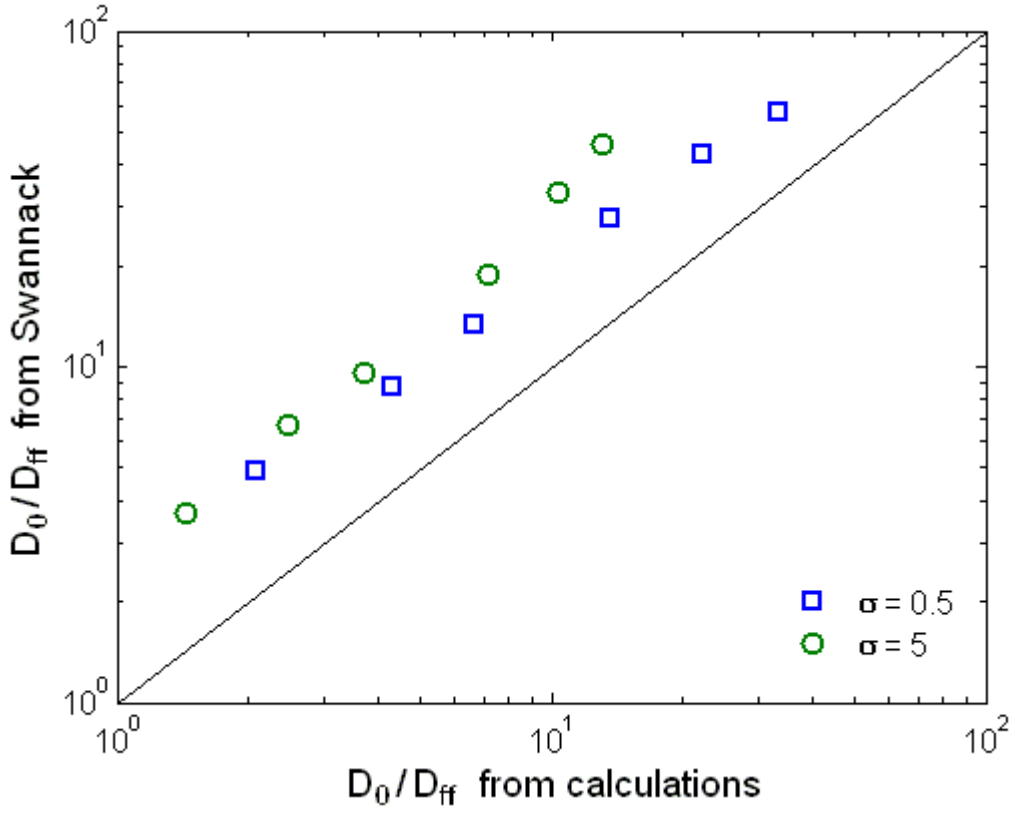

Figure 3-27, Comparison between numerical results for enhancement in gas barrier properties for 3-D ordered flake filled systems and results from the simulation performed of Swannack [6].

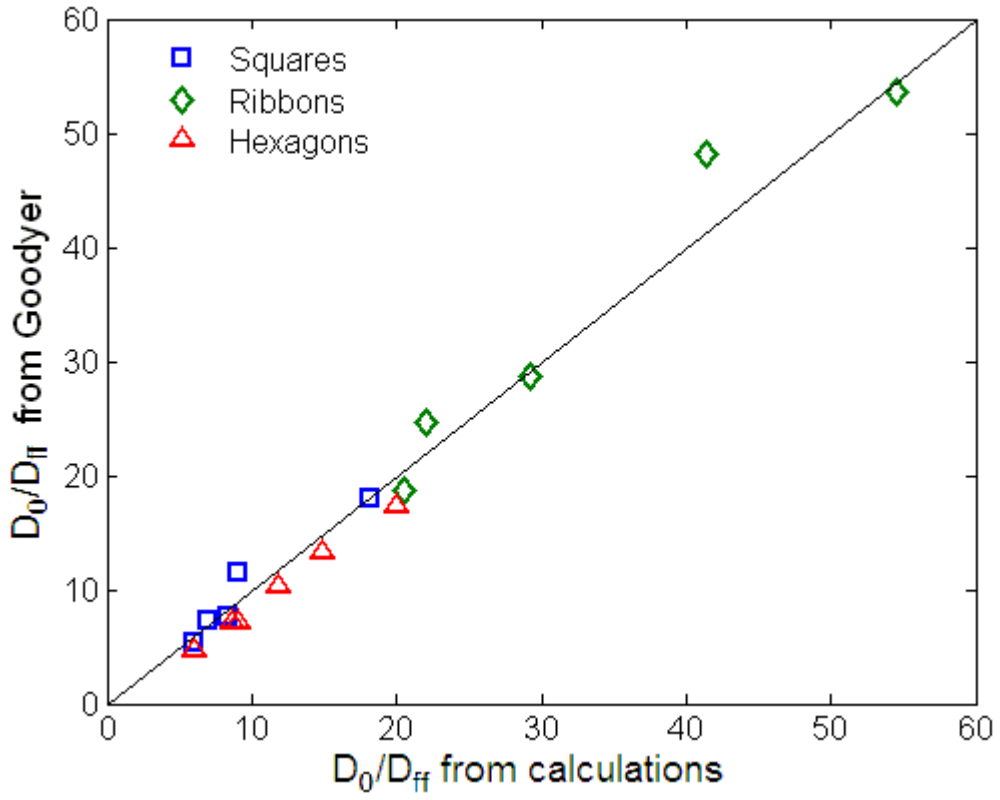

Figure 3-28, Comparison between numerical results for enhancement in gas barrier properties for 3-D ordered flake filled systems and results from the simulation performed of Goodyer [18].

As previously observed for the case of 2-D approximation, the results of the simulations due to Swannak seem to be rather different to what obtained with the present finite volume method, that are confirmed by the prediction given by the Aris equation. There is probably a lack of accuracy of these calculations performed via a Montecarlo approach, which is probably not easily suitable to solve this kind of problem.

On the contrary, finite elements method used by Goodyer, produces results very closed to the present calculations for all the three shapes considered (squares, ribbons and hexagons); the small differences that can be observed, having not a particular trend, seems to be related to numerical errors.

3.4.4.2 3-D randomly distributed flake-filled systems

Following the same approach used for the 2-D approximation, after a detailed characterization of the properties of the ordered heterogeneous systems, more realistic

structures have been developed filling the simulation box with no positional order, as previously described. In this case, only circular and squared platelets have been considered. The results, as calculated from numerical simulations are listed in Table 3-5.

Table 3-5, (D_0/D_{ff}) results in 3-D random flake filled systems with either circular or squared platelets.

α	ϕ	D_0 / D_{ff}	
		Circles	*Squares*
5	0.005	1.04	1.03
	0.0125	1.13	1.14
	0.025	1.25	1.29
10	0.025	1.53	1.56
	0.05	2.15	2.13
	0.10	3.25	3.84
25	2.5	2.29	2.11
	5	3.52	3.19
	10	5.64	6.69
37.5	0.025	2.88	3.27
	0.05	4.94	5.94
	0.10	8.02	9.11
50	0.025	3.44	3.37
	0.05	6.40	5.68
	0.10	12.2	13.0
	0.15	14.5	-

As already observed for the case of ordered structures, the shape of the platelets, evaluating the parameters α and σ according to the definition above described, has no significant influence on the overall transport properties of the nanocomposite, as showed by the parity plot in Figure 3-29, for the behaviors of (D_0/D_{ff} - 1) given by both the configurations, squares and circles.

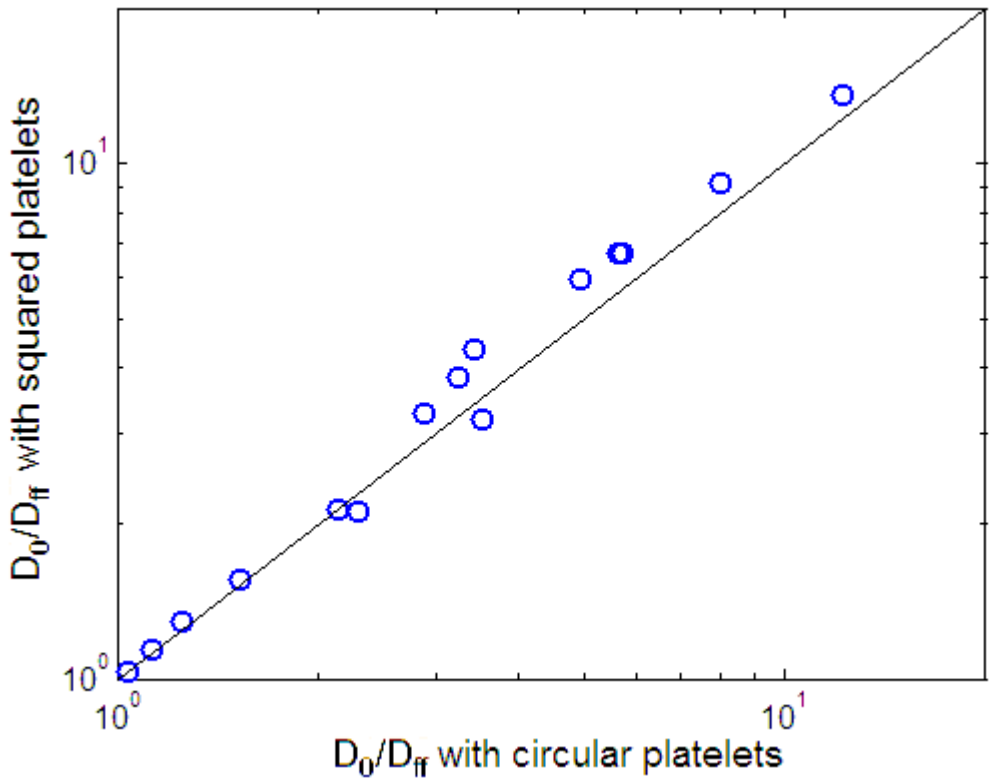

Figure 3-29, Comparison between numerical results for enhancement in barrier properties (D_0/D_{ff} -1) for 3-D random flake filled systems with different flake shape configurations, circular and squared.

As obvious, three-dimensional platelets randomly displaced in the simulation box represent the most realistic picture of polymer layered nanocomposites; it is thus of interest to compare those results with the one obtained in the 2-D approximation, as reported in Figure 3-30 which shows the enhancement in barrier properties both in 2-D and 3-D random (circular shaped) flake filled systems.

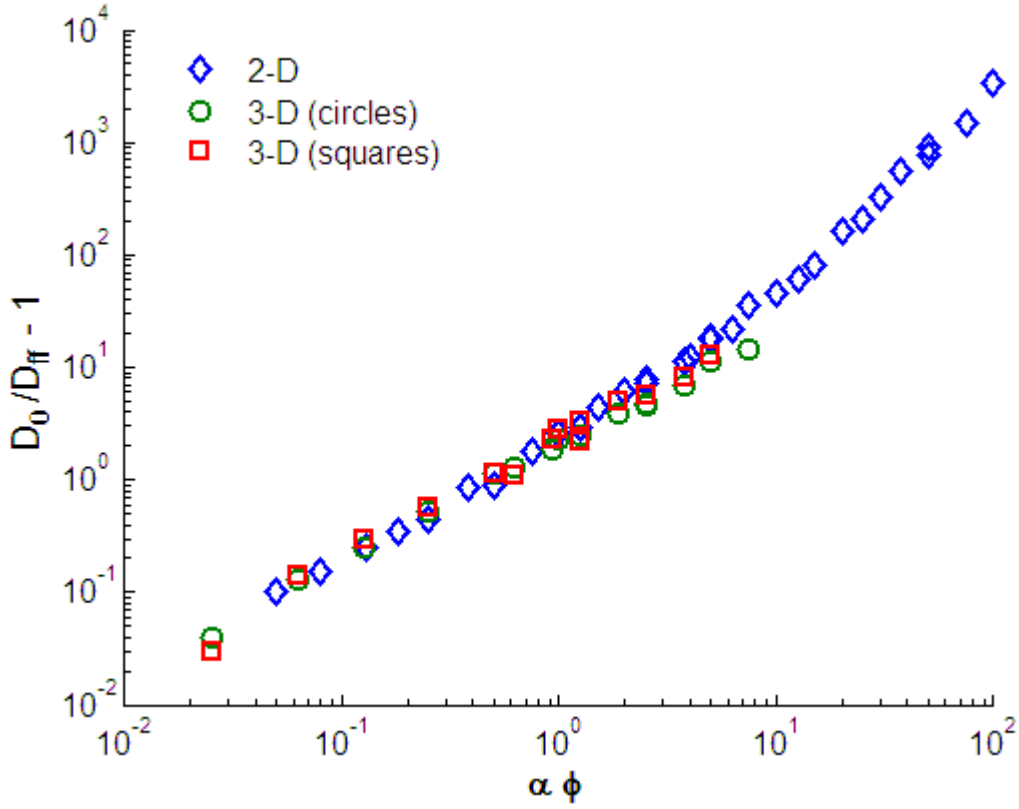

Figure 3-30, Comparison between numerical results for enhancement in barrier properties (D_0/D_{ff} -1) for 2-D and 3-D (with platelets of different shapes) random flake filled systems.

The figure shows that, when platelets are small and the system is diluted, there is a perfect agreement between the two approximations and the two curves appear almost overlapped; in this regime, as already discussed, there is not a tortuosity effect due to wiggling around the flakes and the trend of (D_0/D_{ff} - 1) is linear with $\alpha\phi$.

Unfortunately, the comparison between the two approximations cannot be performed in the entire range of $\alpha\phi$, because the simulations in 3-D are much more expensive in terms of computational power. Therefore it was not possible to properly mesh structures with flakes of very large size and high values of α could not be achieved.

3.4.4.3 Comparison with previous model predictions

In order to compare results obtained in this work for the enhancement in barrier properties for flake filled systems and those expressions developed in previous works, a series of parity plots have been built (Figures 3-31, 3-32, 3-33 and 3-34).

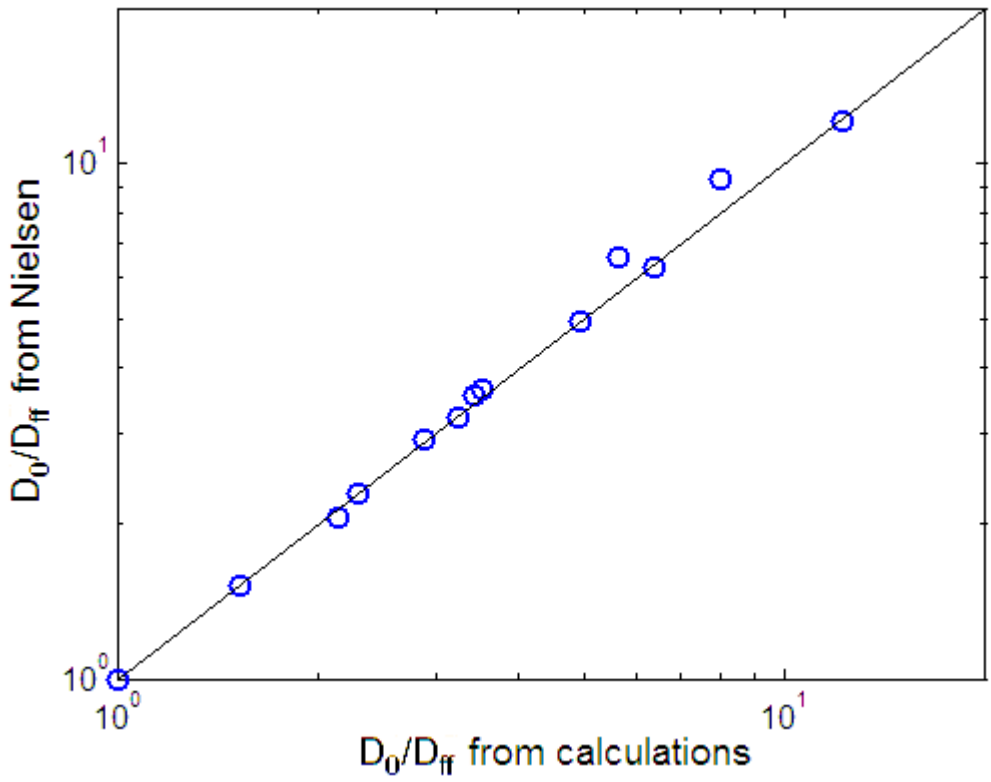

Figure 3-31, Comparison between numerical results for enhancement in gas barrier properties for 3-D random flake filled systems and prediction from Nielsen, Eq. (13).

As above described, all the models in the technical literature give a different definition of the aspect ratio α with respect to the one here considered, which is equal to the ratio normal surface to lateral surface areas, as reported in Eq. (20), while in most of the works it is given by dividing half of the main dimension of the platelets, i.e. the width, by its thickness. As obvious, the model predictions here reported were calculated according to the proper definitions given in the respective works.

Figure 3-31 shows that Nielsen's equation is able to predict the barrier effect in nanocomposite systems when rather small values of aspect ratio and loading are considered; the agreement is indeed rather precise and accurate for the whole range of parameters inspected.

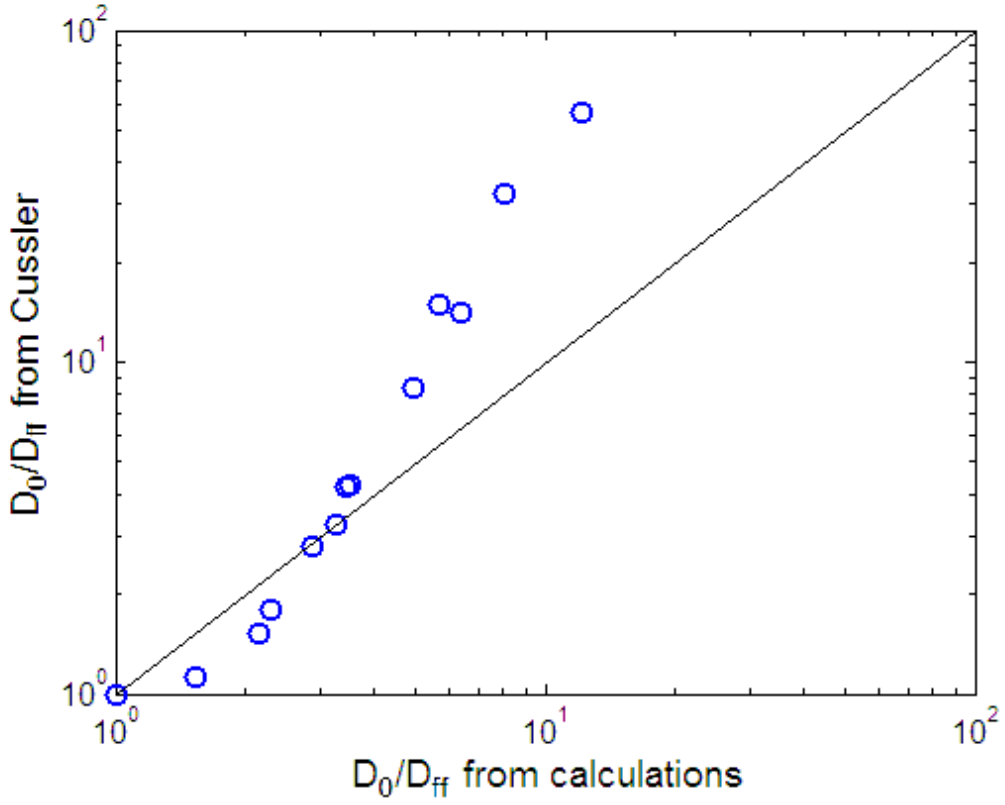

Figure 3-32, Comparison between numerical results for enhancement in gas barrier properties for 3-D random flake filled systems and prediction from Cussler, Eq. (14).

On the contrary, the model due to Cussler, which is reported in the comparison with the results obtained with numerical calculations in Figure 3-32, is not able to mimic the actual behavior of the barrier effect enhancement, even changing the adjustable parameter μ (in the figure the equation has been plotted with the value of $\mu = 0.5$ as suggested in [10]). Indeed, for small $\alpha\phi$, this equation, which supposes a quadratic behavior, underestimates the diffusivity, while, for higher values, it predicts a rather larger barrier effect with respect to the one obtained with the simulations due to an inaccurate coefficient of proportionality.

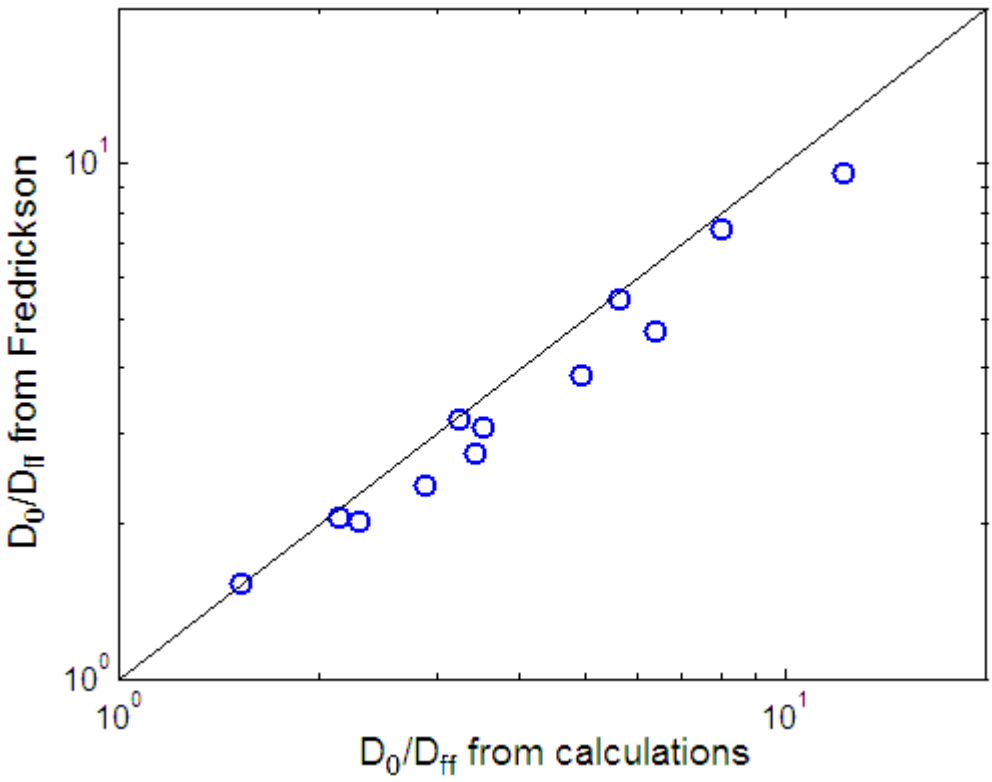

Figure 3-33, Comparison between numerical results for enhancement in gas barrier properties for 3-D random flake filled systems and prediction from Fredrickson, Eq. (15).

Figures 3-33 and 3-34 report the comparisons between the prediction of Fredrickson and Lape models, respectively. The fist one, seems to mimic quite accurately the results obtained from numerical calculation; this model indeed predict substantially a linear dependence of D_0/D_{ff} with $\alpha\phi$ as well as Nielsen.

On the contrary, the parity plot in Figure 3-34 shows that the equation due to Lape is not able to capture the enhancement in barrier properties in nanocomposite systems. However, it has to be noticed that since Lape model was able to correctly describe the behavior for the enhancement in barrier properties in the 2-D approximation, it surely can be used to approach the 3-D systems, which, as above illustrated, show the same trend and there is a perfect correspondence between the two types of geometries. In this concern, although the original development of the equation due to Lape is not correct, it should be considered as accurate once the appropriate value of α is used.

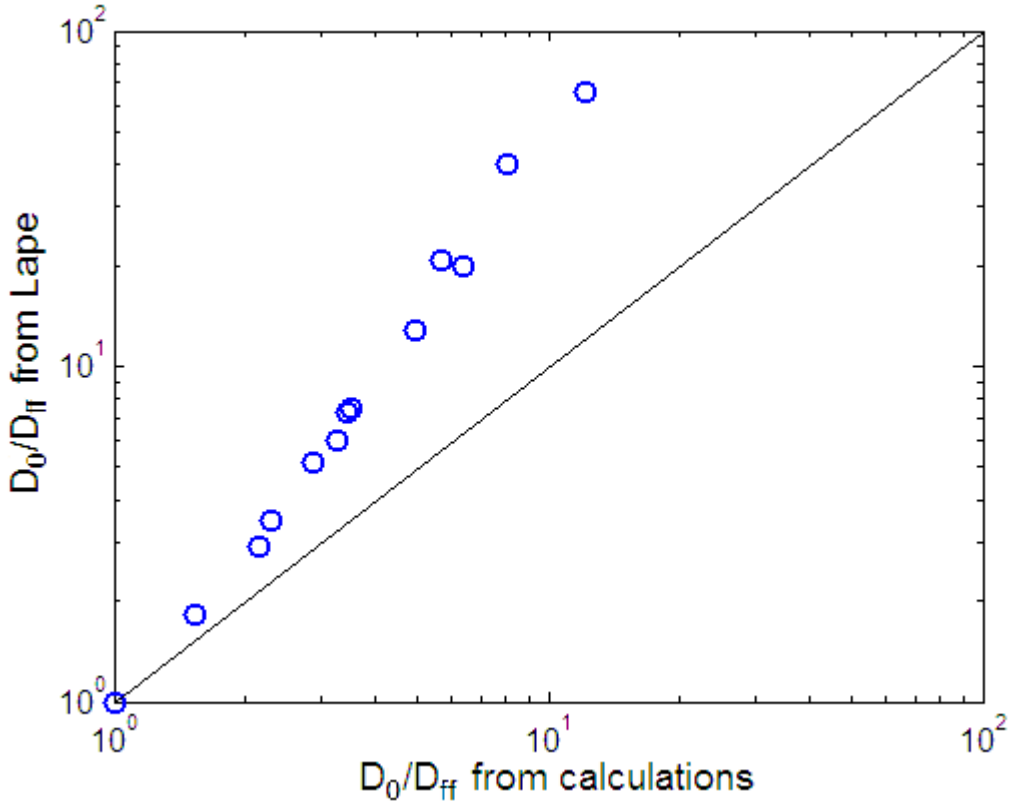

Figure 3-34, Comparison between numerical results for enhancement in gas barrier properties for 3-D random flake filled systems and prediction from Lape, Eq.(16).

The model that shows the best results is the one due to Nielsen, which is the simplest, because it is able to capture, in the investigated range of the parameters α and ϕ, a resistance to the permeation in nanocomposite material which is fairly linear with respect to $\alpha\phi$; in Figure 3-35, the results are represented as function of the filler concentration at different values of the aspect ratio and the agreement of this model with the simulations is remarkable.

It has to be noticed that this agreement is reported only for the investigated range of parameters (α up to 100 and ϕ up to 10%), while when the factor $\alpha\phi$ increases the behavior is supposed to turn as quadratic, as showed either for the case of 2-D approximation or for 3-D ordered systems. On the other hand, real nanocomposites are characterized by having rather low concentrations of inorganic phase and so, even if the flakes are quite wide (high aspect ratios), $\alpha\phi$ is always kept below 10, where the linear trend predicted by Nielsen expression has been proved to work.

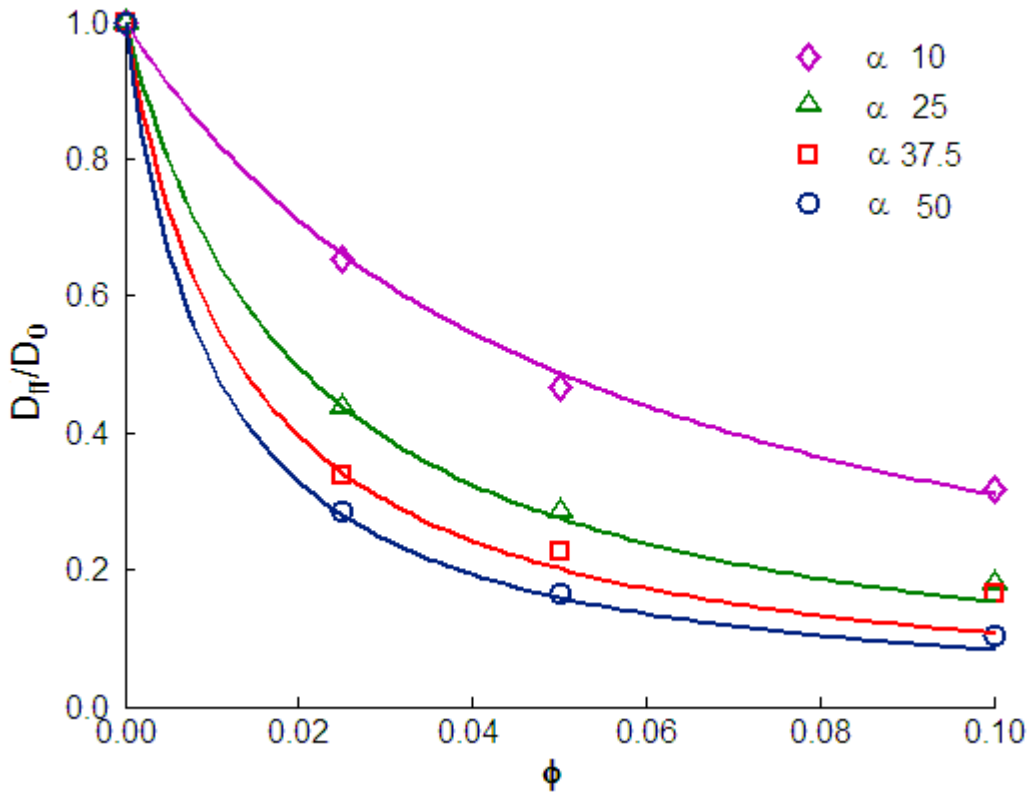

Figure 3-35, Diffusivity decrement (D_{ff}/D_0) in random structures as function of the loading ϕ for different aspect ratios, α. The solid line is the behavior predicted by the Nielsen equation, Eq. (13).

Moreover, as previously showed, the model due to Lape, which gave the correct interpretations of the results form numerical simulations, could be conveniently modified by considering α according to Eq. (20), in order to correctly predict the enhancement in barrier properties also in 3-D systems, as reported in Figure 3.36. It has to be noticed that at low values of $\alpha\,\phi$ the agreement between the results from simulations and the model prediction is remarkable, while at higher values the two curves seem to diverge; this is related to the slight deviation also present in the 2-D approximation and also due to a probable lack of accuracy for relatively high aspect ratios in 3-D systems.

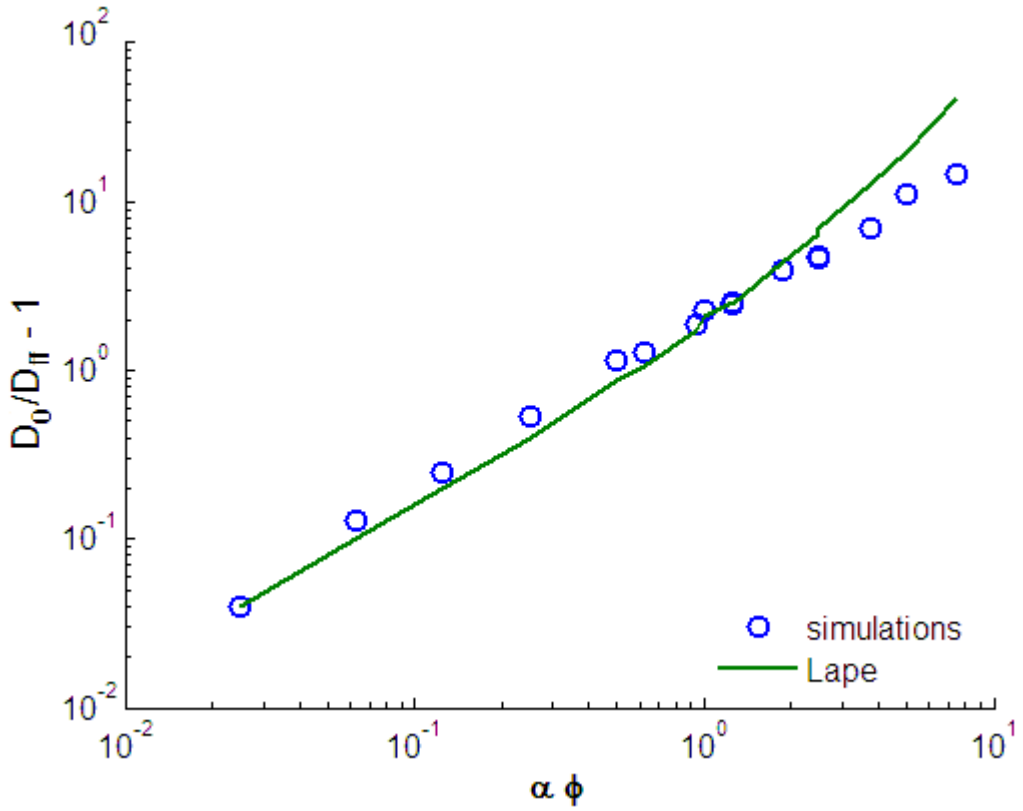

Figure 3-36, Comparison between numerical results for enhancement in barrier properties (D_0/D_{ff} -1) and prediction from a revised version of the Lape, defining the parameter α according to Eq. (21).

The effort in modeling the trend for (D_0/D_{ff} - 1), indeed, led to indentify a double behavior at low $\alpha\phi$ (linear) and at high $\alpha\phi$ (quadratic), that are clearly described in the case of ordered geometries and somewhat extended for randomly distributed systems.

3.5 Conclusions

The problem of diffusion in heterogeneous systems where an impermeable phase is dispersed in a polymer matrix has been thoroughly investigated and a simulation tool was built, based on CFD techniques, for the numerical solution of the mass transport problem in the flakes filled system and ultimately for the evaluation of decrease in overall diffusivity.

The analysis of the existing models and equations proposed in the past and reported in the technical literature led to the derivation of a new simplified expression for the enhancement of gas barrier properties in nanocomposite systems resulting from the ordered dispersion of impermeable flakes in a 2-D matrix. The expression was indeed obtained through a revision of a fundamental work by Aris for the derivation of the contribution to the resistance to mass transport due to “tortuous path” and carefully combining it with contribution for “hole” resistance.

Results from the performed calculations were in good agreement with earlier results from similar approach and predictions from the simplified model well compared with numerical solutions of the diffusion problem in the range of aspect ratio, slit shape and loading for which model assumptions hold.

Reliability of the modeling and simulation tools developed allowed for a useful discussion of different regimes in enhancement of gas barrier properties, resulting from dominance of “hole” or “tortuous path” resistance, and transition from one to another as function of the structure parameters in the system.

The case of randomly distributed systems was also considered in this 2-D approximation and the results pointed out the existence of the two different regimes characterized by two different trends for the enhancement of barrier properties as function of $\alpha\phi$, linear when the contribution of the hole resistance was predominant and quadratic for more concentrated systems with flakes of higher aspect ratios when the tortuosity of the diffusion path was the main effect achieved.

The highly packed geometries which characterized the ordered systems showed in general very good barrier effect, especially when compared with random systems. This was due to the fact that ordered disposition of the platelet maximizes the path of the diffusing molecules and prevents the presence of shortcuts inside the composite; on the other hand, in random structures such “fast tracks” were unavoidable and were used by a relevant fraction of molecules to permeate across the film.

A comparison of these results obtained from numerical simulations and the predictions with the existing models was reported and the remarkable agreement with the equation proposed by Lape, consistent with the present calculations in the entire investigated range of $\alpha\phi$, was then discussed.

In the second part, the same approach was extended in three dimensions in order to mimic more rigorously the real structures; a new definition of the parameters was then proposed to evaluate the geometrical characteristics of platelets of different shapes. In this concern, it has been showed how the overall barrier effect was not affected by the shape of the flakes and the results, in all cases, were comparable with the ones obtained in the 2-D approximation and, therefore, in good agreement with the predictions of the Aris equation. The agreement between the results obtained in approximation in 2-D and the ones in tridimensional geometries was confirmed also when randomly distributes systems were analyzed.

The comparison with the existing models showed that a new definition of the parameters was necessary in order to have a correct evaluation of the barrier properties.

The problem of the existence of a third phase between the flakes and the matrix was also approached in a random system with a given diffusivity value, in order to mimic an interlayer given by a bad adhesion between the phases or by the creation of a crystalline-like structure around the platelets. The results showed how the overall transport properties were significantly affected if a high permeable phase is considered in the structures, while the improvement in the barrier effect given by the presence of the low permeable phase was not equally remarkable.

References

[1] Aris R. On a problem in hindered diffusion. *Arch. Ration. Mech. Anal.* **18** (1986) 83-91.

[2] Cussler E.L., Hughes S.E., Ward III W.J., Aris R. Barrier membranes. *J. Membr. Sci.* **38** (1988) 161-174

[3] Falla W.R., Mulski M., Cussler E.L. Estimating diffusion through flake-filled membranes. *J. Membr. Sci.* **119** (1996) 129-138.

[4] Chen X., Papathanasiou T.D. Barrier properties of flake-filled membranes: review and Numerical Evaluation. *J. Plast. Film Sheeting* **23** (2007) 319-328.

[6] Swannack C., Cox C., Liakos A., Hirt D. A three-dimensional simulation of barrier properties of nanocomposite films. *J. Membr. Sci.* **26**3 (2005) 47-56.

[7] Wakeman W.A. Mason E.A. Diffusion through multiperforate laminae. *Ind. Eng. Chem. Fund.* **18** (1979) 301-305.

[8] Barrer R.M., Petropoulos J.H. Diffusion in heterogeneous media: lattices of parallelepipeds in a continuous phase. *Brit. J. All. Phys.* **12** (1961) 691-697.

[9] Nielsen L.E. Models for the permeability of filled polymer systems. *J. Macromol. Sci. Chem. A* **1** (1967) 929-942.

[10] Moggridge G.D., Lape N.K., Yang C., Cussler E.L. Barrier films using flakes and reactive additives. *Prog. Org. Coat.* **46** (2003) 231-240.

[11] Fredrickson G. H., Bicerano J. Barrier properties of oriented disk composites. *J. Chem. Phys.* **110** (1999) 2181-2188.

[12] Lape N.K., Nuxoll E.E., Cussler E.L. Polydisperse flakes in barrier films. *J. Membr. Sci.* **236** (2004) 29-37.

[13] Bharadwaj R.K. Modeling the barrier properties of polymer-layered silicate nanocomposites. *Macromolecules* **34** (2001) 9189-9192.

[14] Lusti R.H., Gusev A.A., Guseva O. The influence of platelets disorientation on the barrier properties of composites: a numerical study. *Model. Simul. Mater. Sci. Eng.* **12** (2004) 1201-1207.

[15] Hersteeg H.K., Malalasekera W. An introduction to computational fluid dynamics: the finite volume method, 2nd edn. Prentice Hall. Harlow (2007).

[16] Eitzman D.M., Melkote R.R., Cussler E.L. Barrier membranes with tipped impermeable flakes. *AIChE J.* **42** (1996) 2-9.

[17] Sridhar L.N., Gupta R.K., Bhardwaj M. Barrier properties of polymer nanocomposites. *Ind. Eng. Chem. Res.* **45** (2006) 8282-8289.

[18] Goodyer C.E., Bunge A.L. Numerical simulations compared against experimental results for barrier membranes with lithographically printed flakes. *J. Membr. Sci.* **306** (2007) 196-208.

[19] Ley E.E., Goodyer C.E., Bunge A.L. Mathematical models of diffusion through membranes from spatially distributed sources. *J. Membr. Sci.* **283** (2006) 399-410.

[20] Liu Q., Cussler E.L. Barrier membranes made with lithographically printed flakes, *J. Membr. Sci.* **285** (2006) 56-67.

[21] Gusev A.A., Lusti H.R. Rational design of nanocomposites for barrier applications. *Adv. Mater.* **13** (2001) 1641-1643.

[22] Guseva O., Gusev A.A. Finite element assessment of the potential of platelet-filled polymers for membrane gas separation. *J. Membr. Sci.* **325** (2008) 125-129.

[23] Nagy T.F., Duxbury P.M. Permeability and conductivity of platelet-reinforced membranes and composites. *Phys. Rev. Lett. E* **66** (2002) 020802(R).

CHAPTER IV

Modeling structure and transport properties of self-assembled monolayers

In order to investigate the temperature effect in a complex system such as *n*-alkanethiolate self-assembled monolayers on gold, with the idea of relating structural changes with the mass transport properties, a molecular simulation approach has been considered.

Molecular dynamic simulations were used to study the structure and transport properties of oxygen through the SAMs, having different overall chain length from a carbon number of 6 up to 30. This toolbar has been chosen because MD simulations have proven to be highly successful in capturing the structural properties [1-6], and in providing structural level explanations for the macroscopic properties such as wetting [2], and the barrier properties [7] of these monolayers.

MD simulations have been employed to study the transport of small molecules through different systems such as polymers [8-9], or monolayers [10]. MD simulations can provide valuable insights into the structural features that play important roles in determining the barrier properties of SAMs.

4.1 Introduction to molecular dynamics

Molecular dynamics is a technique for computing the equilibrium and transport properties of a classical many-body system, where the nuclear motion of the constituent particles obeys the laws of classical mechanics.

The idea behind molecular dynamics theory is quite simple: at first a model system has to be chosen, consisting of N particles and then Newton's equations of motion are solved for this system until the properties of the system no longer change with time, ensuring therefore the achievement of the equilibration. After the equilibration period, the actual measurements take place by monitoring specific variables during this stage (productive period) [11].

Molecular dynamics basically solves the deterministic equations of motion, i.e., Newton's second law; the problem is thus focused on solving a system of ordinary differential equations (ODEs). While there are several algorithms suitable for solving ODEs, special methods are used for MD simulation that involve a large number of equations, in order to ensure speed, accuracy (in particular energy conservation), and overcome stability. Newton's equation is used in the molecular dynamics formalism to simulate atomic motion of every atom or pseudo-atom *i* :

$$\underline{f_i} = m_i \underline{a_i} \tag{1}$$

The rate and direction of motion (velocity) are governed by the forces that the atoms or pseudo-atoms of the system exert on each other as a result of molecular interactions and that can be expressed via an appropriate force field. In practice, the atoms are assigned initial velocities that conform to the total kinetic energy of the system, which in turn, is dictated by the fixed simulation temperature. The basic ingredients of molecular dynamics are the calculation of the force on each atom $\underline{f_i}$, and from that information, the position of each atom throughout a specified period of time (typically on the order of picoseconds).

The force on an atom can be calculated from the change in energy between its current position and its position a small distance away. This can be recognized as the gradient of the energy with respect to the change in the atom's position:

$$-\underline{\nabla} V_i = \underline{f_i} \tag{2}$$

The main input to a MD code, indeed, is the force field or the potential energy surface, i.e., the interatomic or intermolecular potential describing interactions between the constituents of the molecules simulated. These potentials are developed either by fitting semi-empirical potentials to quantum mechanical methods, such as density functional theory (DFT), and/or experimental data.

Knowledge of the atomic forces and masses can then be used to solve the equations with respect to the positions of each atom along a series of extremely small time steps, to finally obtain the trajectories. Hence, an accurate integration algorithm has to be applied to solve the system of differential equations and determine the positions and velocities of each particle within the system. For this purpose, Verlet algorithm [12-13] is one of the simplest and also usually the best performing one. The derivation of this tool starts with a Taylor expansion of the coordinate of a particle, $\underline{r}$, around a generic time *t*:

$$\underline{r}(t+\Delta t) = \underline{r}(t) + \underline{v}(t)\Delta t + \frac{1}{2}\frac{\underline{f}(t)}{m}\Delta t^2 + \frac{\Delta t^3}{3!}\dddot{\underline{r}} + O\left(\Delta t^4\right) \tag{3}$$

Analogously:

$$\underline{r}(t-\Delta t) = \underline{r}(t) - \underline{v}(t)\Delta t + \frac{1}{2}\frac{\underline{f}(t)}{m}\Delta t^2 - \frac{\Delta t^3}{3!}\dddot{\underline{r}} + O\left(\Delta t^4\right) \tag{4}$$

Summing these two equations:

$$\underline{r}(t+\Delta t) + \underline{r}(t-\Delta t) = 2\underline{r}(t) + \frac{\underline{f}(t)}{m}\Delta t^2 + O\left(\Delta t^4\right) \tag{5}$$

The estimate of the new position with this method has an error that is of the order of Δt^4 where Δt is the time step in the molecular dynamics scheme. As one can see, Verlet algorithm does not use the velocity to compute the new positions, the positions at two different time-steps are required, as well as the accelerations, i.e. the force field and the mass. The velocity can be determined from the knowledge of the trajectory but this expression is only accurate to order Δt^2:

$$v(t) = \frac{r(t+\Delta t) - r(t-\Delta t)}{2\Delta t} + O\left(\Delta t^2\right) \tag{6}$$

However, the estimation of velocity is rather important for the determination of the kinetic energy of the system, so, in order to overcome this aspect, more accurate estimates of the velocities can be obtained using the velocity version of Verlet

algorithm [14]. In this scheme particle position and velocity can be determined by the following expressions:

$$r(t+\Delta t) = r(t) + v(t)\Delta t + \frac{1}{2}\frac{f(t)}{m}\Delta t + O(\Delta t^4) \quad (7)$$

$$v(t+\Delta t) = v(t) + \frac{1}{2}\frac{f(t) + f(t+\Delta t)}{m}\Delta t + O(\Delta t^4) \quad (8)$$

The new velocities, i.e. for time $t + \Delta t$ can be determined only after the new set of coordinates is computed and, consequently the new forces are evaluated; the accuracy of this method is of the order of Δt^4.

Once the system has been properly equilibrated, the macroscopic properties can be then evaluated by means of various ensemble-averaged quantities, such as self-diffusivity which is obtained from a mean-square displacement analysis of the particles trajectories, as described below [11-15].

There are several ensembles within which one can perform a MD whose choice is dictated by the desired conditions and the interests in computing costs. An example is the NVT ensemble, where the number of molecules N, the system volume V, and the temperature T are fixed. In this case, one could compute the self-diffusivity or the structure/arrangement of molecules within the simulation box; the latter provides distribution functions, such as the pair distribution function, which can be compared to experimental data.

Conventional MD can typically capture up to nanosecond time scales (microsecond or longer time scales may be possible by suitable accelerations), therefore, these time scales are sufficiently long when the system equilibrates fast, as for instance molecular liquids [15].

4.2 Simulation details

4.2.1 *n*-Alkanethiolate SAM

The molecular model developed by Hautman and Klein [1] was followed to simulate *n*-alkanethiolate ($CH_3(CH_2)_{n-1}S$) self assembled monolayers, consisting in $n + 1$ united atoms (one sulfur atom, $n - 1$ methylene groups and one methyl end-group) connected by fixed bond lengths.

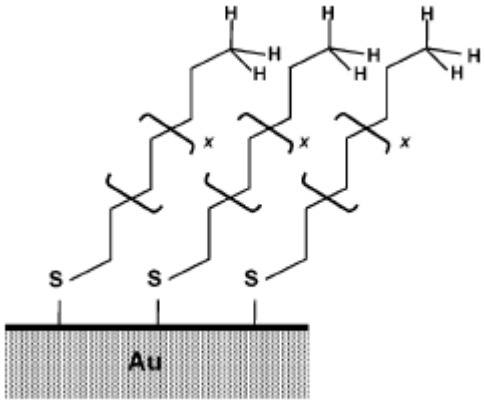

Figure 4-1, Schematic illustration of the *n*-alkanethiolate monolayer on gold.

This model was previously used to describe the system using this molecular dynamics approach [2]; the united atoms were each represented by a single interaction site. The united atoms interacted through the following 12-6 Lennard-Jones potential:

$$\begin{cases} V_{L-J}\left(r_{ij}\right) = 4\varepsilon_{ij}\left[\left(\dfrac{\sigma_{ij}}{r_{ij}}\right)^{12} - \left(\dfrac{\sigma_{ij}}{r_{ij}}\right)^{6}\right] & r_{ij} \le r_c \\ = 0 & r_{ij} > r_c \end{cases} \tag{9}$$

where r_{ij} is the distance between the segments i and j, σ_{ij} and ε_{ij} are Lennard-Jones interaction parameters and r_c is the cut-off distance. The intramolecular Lennard-Jones interaction operated only between atoms that were separated by at least three united atoms.

The Lorentz-Berthelot mixing rules, shown in the following equations, were applied in order to describe mixed interactions when particles *i* and *j* are of different types [16-17]:

$$\sigma_{ij} = \frac{1}{2}\left(\sigma_i + \sigma_j\right) \tag{10}$$

$$\varepsilon_{ij} = \sqrt{\varepsilon_i \varepsilon_j} \tag{11}$$

The parameters regarding the Lennard-Jones potential interactions for the SAMs are listed in Tables 4-1 [18].

Table 4-1, Lennard-Jones parameters for SAMs and oxygen.

	Segment	**σ (nm)**	**ε (K)**
SAMs	CH_3	0.395	98.0
	CH_2	0.395	46.0
	S	0.355	126.0
Oxygen	O_2	0.336	120.0

United atoms interacted with the underlying gold substrate through a 12-3 potential [1]:

$$V(z) = \left(\left(\frac{c_{12}}{(z - z_0)^{12}}\right) - \left(\frac{c_3}{(z - z_0)^3}\right)\right) \tag{12}$$

where c_{12} and c_3 are 12-3 interaction parameters, and z is the distance from the metal surface. The set of parameters is reported in Table 4-2.

Table 4-2, Parameters for the 12-3 Lennard-Jones potential**.**

Segment	c_{12} **(10^{-5} K nm^{12})**	c_3 **(K nm^3)**	z_0 **(nm)**
CH_3	3.41	20.8	0.0860
CH_2	2.81	17.1	0.0860
S	4.089	180.6	0.0269
O_2	2.81	17.1	0.0860

The bond-bending potential for the united atoms was described by the expression:

$$V_b(\vartheta) = \frac{1}{2} k_\vartheta \left(\vartheta - \vartheta_0\right)^2 \tag{13}$$

where k_θ is a force constant and θ_0 is an equilibrium bond angle; these parameters are listed in Table 4-3 [19].

The torsional potential was described by a series expansion in the cosine of the dihedral angle:

$$V_t(\phi) = a_0 + a_1(1+\cos(\phi)) + a_2(1+\cos(2\phi)) + a_3(1+\cos(3\phi)) \quad (14)$$

where a_0 = 0. 0 K, a_1 = 335.03 K, a_2 = -68.19 K, a_3 = 791.32 K.

Table 4-3, Valence parameters for SAMs.

Bond	**S – CH_2**	**CH_2 – CH_2**	**CH_2 – CH_3**
r_b *(nm)*	0.1812	0.1530	0.1530
Angle	**S – C – C**	**C – C – C**	
k_θ (10^3 K/rad^2)	62.5	62.5	
θ_0	114.0	109.5	

All simulations were performed in the micro-canonical ensemble NVE, and the equations of motion were integrated numerically for 200 ps utilizing the above described velocity version of the Verlet algorithm, considering a time-step of about 0.005 ps. The equilibration period for every simulation was 200 ps and, during that time, the velocities were rescaled to the desired temperature (from 200 K up to 550 K). The bond lengths in the *n*-alkanethiol molecules were constrained using the RATTLE algorithm [20]. The cut-off distance, i.e. the maximum distance at which the van der Waals interactions between beads are considered relevant and thus computed with the LJ potentials, was 5.0 σ, where σ is the segment diameter of the methylene group.

The MD cell consisted of chains arranged in the triangular lattice with a nearest neighbor spacing of 4.97Å for SAMs on gold, as reported in literature [21], and in agreement with experimental results.

The initial configurations for the chains were all trans zig-zag extended and normal to the surface. Periodic boundary conditions were used only in the *x* and *y* directions for the SAM, and no periodic boundary condition was used in the *z* direction due to the asymmetry of the system**.** The simulation cell consisted of 90 $CH_3(CH_2)_nS$ molecules and a hard wall placed above the SAM. The size of the simulation box was 11.02 σ x 11.45 σ x 11.02 σ (length (L) x width (W) x height (H))

4.2.2 Oxygen diffusion in *n*-alkanethiolate SAM

The common approach used to investigate the transport properties is based on the analysis of the trajectory of a probe molecule (oxygen) inserted within the chains and, by means of the mean-square displacement, one can obtain the diffusion coefficient. This analysis has failed in the present case due to the properties of oxygen barrier of this SAM and the characteristics of this system with no periodic boundary conditions in *z*-directions. Indeed, once the molecules was inserted into the system it was rejected due to the strong interactions with the alkanethiol chains, and the statistics in following the oxygen trajectory came out being very poor. Consequently oxygen diffusion simulations in the SAMs were carried out employing the so-called "*z*-constraint algorithm" developed by Marrink et al. [22-24], in order to obtain diffusivities, free energy barriers and resistance data for O_2 in *n*-alkanethiolate monolayers on gold.

The initial conditions were obtained by equilibrating the SAMs on gold for 200 ps. At this point the oxygen molecule was inserted and constrained at a particular *z* location in the monolayer, and allowed to move only in the *xy*-plane for another 200 ps using a constraining force $F(z,t)$ to keep the desired *z* coordinate. This procedure was repeated in 23 slabs corresponding to 23 different *z* positions chosen to sample the whole monolayer. The oxygen molecule was represented by a single LJ site [25] and its parameters are listed in Table 3-3.

The time average of the constraining force, $\langle F(z)\rangle_t$ was used to calculate the local free energy barrier, $\Delta G(z)$ at the particular *z*-position. To compute the free energy barrier $\Delta G(z)$ as a function of the *z* position, the constraining force $\langle F(z)\rangle_t$ was averaged over time in each slab:

$$\Delta G(z) = -\int_{outside}^{z} \langle F(z')\rangle_t dz' \qquad (15)$$

Furthermore, the diffusion coefficient in the *z*-direction, $D(z)$, was calculated using the fluctuation-dissipation theorem [26]; the autocorrelation function, $\langle \Delta F(z,t).\Delta F(z,0)\rangle$ of the time fluctuations of the instantaneous constraining force, $\Delta F(z,t)$ was used to calculate the time dependent local friction coefficient, $\xi(z,t)$.

$$\xi(z,t) = \frac{< \Delta F(z,t) \Delta F(z,0) >}{RT} \Delta F(z,t) \tag{16}$$

Integrating $\xi(z,t)$ over time the local static friction coefficient is determined:

$$\xi(z) = \int_0^\infty \xi(z,t) = \frac{\int_0^\infty < \Delta F(z,t) \Delta F(z,0) > dt}{RT} \tag{17}$$

The local diffusivity in the *z*-direction, D_z, was calculated using Einstein's relation:

$$D(z) = \frac{RT}{\xi(z)} = \frac{(RT)^2}{\int_0^\infty < \Delta F(z,t) \Delta F(z,0) > dt} \tag{18}$$

The diffusivity in the *xy*-plane, D_{xy}, was obtained by a mean square displacement approach following the trajectories of the oxygen molecule:

$$D_{xy}(z) = \lim_{t \to \infty} \frac{< (r(t) - r(0))^2 >}{4t} \tag{19}$$

The overall resistance to permeation, *R*, was obtained by considering the local free energy barrier, $\Delta G(z)$ and the local diffusivity value in the *z*-direction, $D_z(z)$, and by integrating over the whole monolayer:

$$R = \int_{outside}^{z} \frac{\exp\left(\frac{\Delta G(z')}{RT}\right)}{D(z')} dz' \tag{20}$$

4.3 Results

Molecular simulation techniques were applied to investigate the temperature effect on SAMs on gold; equilibrium structures were analyzed to obtain structural information, such as gauche population, as well as the average and the local density for these monolayers, in order to relate them to the transport properties in terms of diffusivity and mass transport resistance.

Molecular dynamics simulations were carried out from very low temperature, 200 K, at which SAMs of every chain length are supposed to be perfect crystals, up to 550 K, to fully understand their entire behavior.

4.3.1 Analysis of trans/gauche populations

In a monolayer, the gauche population density is indicative of its crystallinity: a monolayer having a low gauche population density is considered well ordered or crystalline.

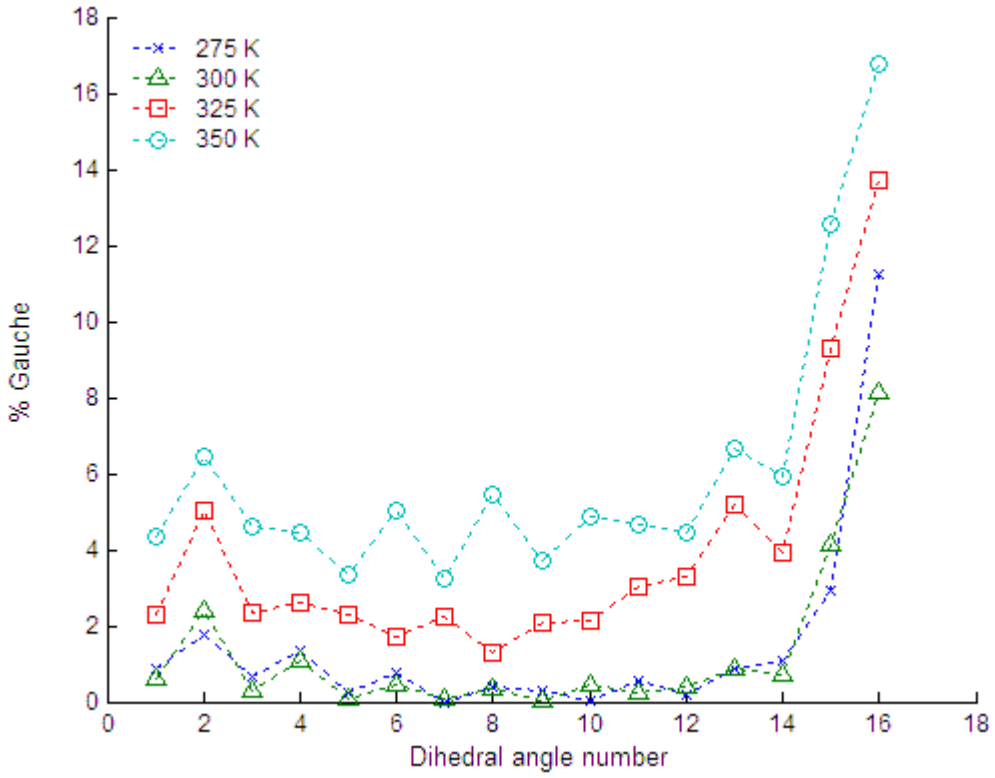

Figure 4-2, Gauche percentage profiles for *n*-octadecanethiolate SAM on gold as obtained from equilibrium MD simulations at various temperatures.

Figure 4-2 shows gauche profiles for a *n*-alkanethiolate SAMs of chain length n = 18 at four different temperatures, where the dihedral angle ϕ was considered as a gauche conformer if $cos\,\phi \geq 0.5$. The profiles show the gauche population is concentrated in the end-groups (on the right side of the plot, while the angle 0 corresponds to the metallic slab) for monolayers of every chain length at every temperature, due to the fact they are free to move and to change their conformation. This is in good agreement with previous works. Furthermore, the population of gauche defects is slightly higher in the area next to the metal surface (the head-group) than in the core;

this effect is more evident in monolayers of long chain molecules and almost negligible in the short *n*-alkanethiolate SAMs.

Below 300 K, gauche defects are located only in the end-groups and the fraction of gauche conformers in the middle part is no more than 1-2 %. As the temperature is raised up to approximately 325-350 K, the average gauche population starts to increase, the chain ends become highly disordered and defects develop in the middle portion as well. Further increases in temperature cause the middle portion of the monolayer to become progressively less crystalline.

Another analysis of the gauche population is performed in order to get a measure of the temperature at which the whole monolayer is no longer crystalline. In other words, the structure is disordered enough to be considered liquid-like; therefore, it is as a sort of melting temperature. The entire monolayer will be labeled as melted when the gauche population of every dihedral angle is above a certain value of cut-off.

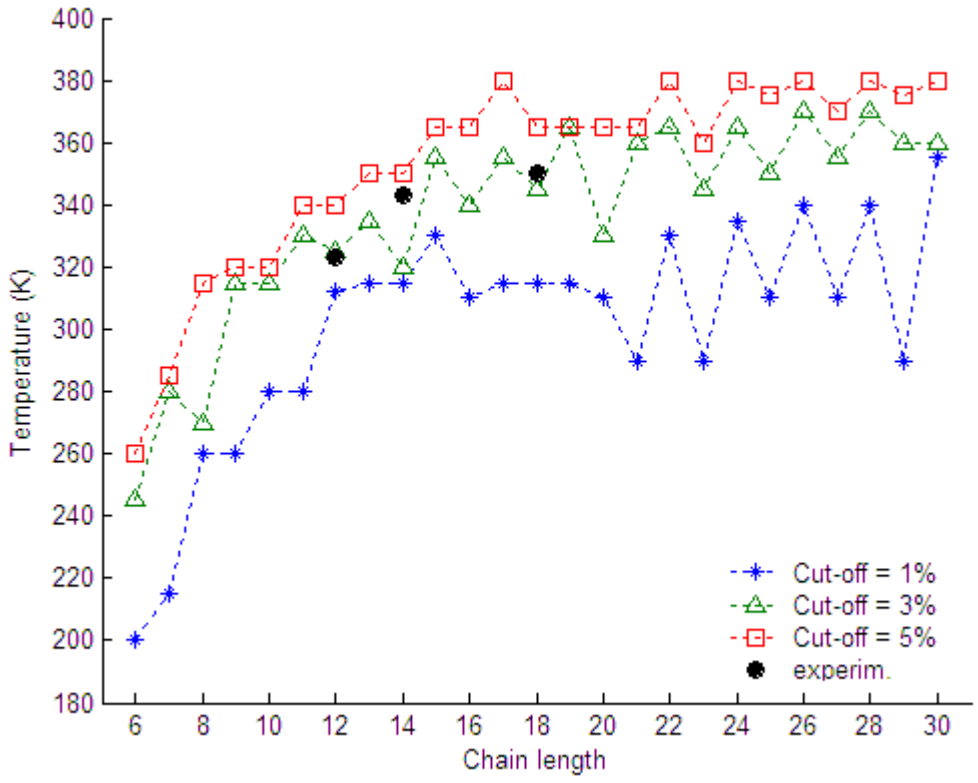

Figure 4-3, Global phase transition temperature profiles for various *n*-alkanethiolate SAMs on gold as a function of their chain length *n*. Data obtained from equilibrium MD simulations using different cut-off values for the gauche density of the whole monolayer; experimental points obtained from Ref. [27].

In Figure 4-3 these pseudo phase transition temperatures are shown as functions of the chain length, considering different percentages of gauche population as cut-off. Clearly the gauche population cutoff has no effect on the overall shape of the curve. However, the cutoff value of 3 % seems to be in good agreement with experimental phase transition temperatures obtained with XRD and RAIRS measurements carried out by Venkataramanan et al. [27]. This trend can be divided in two different regions. In short chain monolayers, the transition point increases steeply with the chain length. Enhancing further the size of the molecule, the curve reaches a sort of plateau, where the local phase transition temperature slightly increases. In the first region (short chain) the monolayer tends to be highly disordered even at room temperature, but for long chain monolayers higher temperature is required to make the system liquid-like.

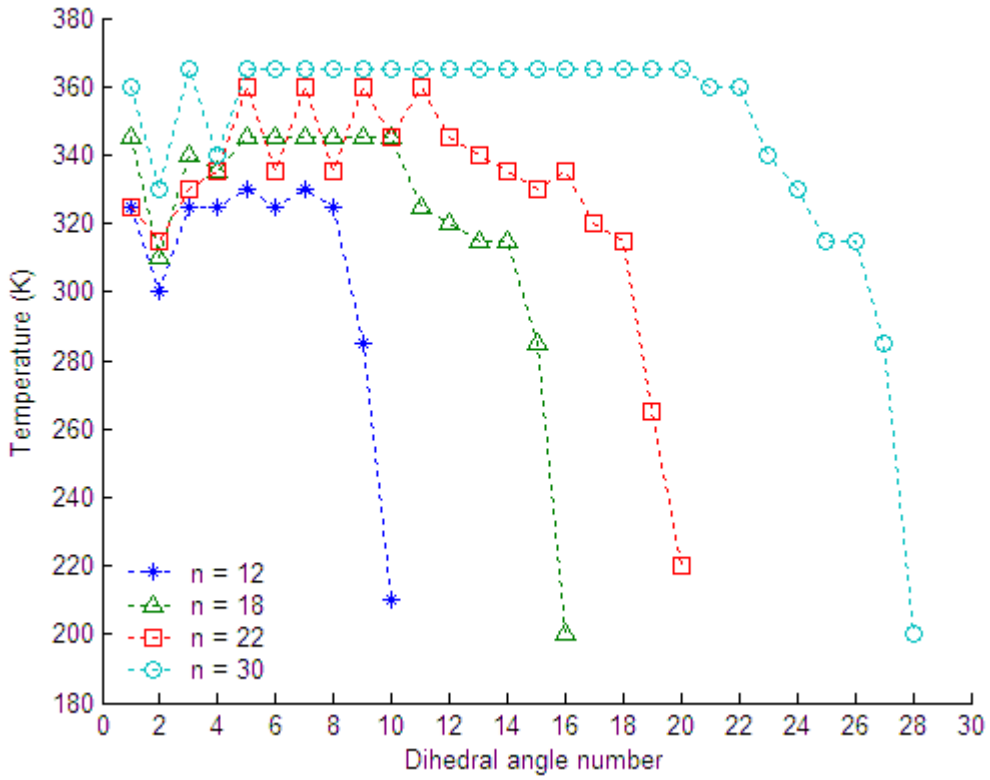

Figure 4-4, Local transition temperature profiles for *n*-alkanethiolate SAMs on gold with various chain lengths *n*. Results were obtained from equilibrium MD simulations using a cut-off value of 3 % in the local gauche density.

An analogous analysis is performed inside the chain to draw the local transition temperature profiles to understand how the monolayer becomes disordered once the

temperature is increased; the profiles shown in Figure 4-4 are obtained considering 3 % gauche as a cut-off value.

These profiles are really similar for *n*-alkanethiolate SAMs of different chain lengths and all of them show a wide area of constant temperature and a deep drop in correspondence to the end of the chain. The end-groups are disordered at very low temperatures and there is a middle portion where the structural changes occur at the same temperature. It is also appreciated that the head-group becomes disordered at lower temperature.

The existence of three distinct regions in the monolayer previously mentioned appears very clear in the four plots in Figure 4-5; that show the average ratios gauche/trans for the three different parts.

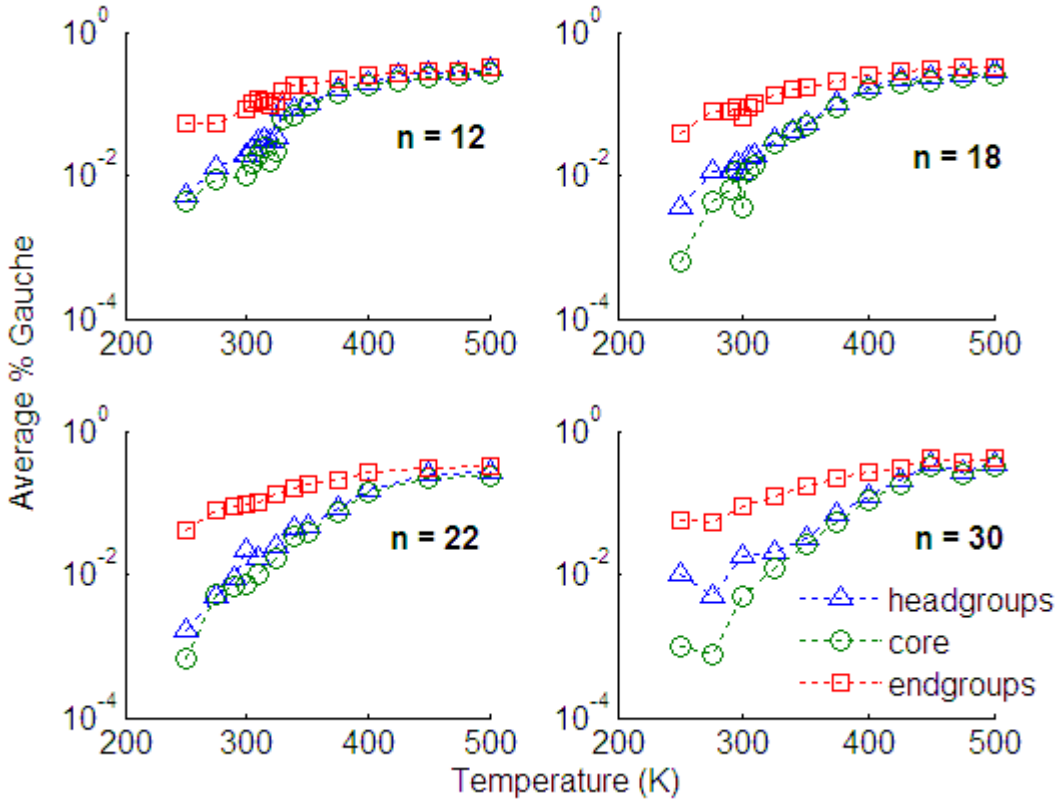

Figure 4-5, Average gauche populations in the head-group, core, and end-group regions within various *n*-alkanethiolate SAMs on gold as a function of temperature as obtained from equilibrium MD simulations.

As one can see, they show three completely different behaviors and, the temperature differ even by one order of magnitude (the *y*-axis has a logarithmic scale): this effect becomes more relevant with increasing chain length.

4.3.2 Temperature effect on the monolayer density

The temperature increase affects the monolayer also in terms of global density, as shown in Figure 4-6, where density profiles are reported as function of the chain length at 3 different temperatures. The density value was obtained as a time average of the mean thickness of the monolayer at 80 different snapshots (only the thickness was changeable, because periodic boundary conditions were set in the other 2 directions).

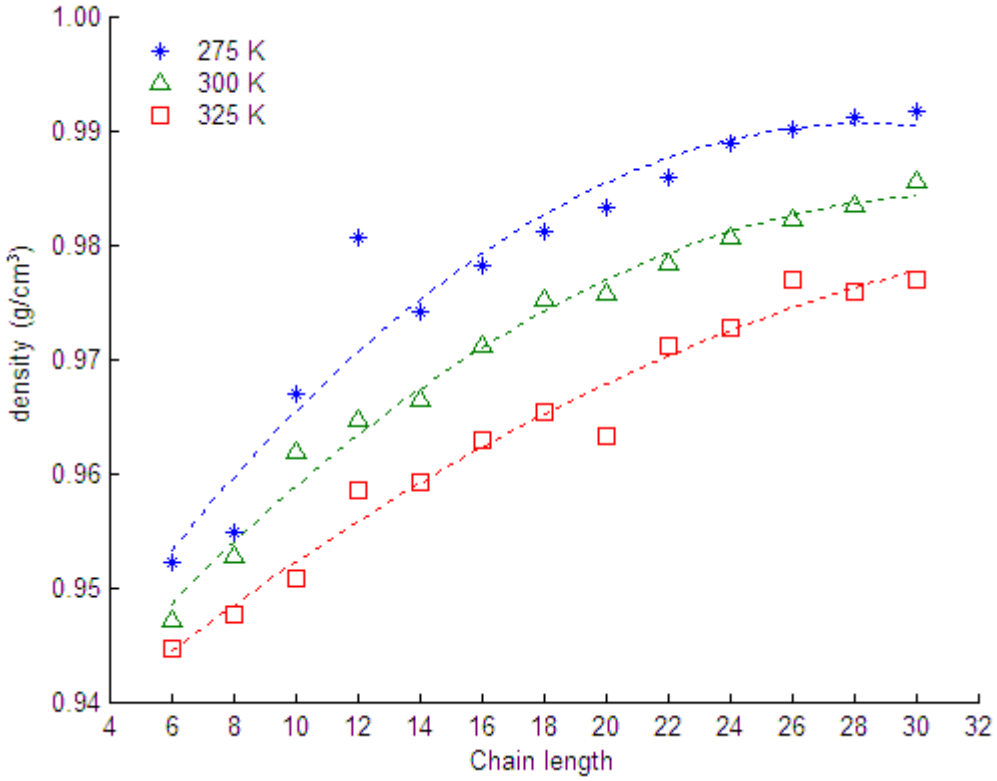

Figure 4-6, Density of *n*-alkanethiolate SAMs on gold with various chain lengths (*n*) at three different temperatures as calculated from MD simulations.

The molecular dynamics simulations show that the monolayer is packed at high density (up to about 1 g/cm^3 at room temperature), which is comparable with the ones of crystalline polyethylene and polypropylene (approximately 0.95 g/ cm^3) and fairly higher than bulk *n*-alkanethiols and *n*-alkanes.

Although the density slightly changes (about 4-5 %), the profiles show that there exists a unique trend at every temperature: the monolayer becomes more compact and

packed with increasing the chain length. On the other hand, the overall density decreases with increasing temperature due to the fact that the chains are becoming more disordered and more extended in the *z*-direction.

In fact, in order to explain why the temperature rise makes the monolayer less dense, the average molecular tilt angle, calculated from the orientation of the molecular axis with respect to the surface normal, has to be considered. In Figure 4-7 tilt angles are reported as a function of the temperature for monolayers of different chain lengths, and the circles are simulation data of *n*-hexadecanethiolate SAMs obtained by Hautman and Klein [3].

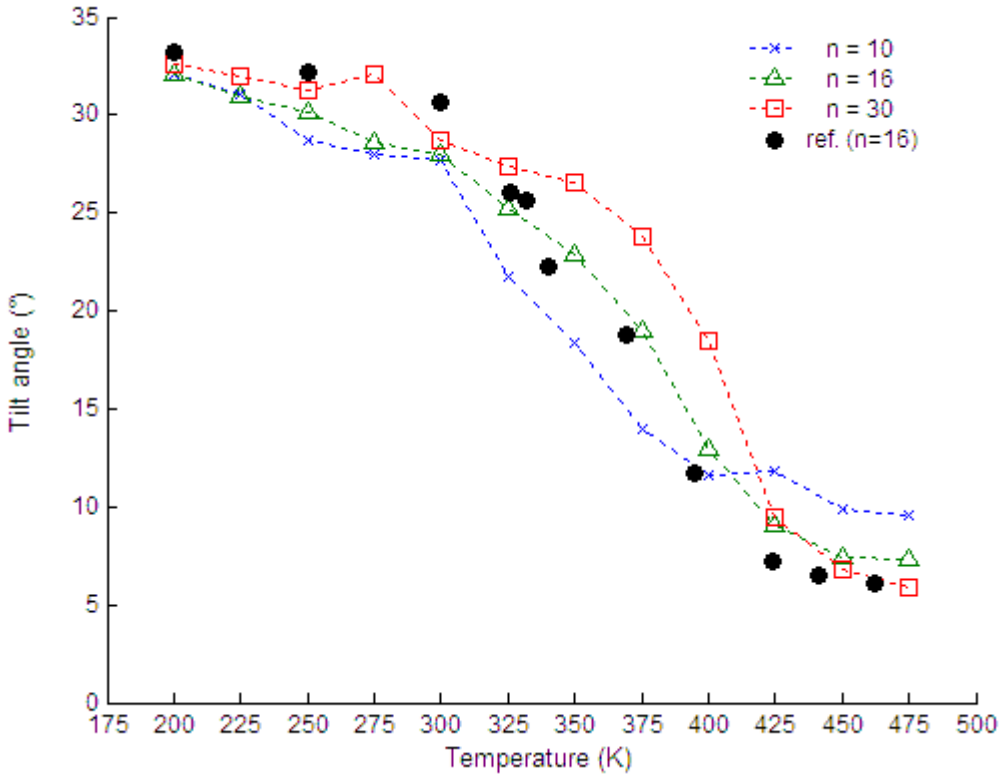

Figure 4-7, Effect of temperature on the average chain orientation for three different *n*-alkanethiolate SAMs on gold as obtained from the equilibrium MD simulations. Simulation data for *n*-hexadecanethiolate SAM from Hautman and Klein are included for comparison [3].

At low temperature the tilt angle maintains roughly the initial value of about 30-32° for *n*-hexadecanethiolate (but it changes with increasing number of carbons) up to approximately the room temperature. Above 300 K there is a clear drop that is associated with the phase transition previously mentioned, indeed it occurs at higher temperatures increasing the chain length, in good agreement with the phase transition

temperatures profile shown in Figure 4-2. As the temperature is further increased, the tilt angle seems to asymptotically decrease to a constant value related to the chain length. However, at high temperature, the structure of the monolayer is mostly disordered and the gauche population percentage is fairly high, so the tilt angle calculation has no meaning anymore because the chain cannot be considered linear.

More detailed information about the local structural changes are shown in the local density profiles where all the atoms in the monolayer are reported; they are a measure of local free volume of the monolayer and so directly related to the transport properties.

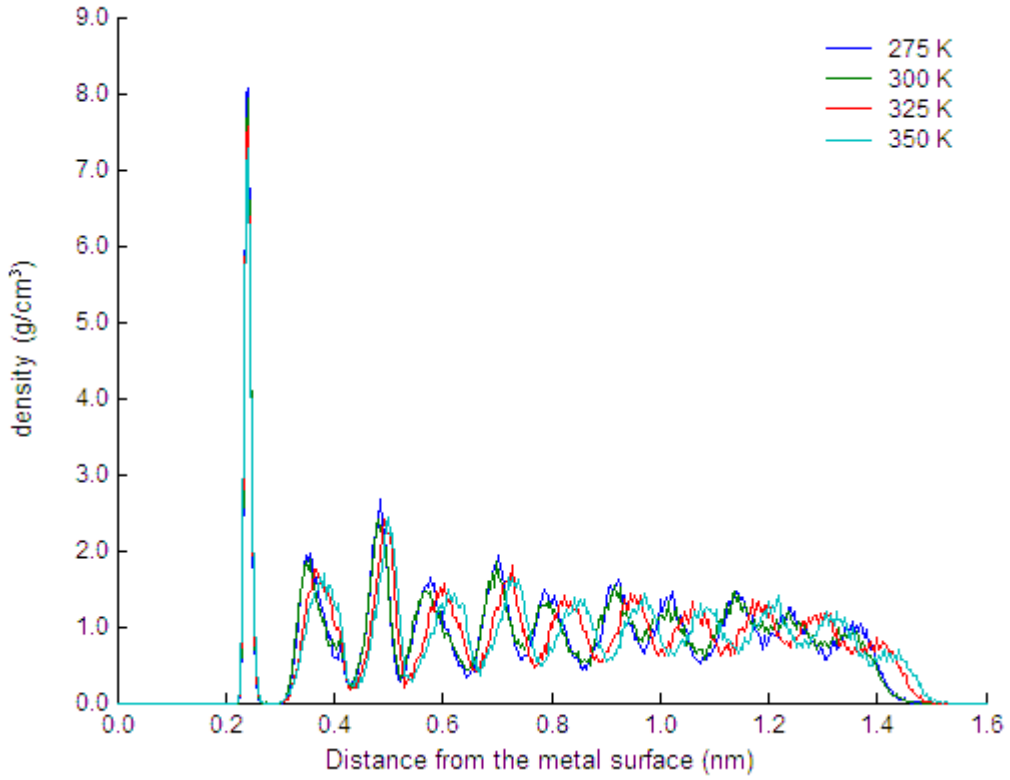

Figure 4-8, Local profile of the density normal to the surface of *n*-decanethiolate SAM on gold obtained from the equilibrium MD simulations at four different temperatures.

In Figures 4-8 and 4-9, two local density profiles normal to the metal surface for *n*-alkanethiolate SAMs of two different chain lengths (n = 10, n = 18) are plotted. As one can see, below room temperature, the sharp and well defined peeks and drops show a high degree of positional order, in good agreement with low density of gauche defects. As the temperature is increased above 300 K, the amplitude of the oscillation becomes shorter, the structure is more liquid-like in the area near the interface with

the vacuum; however, in most of the cases, the profiles show that there still exists a crystalline phase next to the metal surface.

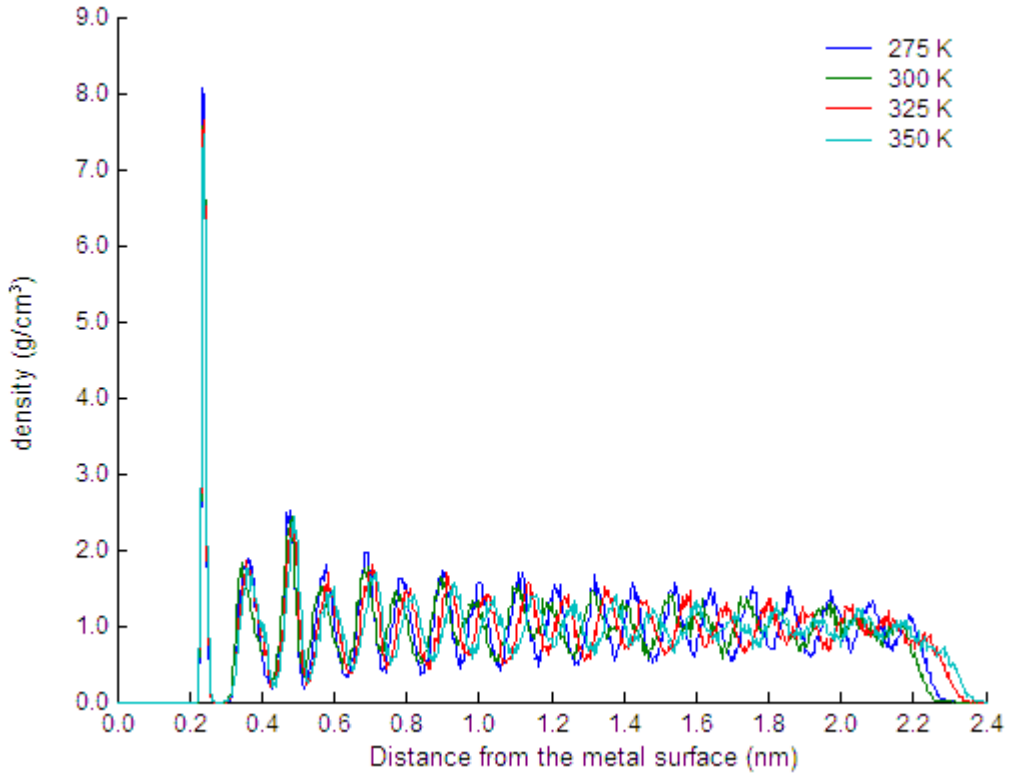

Figure 4-9, Local profile of the density normal to the surface of *n*-octadecanethiolate SAM on gold obtained from the equilibrium MD simulations at four different temperatures.

Furthermore, as the temperature is increased above room temperature, the structure starts to expand, the peaks corresponding to the methyl groups shift more distant to the surface, indeed the thickness increases due to the decrease in the tilt angle, i.e. the chains tend to be almost normal to the gold surface, as previously shown in the overall density profiles and in the tilt angle plot.

4.3.3 Temperature effect on the transport properties

MD simulations were performed to get quantitative information regarding the transport properties of oxygen in *n*-alkanethiols SAMs on gold of different chain lengths (n = 10, 18, 30); the diffusion coefficient through the monolayer is obtained

using the *z*-constraint algorithm, and the diffusion coefficient in the *xy*-plane is determined by calculating the mean square displacement.

In Figure 4-10 the diffusivities in the *z*-direction are reported as a function of the temperature, and as one can see, there is a slight difference between the three chain lengths and the trend with temperature is not monotonic.

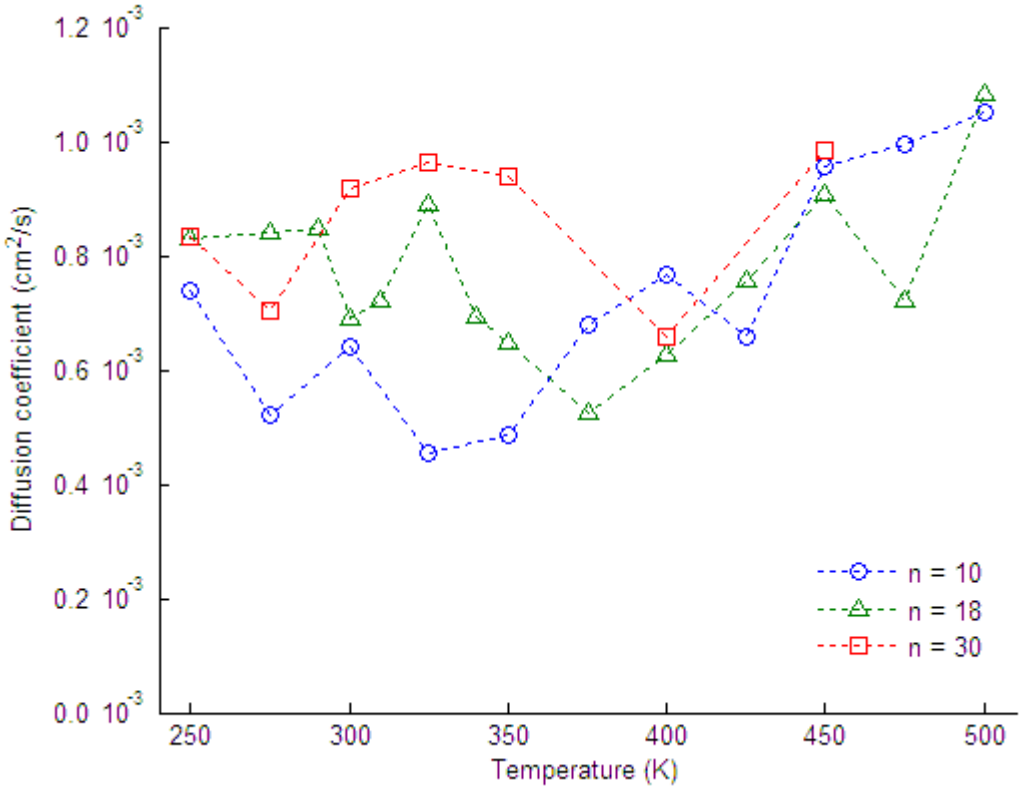

Figure 4-10, Diffusion coefficients in the *z*-direction for the transport of oxygen through various *n*-alkanethiolate SAMs on gold, as calculated from MD simulations.

It has to be noticed that, raising the temperature two competing effects are involved: at first the kinetic contribution of the penetrant molecule tends to increase the diffusion coefficient, on the contrary the change in structure makes the monolayer less crystalline and therefore, becoming more disordered, it looses its preferential orientation in the *z* direction.

The *xy* diffusion coefficient, which has been reported in Figure 4-11, appears clearer than the one in the *z*-direction and the scattering of the data is small.

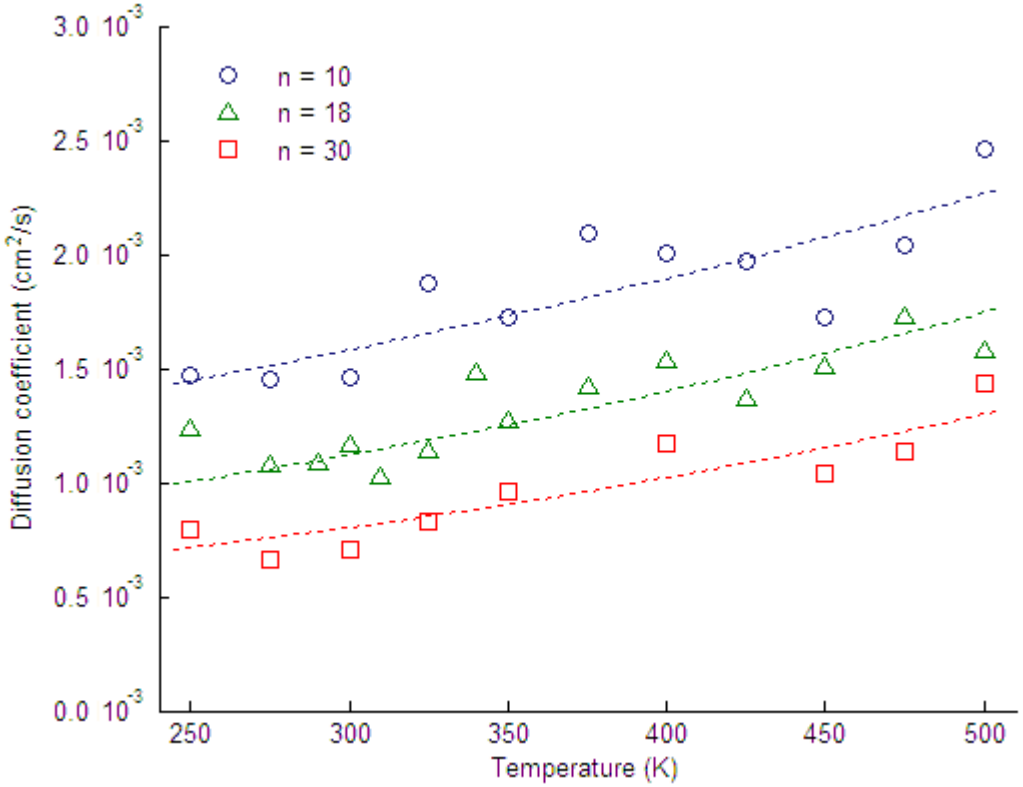

Figure 4-11, Diffusion coefficients in the *xy*-plane for the transport of oxygen through various *n*-alkanethiolate SAMs on gold, as calculated from MD simulations.

As one can see, in this case the three plots, corresponding to the different chain lengths, are different, because the oxygen can diffuse faster in the monolayer with shorter chain. The temperature trend is unique and it is the same in all the *n*-alkanethiolate SAMs of different chain lengths, and can be fitted by an exponential behavior.

Even if there are no remarkable changes of the *z*-direction diffusion with temperature, the free energy profiles show a clear influence on T, as reported in Figure 4-12 for a *n*-triacontanethiolate SAM (*n* = 30) on gold. The free energy barrier offered by the monolayer decreases from ~ 20 kJ/mol to ~ 17 kJ/mol when the temperature is increased from 250 K to 300 K and it drops to a value of ~ 12 kJ/mol for T = 350 K.

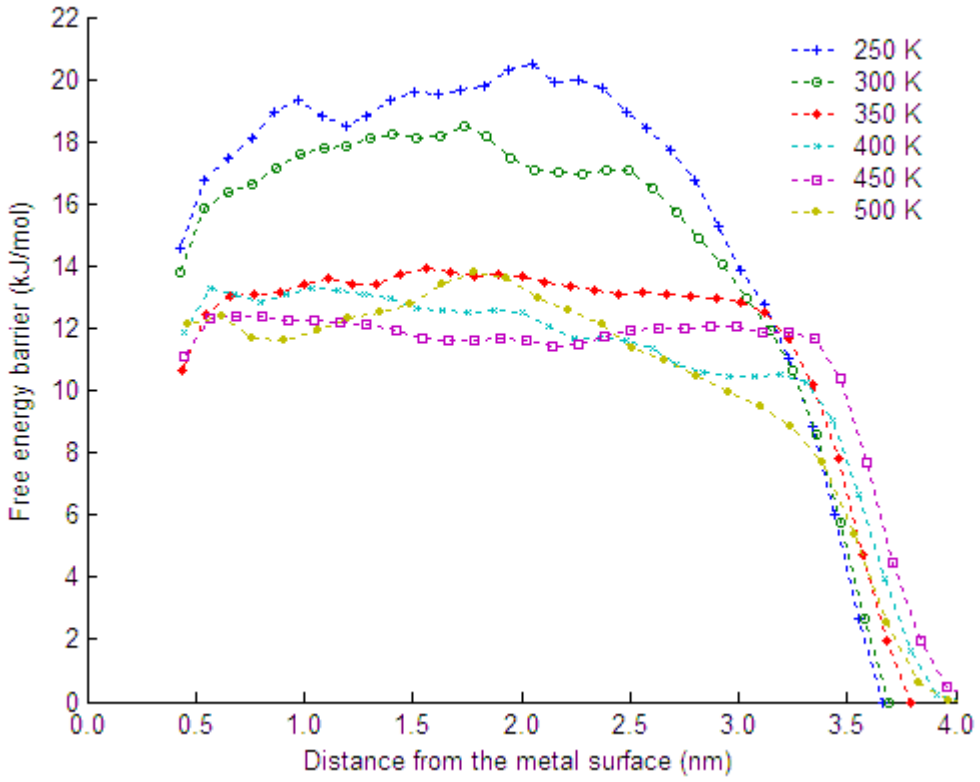

Figure 4-12, Free energy barrier profiles for the transport of oxygen through an *n*-triacontanethiolate SAM (*n* = 30) on gold at different temperatures, as calculated from MD simulations

This is related to the structural changes, which occur in this temperature range, as previously discussed: the monolayer turns in to a less ordered configuration characterized by a higher fraction of free volume accessible to the penetrant.

Further increase in temperature does not affect significantly the free barrier profiles, so the curves appear almost all overlapped; this is due to the local phase transition, which occurs at 360 K in a SAM of chain length 30 and above this temperature the monolayer is considered completely as liquid-like.

Considering all these features, the overall resistances offered by *n*-alkanethiolate SAMs on gold towards oxygen transport, are strongly dependent on the temperature, as shown in Figure 4-13, and they drop by 2 or 3 orders of magnitude in the investigated range of temperature, in a sort of exponential decay.

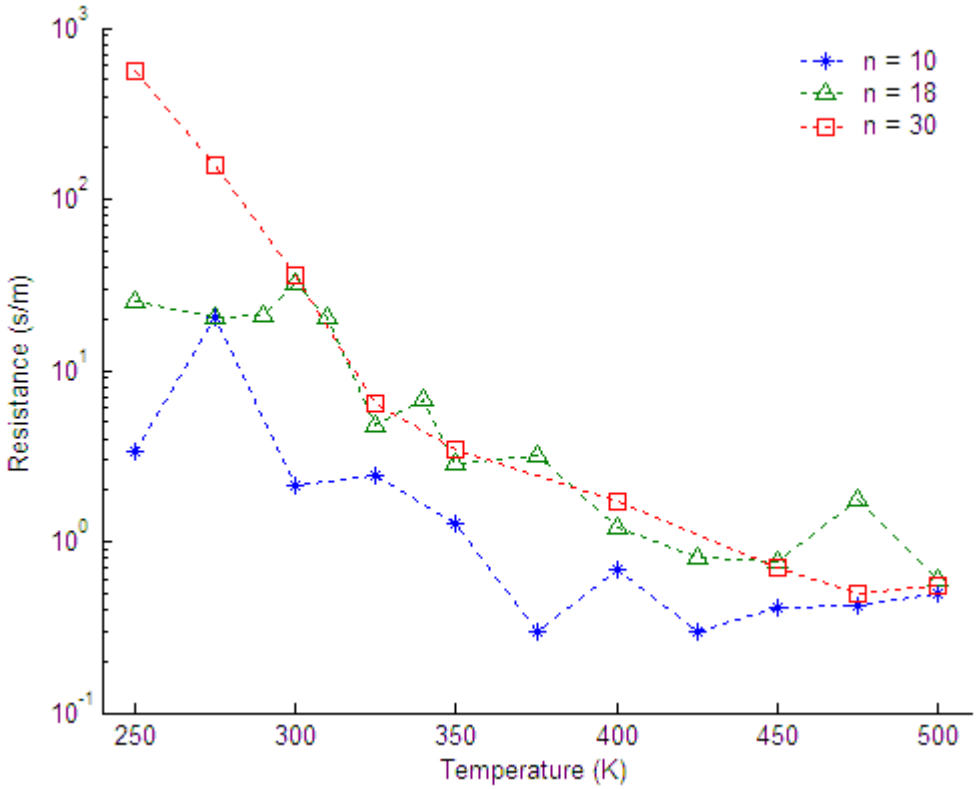

Figure 4-13, Overall resistance to permeation for the transport of oxygen through *n*-alkanethiolate SAMs of chain lengths 10, 18 and 30 on gold as calculated from MD simulations.

The effect of temperature on the structure, and consequently on the free energy barrier, is enhanced by rescaling ΔG by the factor RT as previously reported in Eq. (20). Furthermore, the comparison of the three curves shows that the monolayers offer almost the same resistance to the oxygen diffusion if n = 18 or n = 30, the behavior of R in *n*-decanetiolate is below the others. The short chain monolayers present a poor resistance to the oxygen due to their structure, which is disordered even at low temperature.

4.4 Conclusions

MD simulations were performed to investigate the effect of the temperature on oxygen transport through *n*-alkanethiolate SAMs on gold of different chain lengths.

MD simulations showed that the diffusivities, free energy barriers and resistances for these monolayers are strongly affected by the temperature.

The structural information obtained from the equilibrium MD simulations of these coatings revealed that the crystallinity, compactness, and the thickness of the SAMs are the most important factors responsible for the observed barrier property trends. It has been shown indeed that the primary effect of raising the temperature is to make the monolayer more disordered and consequently less crystalline.

The analysis of the SAMs crystallinity by the evaluation of the chains gauche populations allowed the calculation of an effective transition temperature at which the structure becomes liquid-like. Increasing the temperature, the defects develop from the external part to the middle region of the monolayer, and, at high enough T, the whole core of the SAM changes its structure.

In this concern, tilt angle and both average and local densities were determined form MD simulations showing that the structure of the monolayer tended to become more expanded and less dense once the temperature is raised, exhibiting also a good agreement with previous simulations data.

This disorder induced a reduction of the resistance to the through-film oxygen diffusion, as determined from MD simulations that showed the diffusivities, free energy barriers and resistances were strongly affected by the structural changes given by raising the temperature.

References:

[1] Hautman J., Klein M.L. Simulation of a monolayer of alkyl thiol chains. *J. Chem. Phys.* **91** (1989) 4994-5001.

[2] Srivastava P., Chapman W.G., Laibinis P.E. Odd-even variations in the wettability of *n*-alkanethiolate monolayers on gold by water and hexadecane: a molecular dynamics simulation study. *Langmuir* **21** (2005) 12171-12178.

[3] Hautman J., Klein M.L. Molecular dynamics simulation of the effects of temperature on a dense monolayer of long-chain molecules. *J. Chem. Phys.* **93** (1990) 7483-7492.

[4] Hautman J., Bareman J.P., Mar W., Klein M.L. Molecular dynamics investigations of self-assembled monolayers *J. Chem. Soc. Farad. Trans.* **87** (1991) 2031-2037.

[5] Bareman J.P., Cardini G., Klein M.L. Characterization of structural and dynamical behavior in monolayers of long-chain molecules using molecular-dynamics calculations. *Phys. Rev. Lett.* **60** (1988) 2152-2155.

[6] Bareman J.P., Klein M.L. Collective tilt behavior in dense, substrate-supported monolayers of long-chain molecules: a molecular dynamics study. *J. Phys. Chem.* **94** (1990) 5202-5205.

[7] Srivastava P., Chapman W.G., Laibinis P.E. *J. Phys. Chem. B,* Submitted.

[8] Dekker M. Diffusion in Polymers; 1st edn. New York (1996).

[9] Indrakanti A., Ramesh N., Duda J.L., Kumar S.K. Modeling diffusion in miscible polymer blend films. *J. Chem. Phys.* **121** (2004) 546-553.

[10] McKinnon S.J., Whitterburg S.L., Brooks B. Nonequilibrium molecular dynamics simulation of oxygen diffusion through hexadecane monolayers with varying concentrations of cholesterol. *J. Phys. Chem.* **96** (1992) 10497-10506.

[11] Allen M.P., Tildesley D.J. Computer simulation of liquids. Oxford Science Publications. Oxford (1989).

[12] Verlet L. Computer "Experiments" on Classical Fluids. I. Thermodynamical properties of Lennard-Jones molecules. *Phys. Rev.* **159** (1967) 98-103.

[13] Verlet L. Computer "experiments" on classical fluids. II. Equilibrium correlation functions. *Phys. Rev.* **165** (1967) 201-214.

[14] Swope W.C., Andersen H.C., Berens P.H., Wilson K.R. A computer simulation method for the calculation of equilibrium constants for the formation of physical clusters of molecules: application to small water clusters. *J. Chem. Phys.* **76** (1982) 637-649.

[15] Frenkel D., Smit B. Understanding molecular simulation: from algorithms to applications. Academic Press. New York (1996).

[16] Jorgenson W.L. Intermolecular potential functions and Monte Carlo simulations for liquid sulfur compounds. *J. Phys. Chem.* **90** (1986) 6379-6388.

[17] Jorgenson W.L., Tirado-Rives J. The OPLS [optimized potentials for liquid simulations] potential functions for proteins, energy minimizations for crystals of cyclic peptides and crambin. *J. Am. Chem. Soc.* **110** (1988) 1657-1666.

[18] Stubbs J.M., Potoff J.J.; Siepmann J.I. Transferable Potentials for Phase Equilibria. 6. United-Atom Description for Ethers, Glycols, Ketones, and Aldehydes. *J. Phys. Chem. B* **108** (2004) 17596-17605.

[19] van der Ploeg P., Berendsen H.J.C. Molecular dynamics simulation of a bilayer membrane. J. Chem. Phys. **76** (1982) 3271-3276.

[20] Andersen H.C. Rattle: A “velocity” version of the shake algorithm for molecular dynamics calculations. *J. Comp. Phys.* **52** (1983) 24-34.

[21] Laibinis P.E. Whitesides G.M., Allara D.L., Tao Y.T., Parikh A.N., Nuzzo R.G. Comparison of the structures and wetting properties of self-assembled monolayers of n-alkanethiols on the coinage metal surfaces, copper, silver, and gold. *J. Am. Chem. Soc.* **113** (1991) 7152-7167.

[22] Marrink S.J., Berendsen H.J.C. Simulation of water transport through a lipid membrane. *J. Phys. Chem.* **98** (1994) 4155-4168.

[23] Marrink S.J., Sok R.M., Berendsen H.J.C. Free volume properties of a simulated lipid membrane. *J. Chem. Phys.* **104** (1996) 9090-9099.

[24] Marrink, S. J.; Berendsen, H.J.C. Permeation process of small molecules across lipid membranes studied by molecular dynamics simulations. *J. Phys. Chem.* **100** (1996) 16729-16738.

[25] Murad S., Gupta S. Molecular dynamics simulation for Henry's constant of oxygen in benzene. *Fluid Phase Equil.* **187** (2001) 29-37.

[26] Kubo R. The fluctuation-dissipation theorem. *Rep. Prog. Phys.* **29** (1966) 255-284.

[27] Venkataramanan M., Pradeep T. A method to study the phase transition and desorption of self-assembled monolayers on planar gold surfaces. *Anal. Chem.* **72** (2000) 5852-5856.

CHAPTER V

Conclusions

In this work the problem of diffusion of small molecules in nano-sized systems has been widely investigated from different points of view. This new class of materials, indeed, recently developed by means of several techniques, presents a structure with a constituting element in the nanoscale. This gives interesting properties to the system and makes the materials suitable for several potential applications. The transport phenomena here studied, and specifically the barrier effect given by these systems, allow a straightforward application in the food packaging industry.

The first part of this work was focused on the experimental results achieved in two types of material, organic-inorganic hybrid coatings (obtained via sol-gel) and microfibrillated cellulose films.

The second section was dedicated to two different approaches of simulation: the diffusion of oxygen through polymer-layered silicates was modeled from a continuum scale with a CFD software, while the properties of *n*-alkanthiolate self assembled monolayers on gold were analyzed from a molecular point of view by means of a molecular dynamics algorithm.

Concerning the experimental activity, the transport properties, in terms of oxygen permeability, diffusivity and solubility, of two different sets of organic-inorganic hybrids have been investigated. It has been proved that the sol-gel technique is suitable for the preparation of materials with remarkable barrier properties obtaining composites where the organic (polymeric) domains are highly interconnected with the silica Si-SiO_2 at the nano-scale, leading thus to an improvement of the barrier properties.

When a fairly permeable polymer, such as a polyethylene-based material, is used as organic phase, it has been showed that the barrier performances were rather improved.

The analysis of the hybrid oxygen permeabilities indeed revealed a strong decrease of its values when the silica is added, much larger of what predicted by the Maxwell model: this indicates that there is a further effect given by the structure of the system where the two moieties are highly interconnected. This feature was enhanced by the addition of a low permeable material, PHS, able to promote hydrogen bonds, that allowed to obtain a system suitable for the food packaging applications.

Another set of materials was developed considering as organic phase polyvinyl alcohol, that has exceptional oxygen barrier properties; in this case the addition of silica was aimed at the stabilization of PVOH with respect to water, which is a strong solvent of the polymer. Hence, permeation tests were performed on samples as received and pretreated by dipping the specimen into water, and water vapor sorption experiments were also carried out. The results showed that the addition of silica, and the consequent formation of an interconnected network in the sol-gel process, is able to guarantee stability of the polymer structure and barrier properties even after a prolonged exposition of the sample to water.

Regarding micro-fibrillated cellulose, MFC, two different generations, obtained by two different processes, have been characterized in terms of oxygen and water transport properties. The system showed a remarkable barrier effect toward oxygen when it is dry, while, as expected for such hydrophilic materials, the permeability strongly increases increasing the water content in the membrane. A particular attention was also devoted to the water sorption and permeation; the trends of water permeability, diffusivity and solubility as function of the activity were discussed on the basis of structural considerations regarding the two different generations, with or without plasticizer. The very low value of water diffusivity reported at low activities, has been discussed in relationship with structural observations. Therefore, the remarkable properties of this material that have been reported make MFC interesting for several potential applications exploiting its significant sustainability and biodegradability, as well as good mechanical properties, in the field of bio-nanocomposites, either as pure film or as reinforcement for bio-polymers.

Concerning the second section, at first the modeling the transport properties in layered nanocomposite systems has been developed by means of a CFD software based on a finite element algorithm, that allowed the calculation of the barrier effect in relation

with the structural parameters of the platelets dispersed in the polymeric phase. The existing models were also analyzed leading to the derivation of a new expression for the enhancement of gas barrier properties in nanocomposite systems resulting from the ordered dispersion of impermeable flakes in a 2-D matrix; the equation was obtained through the revision of a fundamental work by Aris pointing out the contribution to the resistance to mass transport due to “tortuous path” and carefully combining it with contribution for “hole” resistance. The simulation results showed the good agreement with the prediction given by this model when the geometrical parameters are in the range in which model assumptions hold.

The case of randomly distributed systems was also considered in this 2-D approximation and the results pointed out two contributions to the overall effect, as predicted by the model and observed for ordered structures. There are indeed two regimes characterized by two trends for the enhancement of barrier properties as function of $\alpha\phi$, a linear one when the contribution of the hole resistance is predominant (small $\alpha\phi$) and a quadratic one for more concentrated systems with flakes of higher aspect ratios (large $\alpha\phi$) when the tortuosity of the diffusion path is the main effect achieved. On the contrary the random distribution of the flakes reduces the barrier effect that can be obtained with respect to ordered structure, because the presence of holes inside the composite, sort of shortcuts, is unavoidable and a relevant fraction of molecules uses these easy paths to permeate across the film. The results were analyzed in comparison with the models existing in literature for such systems and it has been showed the equation proposed by Lape well predicts the enhancement in barrier properties in the entire investigated range of α and ϕ.

The same approach was then extended in three dimensions to mimic real structures and a new definition of the parameters was thus developed to calculate the geometrical characteristics of platelets of different shapes. It has been showed, in this concern, that the transport properties were not affected by the shape of the single flakes, and, in all cases, results were comparable with the ones obtained in the 2-D approximation and, therefore, in good agreement with the predictions given by Aris equation.

Three-dimensional systems with randomly distributed platelets were finally simulated and the results revealed that are in good agreement with the ones obtained in the 2-D approximation.

A completely different approach was then considered to simulate the effect of the temperature on the oxygen transport through *n*-alkanethiolate SAMs on gold of different chain lengths; due to its particular structure, such material had to be modeled at the molecular level and a molecular dynamics code was thus developed.

The structural information obtained from equilibrium MD simulations showed the gauche population profiles within the monolayer that provide the measure of crystallinity; the chain tilt angle, and local and overall densities were also determined. It has been showed that adding energy to the system, i.e. raising the temperature, makes the monolayer more disordered and consequently less crystalline. This effect was considered to determine an effective transition temperature at which the structure becomes liquid-like on the basis of the analysis of gauche populations; the results showed a good agreement with experimental data and suggested the mechanism of these modifications providing also quantitative information. The gauche defects, at low temperature located only in the chain-ends, develop from the external part toward the middle region the monolayer, and when the transition temperature is reached (it depends on the chain length), the entire monolayer turns into a liquid-like configuration.

MD simulations showed also, concerning the oxygen transport properties, that diffusivities, free energy barriers and resistances for these monolayers are strongly affected by these structural changes. The disorder given by the high temperature indeed produces a decrease in the barrier free energy and it lowers the overall resistance to oxygen diffusion, making the monolayer thus more permeable to small molecules.

The complete work carried out on different materials and approached by several methods, either experimental or modeling, led to characterize, discuss and then understand the transport mechanism in system characterized by nano-sized domains for which traditional models are not often suitable. The correct interpretation of such diffusing phenomena in relation with structural features should allow the development

of new materials with desired properties accurately tuned for several different needs, especially in the field of packaging applications.